2023

The Degradation Mechanisms of Aryl Hydrocarbon Receptor in Human Lung Epithelial Carcinoma A549 Cells

Rui Xiong
University of the Pacific

The Degradation Mechanisms of Aryl Hydrocarbon Receptor in Human Lung Epithelial Carcinoma A549 Cells

By

Rui Xiong

A Dissertation Submitted

In Partial Fulfillment of the

Requirements for the Degree of

DOCTOR OF PHILOSOPHY

Thomas J. Long School of Pharmacy
Pharmaceutical and Chemical Sciences

University of the Pacific
Stockton, California

2023

The Degradation Mechanisms of Aryl Hydrocarbon Receptor in Human Lung Epithelial Carcinoma A549 Cells

By

Rui Xiong

APPROVED BY:

Dissertation Advisor: William K. Chan, Pharm.D., Ph.D.

Committee Member: Craig Vierra, Ph.D.

Committee Member: Miki Park, Ph.D.

Committee Member: Wade Russu, Ph.D.

Committee Member: John Livesey, Ph.D.

Department Chair: William K. Chan, Pharm.D., Ph.D.

The Degradation Mechanisms of Aryl Hydrocarbon Receptor in Human Lung Epithelial Carcinoma A549 Cells

By

Rui Xiong

Acknowledgments

First and foremost, I would like to express my sincere gratitude to my research advisor, Dr. William Chan, for his continuous support, patience, valuable advice, and ideas. Without his assistance and guidance, I would not have had a chance to come here and finish my doctor's degree. He is a great mentor and I have the highest respect for him. His scientific attitude has greatly influenced me on how to conduct experiments and interpret data. Even though my project has been both enjoyable and challenging at times, his unwavering support, passion, and professional guidance always helped me navigate through difficult situations. Meanwhile, he always showed generosity in forgiving the mistakes I made during the early stages of my study. I feel so lucky to do research in his lab. The knowledge and experience I have gained under his guidance have been instrumental in shaping my perspective and skills, and I believe they will continue to benefit me throughout my career and life.

In addition, I would like to thank Dr. Craig Vierra for teaching me all the LC-MS/MS technology, I learned a lot from both his principle-based lectures and the collaborative work with him. I would like to thank Dr. Miki Park for always providing me with kind help when I came across difficulties. I would like to thank Dr. Wade Russu for giving me an opportunity to learn more about pro- and anti-apoptotic proteins. I would like to thank Dr. John Livesey for encouraging me to talk about my research project and always showing a great interest in it, which made me feel more confident.

I would also like to thank my lab mates: Dr. Jinyun Chen, Dr. Yujie Yang, Junyu Qian, Dan Shao, Sandra Do, Yiyuan Wang, and Sophia Wong for their contributions to

my research. I am also thankful to all the friends I met here; their company and help have made my life easier and enjoyable.

Finally, I would like to express my gratitude to my parents and family for their unconditional love and support all the time.

The Degradation Mechanisms of Aryl Hydrocarbon Receptor in Human Lung Epithelial Carcinoma A549 Cells

Abstract

By Rui Xiong

University of the Pacific
2023

The aryl hydrocarbon receptor (AHR), a cytosolic ligand-activated transcription factor, has been acknowledged as a critical regulator of xenobiotic-induced toxicity and carcinogenesis. In the absence of ligand, the AHR is cytoplasmic in a complex with Hsp90, p23, XAP2, and Src. The AHR complex translocates to the nucleus upon ligand binding. After releasing its chaperones, it forms a heterodimer with ARNT, which subsequently binds to a dioxin-responsive element (DRE) for target genes transcription. Multiple aspects of cells are altered by the substantial expression of AHR target genes. Even without the AHR ligand, the cytoplasmic AHR plays a critical role in tumor progression by affecting various cellular functions. Thus, understanding the mechanisms of AHR degradation is crucial, which provides novel ways to control the AHR target genes transcription and cellular functions. In addition to the 26S proteasomal degradation triggered by ligand or geldanamycin treatment, we discovered a novel AHR degradation pathway mediated by autophagy-lysosome in A549 cells. Specifically, the chaperone-mediated autophagy (CMA) facilitates the degradation of basal AHR in the lysosome. It can be activated by 6-AN, resulting in downregulated AHR protein levels and functions, including the ligand-dependent target genes transcription and cell migration/invasion process in A549 cells.

p23 as a part of the AHR cytoplasmic complex has been continuously studied in our lab over the past decade. The most prominent role of p23 is protecting AHR from degradation in both immortalized cancer cell lines (mouse hepatoma Hepa1c1c7, human hepatoma Hep3B, human cervical HeLa) and untransformed human lung bronchial/tracheal epithelial (HBTE) cell lines [1][117] [121]. It encouraged us to investigate the mechanisms further. In A549 cells, downregulation of p23 content reduced AHR protein levels, partially due to an elevated AHR protein degradation. This degradation was not reversed by proteasome inhibitor MG132 but partially restored by lysosome inhibitor CQ. We cannot rule out the possibility that selective macroautophagy was involved in the basal AHR degradation in A549 cells since the PLA results showed a positive interaction between AHR and LC3B. So far, Hela cells could be the best expression system for HaloTag-AHR overexpression. Thus, we can use the HaloTag technology as a powerful tool to study the AHR degradation mechanism via protein labeling and LC-MS/MS analysis.

Table of Contents

List of Tables

Table

List of Figures

Figure

List of Abbreviations

3MA	3-methyladenine
6-AN	6-aminonicotinamide
ActD	actinomycin D
AHR	aryl hydrocarbon receptor
AHRR	aryl hydrocarbon receptor repressor
AR	androgen receptor
ARNT	aryl hydrocarbon receptor nuclear translocator
ATG5	autophagy related 5
BaP	benzo[a]pyrene
BCA	bicinchoninic acid
bHLH-PAS	basic helix-loop-helix-PER-ARNT-SIM
CDK	cyclin D-cyclin-dependent kinase
CHIP	carboxy-terminus of Hsc70-interacting protein
CHX	cycloheximide
CMA	chaperone-mediated autophagy
CQ	chloroquine
CRISPR	clustered regularly interspaced short palindromic repeats
Cyp1a1	cytochrome P450 1a1
DMEM	Dulbecco's modified eagle medium
DMSO	dimethyl sulfoxide
DRE	dioxin response element

ECM	extracellular matrix
EDTA	ethylenediaminetetraacetic acid
e-MI	endosomal microautophagy
EMT	epithelial-mesenchymal transition
FICZ	6-formylindolo (3,2-b) carbazole
GA	geldanamycin
GFP	green fluorescent protein
GPX4	glutathione peroxidase 4
HBTE	human lung bronchial/tracheal epithelial
HIF-1α	hypoxia inducible factor 1 alpha
HSC70	heat shock cognate 70kDa protein
HSP90	heat shock protein 90
I3C	Indole-3-carbinol
IDO	idoleamine-2,3-dioxygenase
kDa	kilodalton
LAMP2	lysosome-associated membrane protein 2
LC3	microtubule-associated protein 1 light chain
LC-MS/MS	liquid chromatography with tandem mass spectrometry
LUAD	lung adenocarcinoma
MA	macroautophagy
Met	metformin
MMP	matrix metalloproteinase
NADPH	nicotinamide adenine dinucleotide phosphate

NF-κB	nuclear factor-κB
NLS	nuclear localization signal
NSCLC	Non small cell lung cancer
p23	prostaglandin E synthase 3
p23KD	p23 gene knockdown
p62/SQSTM1	sequestosome-1
PAH	polycyclic aromatic hydrocarbons
PCR	polymerase chain reaction
PI3K	phosphatidylinositol 3-kinase
PLA	proximity ligation assay
PMSF	phenylmethanesulfonylfluoride
Rap	rapamycin
RNP	ribonucleoprotein
ROS	reactive oxygen species
SDS-PAGE	sodium dodecyl sulfate-polyacrylamide gel electrophoresis
sgRNA	single guide RNA
Src	proto-oncogene tyrosine-protein kinase
TCDD	2,3,7,8-tetrachlorodibenzo-*p*-dioxin
TDO	tryptophan-2,3-dioxygenase
TEMED	tetramethyl ethylenediamine
TGF-β	transforming growth factor-β
UCHL3	ubiquitin carboxy-terminal hydrolase isozyme L3
VEGF	vascular endothelial growth factor

WT	wild type
XAP2	hepatitis B virus-x associated protein 2
βME	beta-mercaptoethanol

CHAPTER 1: INTRODUCTION

Aryl hydrocarbon receptor (AHR)

Aryl hydrocarbon receptor is a ligand-activated transcription factor from the basic helix-loop-helix-periodic circadian protein (PER)-AHR nuclear translocator (ARNT)-single-minded protein (SIM) (bHLH-PAS) superfamily. It recognizes both exogenous and endogenous ligands present in the environment. The Aryl hydrocarbon receptor (AHR) is found to be expressed ubiquitously and is typically located in the cytoplasm. It is present in an inactive complex that includes a heat shock protein 90 (hsp90) dimer, co-chaperone prostaglandin E synthase 3 (p23 or PTGES3), X-associated protein 2 (XAP2, AIP, or ARA9), and the protein kinase Src [2]. Upon binding with the ligands, AHR dissociates from its inactive complex and moves into the nucleus due to its nuclear localization signal. It then forms a complex by dimerizing with ARNT, which is capable of binding to dioxin response elements (DREs) of AHR-target genes, followed by co-activators recruited for the transcription of numerous target genes. As a result of activating AHR, a number of detoxification genes are transcribed, including phase I drug metabolizing cytochrome P450 enzymes (e.g., CYP1A1, CYP1A2, and CYP1B1), phase II enzymes (e.g., NADPH dependent quinone oxidoreductase-1, aldehyde dehydrogenase, and UDP-glucuronosyl transferase), and phase III transporters (e.g., P-glycoprotein and multidrug resistance-associated proteins). They are essential for drug absorption, distribution, metabolism, and excretion in the liver, intestine, kidney, and brain tissues. Especially, the drug metabolizing P450 enzyme plays an important role in metabolism, eliminating and detoxification of xenobiotics [3]. Cytochrome P450 1A1

(CYP1A1) expression is largely dependent on AHR activity and can be significantly induced through multiple DREs upon AHR activation. The transcriptional activity of AHR is repressed by the aryl hydrocarbon receptor repressor (AHRR), which competes with ARNT dimerization and binds to the DRE region. On the other hand, AHRR is one of the AHR target genes activated by the AHR/ARNT dimer binding to the DRE sequence located in the AHRR target gene [4]. In addition, the nuclear export signal sequence is exposed after AHR-ARNT heterodimer formation and then triggers its shuttling back to the cytoplasm for rapid degradation of AHR in the proteasome. In several cell line treatments, the AHR protein is reduced by 80-95% within 4 hours of TCDD treatment. As long as the ligand is present in the medium, and the AHR protein does not recover to its basal levels [5].

The AHR ligands

There are a variety of ligands that have been identified for the AHR, including natural compounds such as tryptophan metabolites, flavonoids, and indoles, as well as synthetic compounds such as polycyclic aromatic hydrocarbons (PAHs), dioxins, and polychlorinated biphenyls (PCBs). These ligands can have a range of effects on the AHR signaling pathway. High doses of dioxin exposure can trigger skin lesions like chloracne. Long-time exposure can cause more severe effects like tumorigenesis, inflammation, immunotoxicity, steroid hormone dysfunction, neurodevelopmental abnormalities, and reproductive dysfunctions. 2,3,7,8-tetrachlorodibenzo-ρ-dioxin (TCDD) has been classified as group 1 carcinogen to humans and PCBs are identified as group 2A, which means it is probably carcinogenic to humans, according to the International Agency for Research on Cancer (IARC). TCDD has a long half-life (more

than 10 years) in humans since it is hard to metabolize into a polar derivative that our bodies can easily eliminate. In recent years, natural compounds have been identified as AHR ligands continuously. Vegetables and fruits that contain flavonoids are the most abundant category of polyphenols, such as resveratrol and quercetin. Indole-3-carbinol (I3C) comes from cruciferous vegetables and is another kind of AHR ligand precursor. AHR ligands exist not only in external sources but also as molecules that are formed by endogenous metabolism in the body. Examples of such molecules include formylindolo [3,2-b] carbazole (FICZ), indirubin, indigo, metabolites of arachidonic acid, and kynurenine pathway metabolites [6]. In mammals, there are three critical enzymes for metabolization of tryptophan to N-formyl-kynurenine: tryptophan-2,3-dioxygenase (TDO) and idoleamine-2,3-dioxygenases (IDO1 and IDO2) [7]. TDO2 and IDO1 can be expressed in various tumors, resulting in significant production of kynurenine, which is a relatively weak AHR ligand. The expression level of TDO2 is positively correlated with AHR target gene *cyp1b1* in human glioblastoma which is produced by high levels of kynurenine via activating AHR signaling pathway. Their results also showed a positive correlation between *cyp1b1* mRNA levels and poor survival rate of patients with glioblastoma [8].

Expression of AHR in tumorigenesis

Even if the levels of aryl hydrocarbon receptor (AHR) expression are low, the presence of high-affinity AHR ligands can still lead to significant AHR transcriptional activity in vitro. When low-affinity ligands are produced locally, the expression level of AHR plays a crucial role in determining its impact during tumor development. The expression of AHR is observed in most tissues except for skeletal muscle, and its levels

vary widely in different cells and tissues. The liver, lung, spleen, and kidney show the highest expression levels of AHR. In general, cells of epithelial origin exhibit the highest expression levels of AHR in a given tissue. The immunohistochemical analysis supported that the tumor showed increased expression levels of AHR when compared to the surrounding normal tissues [9][10]. It could be explained by the fact that the increased expression of AHR in tumor tissues is due to the correlation with nuclear factor-κB (NF-κB) and signal transducer and activator of transcription 6 (STAT6), which are known to enhance inflammatory responses. A specific response element for NF-κB and RELA-p50 heterodimer binding was identified in the promoter of the human *AHR* gene [11]. Another way to find out whether AHR is transcriptionally activated is to determine the translocation of AHR from cytoplasm to nucleus using immunohistochemistry. There is a positive correlation between the poor prognosis of patients with lung squamous cell carcinoma and nuclear localization of AHR [10]. In contrast, the expression levels of AHR in breast cancer were negatively correlated with the histological grade of tumors, which could be due to the fact that AHR mediated the degradation of ER through the proteasome pathway [12]. Moreover, another possible way to investigate the involvement of AHR activity in human tumors is to assess the expression levels of a target gene that is regulated by AHR, such as *cyp1a1* and *cyp1b1*. A study on the relationship between CYP1B1 expression and survival rates of patients with glioblastoma suggested that lower CYP1B1 expression correlated with higher survival rates [8]. It has been suggested by recent studies that higher expression or activity of AHR is associated with the advancement of late-stage tumorigenesis in most human tumors, which could provide a selective advantage for tumor growth.

Physiological role of AHR in tumor progression

AHR has been recognized as an important transcription factor in regulating xenobiotic-induced toxicity and carcinogenesis. However, its physiological role in tumor progression without xenobiotics remains unclear. Under normal physiological conditions, recent studies demonstrated that AHR plays a critical role in cell proliferation, metastasis, and differentiation by affecting cell cycle, apoptosis, cell-cell contact, extracellular matrix (ECM), and angiogenesis in the progression of cancers.

Cell cycle regulation

AHR has the capability to facilitate the process of the cell cycle without the presence of external ligands [13]. Further analysis of the cell cycle indicated that the increased proliferation rates resulted from an enhanced progression of the cell cycle, characterized by an upregulated proportion of cells transitioning into the S and G2/M phases. However, Abdelrahim et al. discovered that unliganded AHR displayed a cell context-dependent manner, which showed growth promoting effect on HepG2 while inhibiting effect on MCF-7 [14]. The proliferation of human lung cancer A549 cells was increased by the overexpression of AHR, which resulted in a significant increase of DNA synthesis-related genes expression, including the proliferating cell nuclear antigen (PCNA) and RFC38. The regulation of these genes is primarily governed by E2F1, a transcription factor that plays a critical role in the progression of the cell cycle from G1 to S phase. A complex between AHR and E2F1 can be directly formed on the regulatory region of E2F1 through the PAS-B domain of AHR. This is followed by the recruitment of activators for thyroid hormone and retinoid receptors (ACTR). This interaction indicates the physiological role of AHR as a strong transcriptional coactivator for E2F1-

dependent transcription. Furthermore, it suggested that the AHR-E2F1 interaction is a component of the mechanism through which AHR/ARNT promotes cell proliferation [15]. Another mechanism of AHR in regulating cell cycle progress depends on the retinoblastoma tumor suppressor protein (RB). Progression from G1 to S phase within the cell cycle is regulated by the sequential phosphorylation of the RB protein via cyclin D-cyclin-dependent kinase (CDK) 4/6 complexes. AHR participated in the interaction with CDK4 and CCND1 to form a complex that facilitated cell cycle progression without external ligands. However, the presence of exogenous ligand TCDD can disrupt this interaction and lead to G1 cycle arrest [13]. In addition, AHR can regulate the cell cycle by activating the cyclin-dependent kinase inhibitor p21 and the p27Kip1 cyclin/CDK inhibitor [16].

Apoptosis

It is conceivable that AHR regulates the expression of genes involved in apoptotic signaling. The critical role of AHR in the anti-apoptotic response within human breast cancer cells, coupled with its potential overexpression, offers a plausible explanation for the developmental process of environmentally induced breast cancers [11]. The AHRR *gene* expression was knocked down in both the human lung cancer cell line and non-cloneable normal HMECs, resulting in the acquisition of resistance to apoptotic signals, increased motility and invasion capabilities in vitro, and enhanced angiogenic potential in vivo. The exposure of murine hepatoma 1c1c7 cultures, which contain AHR, to various apoptosis-inducing factors resulted in a concentration-dependent suppression of cell proliferation, reduction of viability, and initiation of apoptosis. These effects were determined through the examination of DNA

fragmentation and caspase activation. However, it is important to note that Tao cells, a variant of the hepatoma 1c1c7 cell line, exhibited no such response, as they possess only 10% of the AHR content found in hepatoma 1c1c7 cells. The correlation between AHR content and susceptibility to apoptosis was verified by reducing AHR levels in hepatoma 1c1c7 cells and increasing AHR levels in Tao cells. Bid and procaspase -9, -3, and -12 processing were observed exclusively in cells containing AHR. The Tao endosomal/lysosomal extracts exhibited ~50%, 35%, and 55% of the Bid cleavage and cathepsin B and D activities of hepatoma 1c1c7 endosomes/lysosomes, respectively. This suggested that the content of endosomal/lysosomal cathepsin B and D is associated with AHR expression. It has been proposed that AHR could potentially impact the movement and breakdown of proteases that are typically present in endosomes and lysosomes. This could result in the activation of Bid through the release of proteases like cathepsin D, ultimately leading to the initiation of the apoptotic program [17]. In addition, the determination of cell fate processes could be influenced by AHR in a cell context-dependent manner. In contrast to stimulating growth arrest and apoptosis in most liver cells, TCDD facilitates the clonal expansion of preneoplastic hepatocytes, which are identified as enzyme-altered foci (EAF). This expansion occurs by inhibiting apoptosis and bypassing AHR-mediated growth arrest. They hypothesized that the continuous activation of AHR in the liver, when exposed to genotoxic carcinogens, exerts a significant selective pressure. This pressure, in turn, leads to the preferential growth and expansion of clones that evade growth arrest and apoptosis [18]. This is consistent with the concept of multistep tumor progression, wherein a series of clonal

expansions occur, each of which is initiated by the acquisition of a favorable mutant genotype by chance.

Cell-cell contact

Tumor progression and promotion are initiated by the absence of cellular interaction. AHR is involved in the signaling cascade of contact inhibition, resulting in deregulation of proliferation, differentiation, and cell motility. The disruption of cadherin dependent cell-cell contact is significantly influenced by Src kinase, a crucial component of the AHR complex. Ligand binding to AHR induced the dissociation of Src kinase from the AHR complex and its subsequent translocation from the cytoplasm to the membrane. This kinase activity of Src facilitated the destabilization of cell-cell contact [19]. Epithelial-mesenchymal transition (EMT) is crucial in the process of tumor metastasis, and E-cadherin is considered to be an important regulator in cell-cell contact. AHR acts as a transcription factor in activating Slug expression which inhibits E-cadherin expression, resulting in upregulated EMT and loss of cell-cell contact [20]. On the other hand, previous studies suggested that the transcriptional activity and nuclear localization of AHR were upregulated when cellular contact was disrupted. In in vitro wound healing analysis, activation AHR which is assessed by utilizing green fluorescent protein as a reporter of transcriptional activity occurred in the cells located at the wounded edge. The generation of signals resulting from the loss of cell-cell contact leads to an elevation in the phosphorylation level of AHR, specifically the phosphorylation of Ser68 situated within the nuclear export signal sequence. Consequently, this phosphorylation induced the accumulation of AHR within the nucleus due to the inhibition of its export activity [21].

Extracellular matrix remodeling

The extracellular matrix (ECM) regulates cell shape, proliferation, migration, and differentiation. It is constituted by a variety of proteins and polysaccharides, establishing an intricate network that connects cells within tissues. ECM serves a dual role in facilitating cellular communication and as a supply for growth factors and other signaling molecules. It is a dynamic structure that undergoes constant remodeling in tumor pathogenesis. ECM remodeling, including its assembly and degradation, is influenced by the 3D environment and cellular tension mediated by integrins and proteolysis. Proteolytic enzymes, such as matrix metalloproteinases (MMPs), and cysteine proteases, and serine proteases, play an important role in the modulation of ECM. These enzymes contribute to ECM remodeling through various mechanisms, which include the direct degradation of matrix proteins, the release of small bioactive peptides, and the release of growth factors that are stored within the ECM. Moreover, these proteolytic enzymes have been identified as targets of the AHR pathway. TCDD and AHR activation have been shown to regulate the expression levels of several ECM proteins, such as collagen and fibronectin [22].

MMPs are a group of enzymes that rely on zinc and calcium for their functionality. Collectively, they have the capability to break down all the ECM. Their dysregulation serves as a distinctive characteristic of cancer metastasis. The AHR pathway is involved in regulating the expression and activity of MMPs. Exposure to TCDD resulted in an elevation of MMP-1 expression in normal human keratinocytes, while A2058 melanoma cells with enhanced invasion capability exhibited increased levels of MMP-1, MMP-2, and MMP-9 [23]. Activation of the AHR pathway elicited the upregulation of

MMP-9 expression, thereby enhancing the invasiveness of gastric cancer cells [24]. MMP2 activity was significantly reduced in AHR-/- mouse embryo fibroblasts [25].

Cathepsin B and C are cysteine proteases that have been identified as targets of the AHR pathway. The down-regulated cathepsin B, capable of degrading type IV collagen, laminin, and fibronectin in vitro, was observed in porcine thyrocytes upon exposure to TCDD. In MCF-7 cells, the expression of cathepsin D induced by estrogen was inhibited by both exposure to TCDD and the activation of the constitutively active aryl hydrocarbon receptor (CA-AHR) [26]. In addition, serine proteases are targets of the AHR pathway. Upon binding to the urokinase plasminogen activator (uPA) receptor on the cell surface, the uPA undergoes a conversion process facilitated by cysteine proteases, ultimately resulting in the activation of the enzyme. Plasmin is activated by uPA followed by degrading ECM proteins. uPA activates pro-MMPs and participates in the cleavage of collagen. The inhibitor of plasminogen activator -1/2 (PAI-1/2) suppressed the function of uPA, which could block the proteolytic cascades effectively. Previous studies demonstrated that both uPA and PAI-1/2 are targets of the AHR pathway and regulated by TCDD [27].

Angiogenesis

Angiogenesis plays a crucial role in the progression of tumors. It is a precisely controlled cellular process that is balanced by signals promoting and inhibiting blood vessel formation, such as angiopoietins, integrins, junctional molecules, oxygen sensing agents, chemokines, and endogenous inhibitors. Vascular endothelial growth factor A (VEGF-A) is widely accepted as one of the most prominent prototypes of angiogenesis inducers. AHR is involved in vascular homeostasis and endothelial responses to toxins.

AHR-null mice have impaired angiogenesis in vivo, thereby impeding the growth of tumor xenografts. AHR−/− aortic endothelial cells (MAECs) with lower expression of VEGF-A failed to form tube-like structures in culture, but cotreated with VEGF-A rescued this process. They also demonstrated that HIF1α regulated VEGF expression mediated by AHR. It is noteworthy that AHR-null stromal myofibroblast exhibited heightened production of transforming growth factor-β (TGFβ) activity. This increase in TGFβ activity resulted in the inhibition of angiogenesis in human endothelial cells (HECs). Furthermore, the modulation of angiogenesis was observed to be a result of the collaborative actions of VEGF and TGFβ. This was evident from the fact that the introduction of TGFβ to AHR−/− MAECs, which already exhibited low basal VEGF-A activity, led to a further reduction in their VEGF-A activity. Therefore, the modulation of angiogenesis by AHR is dependent on the activation of VEGF in the endothelium and the inactivation of TGFβ in the stroma [28]. Knockdown of AHRR in the human lung cancer cell line led to an increase in motility and invasion in vitro, as well as an enhanced angiogenic potential in vivo. Conversely, ectopic AHRR overexpression in tumor cells resulted in a decrease in angiogenic potential [29].

The transwell migration and invasion assays are useful techniques for investigating the mechanisms involved in angiogenic events, as endothelial cell migration and invasion play a crucial role in angiogenesis. The movement of cells from one location to another, guided by external biochemicals, is commonly referred to as cell migration. On the other hand, cell invasion evaluates the capacity of endothelial cells to cross a three-dimensional matrix, such as basement membranes.

Autophagy

The lysosomal degradation pathways differ from the ubiquitin-proteasome system as they include the targeting and degradation of cargo material within the lysosomes. Lysosomes, which are membrane-bound organelles, are widely recognized as the primary compartments for degradation and recycling in eukaryotic cells. It provides an acidic environment for optimal activity of hydrolases, such as proteases, lipases, nucleotidases, and glycosidases, which enable them to break down various types of macromolecules. Lysosomal delivery systems include the processes of endocytosis and autophagy. Endocytosis is crucial for the breakdown of substances originating from outside the cell, while autophagic pathways specifically aim at internal cellular components. Autophagy is a catabolic process that adaptively directs intracellular materials, including damaged organelles, aggregated proteins, or long-lived proteins, toward degradation within lysosomes. Two significant types of autophagy have been elucidated: 1) bulk autophagy or non-selective autophagy; 2) selective autophagy. The basal activity of autophagy is essential for maintaining cellular quality control and homeostasis. However, it reaches its maximum activation in response to various stress stimuli, including nutrient deprivation and hypoxia. Autophagosome formation induced by starvation is likely to occur in a cargo-independent manner, whereas in the absence of nutrient deprivation, the formation of autophagosomes depends on specific cargo [30]. Selective autophagy can target and degrade various cargos, including intracellular pathogens (xenophagy), mitochondria (mitophagy), peroxisomes (pexophagy), certain endoplasmic reticulum (ER-phagy), ribosomes (riophagy), inflammasome, midbody, and aggregated/misfolded proteins. There are three distinct subtypes of autophagic

pathways, each with its own unique molecular and regulatory mechanisms. These subtypes are categorized based on the way by which the cargo material is transported to lysosomes: macroautophagy (MA), microautophagy (MI), and chaperone-mediated autophagy (CMA). Here, only selective autophagy pathways are elaborated in detail.

Selective Macroautophagy

Macroautophagy is extensively researched in this field and is particularly effective in breaking down large cargos, including mitochondria, bacteria, and protein aggregates. The process requires the formation of autophagosome, a double membrane vesicle, which subsequently engulfs a portion of the cytoplasm. Ultimately, it fuses with lysosomes for degradation. To achieve selectivity, labels are necessary to identify the cargos susceptible to degradation through selective autophagy. Ubiquitin-linked chains can be a signal for it. In addition, p62/SQSTM1 (sequestosome-1), which was identified as an autophagic receptor, links the ubiquitinated cargo and phagophore together. The phosphorylated p62 was used to determine selective autophagy levels distinguished from non-selective autophagy. p62 mediates interaction with ATG8 on phagophore [31].

ATG8 is an autophagy-related ubiquitin-like protein family. There are at least seven kinds of ATG8 in mammals (LC3A, LC3B, LC3C, GABARAP, GABARAPL1, GABARAPL2 and GABARAPL3), which can be divided into two subfamilies: the microtubule associated protein light chain 3 (LC3) subfamily and the gamma-aminobutyric acid receptor associated protein (GABARAP) subfamily. The primary homologue of ATG8 in mammalian autophagy is LC3B. The ATG4 protease cleaves ATG8 at the C-terminal, resulting in the exposure of a glycine residue and the

production of form I of the ATG8 molecule (LC3-I). Then the glycine residue is conjugated to lipid phosphatidylethanolamine (PE) generating form II of ATG8 molecule (LC3-II). LC3-II is an autophagic marker since it is bound to the membranes of the autophagosome tightly [32].

Autophagic receptors bind both the cargo and lipidated ATG8 protein for selectively triggering autophagosome formation. Although there are various autophagic receptors identified now, they share some common criteria. 1) Autophagic receptors contain LC3 interacting region (LIR) which binds to ATG8 proteins. Some autophagic receptors have more than one LIR, which could enhance the affinity to ATG8 for autophagosome formation. 2) Autophagic receptors contain cargo binding domains providing direct interaction with substrates. 3) Both autophagic receptors and their cargos are degraded through lysosomes. 4) Deletion of autophagic receptor does not affect non-selective autophagy or bulky autophagy, and it has no effect on the degradation of other kinds of cargos [33]. Take p62 as the representative, human p62 has 440 amino acids. From the N-terminal to C-terminal, it contains PB1 domain, ZZ-zinc finger domain, (NLS) nuclear localization, (NES) nuclear export signal, LC3-interacting region (LIR), KEAP1 interacting region (KIR) and Ub-associated (UBA) domain. PB1 domain makes p62 interact with other protein kinases. Most importantly, it helps p62 to oligomerize with themselves or hetero-polymerize with other proteins containing the PB1 domain. This polymeric structure enables cargo coaggregation. It also facilitates the tight interaction between the cargos and PE conjugated ATG8 at the phagophore [34]. The LIR mediates p62 binding to all members of the ATG8 family, which is also required for autophagic degradation of itself. Thus, p62 is a selective

autophagy substrate as well [35]. Selective autophagy is initiated with labeled cargos, and most cargos are labeled with ubiquitin. The UBA domain enables p62 to bind both mono and poly ubiquitin labeled proteins. But p62 has a more preference for mono-Ub binding. Thus, p62 is inclined to K63-Ub chains than K48-Ub chains. Since the conformation of K63-Ub chains is more extended and open when compared to K48-Ub chains [36].

Autophagy inhibition is considered to affect the degradation of specific autophagy cargos, such as long-lived proteins, aggregated proteins, and organelles. However, some studies showed the accumulation of certain short-lived proteins in response to long-term inhibition of autophagy. These short-lived proteins normally are degraded through 26s proteasome. For example, p53 and beta-catenin, which are also important regulatory proteins. However, this decreased proteasomal degradation is not caused by the inhibition of proteasome function and subunits expression. It is due to delayed delivery of ubiquitinated cargos to 26S proteasome [37]. On the one hand, the p62 oligomers that are generated by oligomerizing with itself or other proteins containing the PB1 domain would include multiple UBA domains. This structure could not only sequester ubiquitinated autophagic cargos but also proteasomal substrates, leading to a decreased diffusion rate. On the other hand, the multiple UBA domains of p62 protect the ubiquitin surface from being recognized by the 26S proteasome ubiquitin receptors. There is no direct inhibition of proteasome activity since autophagy deficiency has no effect on 26S proteasome degradation of ubiquitin-independent substrates [38].

Chaperone-mediated autophagy

For a long time, lysosome was not considered to degrade individual proteins selectively. However, the discovery of chaperone-mediated autophagy (CMA) changed this notion. Briefly, proteins are identified by a chaperone that helps to deliver the proteins to the surface of the lysosomes for degradation. This is a kind of direct lysosomal uptake autophagy only found in mammalian cells so far. There is saturability when substrates bind to the lysosomal membrane, which suggests that there must be a specific membrane receptor in this process [39]. The KFERQ-like motif in substrate proteins is recognized by the heat-shock cognate protein of 70 kDa (hsc70). Then the substrates are targeted to the lysosomal membrane, binding to the lysosome-associated membrane protein type 2A (LAMP2A). Before substrate proteins are translocated into the lysosome for degradation, they are unfolded and the substrate proteins binding leads to multimerization of LAMP2A to form a channel-like structure across the lysosomal membrane. Moreover, with the assistance of luminal lysosome-associated hsc70 (lys-hsc70), the substrates can be completely translocated into the lysosome for hydrolysis [40].

All the proteins degraded by lysosomes through CMA contain a pentapeptide motif KFERQ in their sequence. This KFERQ-like peptide is sufficient and necessary for the chaperone-mediated selectivity of proteins. Ribonuclease A (RNase A) was the first identified substrate for CMA degradation. Studies showed that the lysosomal degradation of RNase A was completely abolished by removing the KFERQ motif in the absence of nutrients. Moreover, proteins that are not normally processed for lysosomal degradation can be induced to degrade by CMA when attaching this KFERQ sequence

to them [41]. A KFERQ-like motif is not specific amino acids, but it represents the properties of individual amino acid. They are composed of a positively charged residue: K or R; a hydrophobic residue: I, L, V or F; a negatively charged residue: D or E; the fourth amino acid can be either hydrophobic or positive; glutamine can be on either side of the motif [42]. Recent studies support that posttranslational modification contributes to the KFERQ-like motif composition in the absence of one residue. Glutamine can be replaced by acetylation of a lysine, a negatively charged residue can be replaced by phosphorylation of a residue [43]. The motif located in proteins must be accessible for chaperone binding, and Dice JF's study showed that one motif in a protein is sufficient for CMA targeting. Even though there are more than 30% soluble proteins containing this KFERQ-like motif, they cannot be classified as substrates only for CMA degradation. Because this motif can also be targeted for microautophagy and other functions [44].

The level of LAMP2A regulates CMA activity since the substrate binding to it is essential for CMA. The requirement of translocation is the multimerization of LAMP2A. Studies showed that there is a restriction of translocation in mutations of LAMP2A with substrate binding activity but cannot form complex after binding. LAMP2A complex is disassembled into monomers for the next cycle of substrate binding after the previous one has been translocated into the lysosome. Thus, this process is identified as targeting proteins one by one for CMA degradation [40].

CMA has been suggested to exhibit constitutive activity in mammalian cells at basal levels, however, it can be maximally activated by various stress conditions including prolonged starvation, hypoxia, and oxidative stress. Starvation activates CMA in most types of cells. The proteins degraded through CMA are used to synthesize other

needed proteins. Usually, it starts with about 30 minutes of starvation into macroautophagy, followed by upregulation of CMA after about 10 hours of starvation. In some tissues, CMA is upregulated at about 36 hours of starvation and lasts for 3 days [45]. This delayed activation of CMA in response to starvation could selectively degrade non-essential proteins to synthesize essential proteins. In contrast, starvation induced macroautophagy is bulk and non-selective. Furthermore, CMA functions to selectively degrade damaged or misfolded proteins in response to stress, preventing the protein from aggregation. In addition, CMA functions in many other pathways since different kinds of substrates are degraded by it. There are several transcription factors identified as CMA substrates. Thus, CMA affects the transcription pathway and multiple cellular processes.

However, CMA cannot be isolated from other components of the cellular protein control. Inhibition of CMA by knocking down LAMP2A activates macroautophagy and enhances proteasome degradation in most types of cells [46]. Without stress, this compensation is enough for the cell to survive. However, as the number of damaged proteins increases due to stress, the compensation by another degradation pathway cannot support these damaged proteins' degradation, resulting in cell death [46]. And blockage of macroautophagy or proteasome degradation conversely upregulates CMA activity [47]. Compensation plays a vital role in maintaining cellular protein levels under healthy conditions. Koga, H found that malfunction of macroautophagy in Huntington’s disease is compensated by activation of CMA. However, this continuous CMA compensation is exhausted soon, resulting in pathogenic huntingtin protein aggregation [48].

Selective endosomal microautophagy (e-MI)

Among the three autophagy pathways, little information is available regarding microautophagy. The morphology studies showed that the lysosome membrane invaginates to randomly entrap the cytosolic components for degradation. Interestingly, cytosolic cargos can also be internalized selectively in the late endosomes for e-MI degradation. A recent discovery in selective autophagy is that hsc70 binding to cytosolic proteins containing the KFERQ motif can be delivered to late endosomes where proteins are degraded through endosomal microautophagy (e-MI) [44]. There are similarities between CMA and selective e-MI. A KFERQ-like motif is required in the substrates, which are recognized by Hsc70. Nevertheless, e-MI does not need LAMP2A to target the lysosome membrane, which directly binds to the phospholipid phosphatidylserine on the endosomal membrane. Moreover, the substrate proteins translocate into late endosomes without unfolding. Although they share the same KFERQ-like motif, their substrates are not completely the same. The KFERQ-like motif is necessary and sufficient for hsc70-mediated CMA lysosomal degradation, but attaching this motif is not sufficient for mammalian e-MI. Thus, further identification of the sequence and structure of substrate proteins for e-MI targeting will be needed [49].

CHAPTER 2: ACTIVATION OF CHAPERONE-MEDIATED AUTOPHAGY INHIBITS THE ARYL HYDROCARBON RECEPTOR FUNCTION BY DEGRADING THIS RECEPTOR IN HUMAN LUNG EPITHELIAL CARCINOMA A549 CELLS

Abstract

The aryl hydrocarbon receptor (AHR) is a ligand-activated transcription factor and a substrate protein of a CUL4B E3 ligase complex responsible for diverse cellular processes. In the lung, this receptor is responsible for bioactivation of benzo[a]pyrene during tumorigenesis. Realizing that the AHR function is affected by its expression level, we are interested in the degradation mechanism of AHR in the lung. Here, we have investigated the mechanism responsible for AHR degradation using human lung epithelial A549 cells. We have observed that the AHR protein levels increase in the presence of chloroquine, an autophagy inhibitor, in a dose-dependent manner. Treatment with 6-aminonicotinamide (6-AN), a chaperone-mediated autophagy (CMA) activator, decreases the AHR protein levels in a concentration-dependent and time-dependent manner. This decrease suppresses the ligand dependent activation of the AHR target gene transcription, and can be reversed by chloroquine, but not MG132. Knockdown of lysosome-associated membrane protein 2 (LAMP2), but not autophagy related 5 (ATG5), suppresses the chloroquine-mediated increase of the AHR protein. AHR is resistant to CMA when its CMA motif is mutated. Suppression of the epithelial-to-mesenchymal transition in A549 cells is observed when the *AHR* gene is knockout or the AHR protein level is reduced by 6-AN. Collectively, we have provided evidence supporting that AHR is continuously undergoing CMA and activation of CMA suppresses the AHR function in A549 cells.

Introduction

The aryl hydrocarbon receptor (AHR) is a biological sensor which alters gene expression in response to many environmental pollutants (such as dioxins and polychlorinated biphenyl compounds) and flavonoids [50, 51]. Many tryptophan metabolites (such as 6-formylindolo (3,2-b) carbazole (FICZ)) have been shown to be the endogenous ligands of this receptor. These metabolites can be generated in the gut microbiome and subsequently activate AHR in human cells [52]. AHR suppresses immune response in part by promoting naïve T cells differentiation into T regulatory cells [53]. It also drives the growth of many tumors [54], promotes insulin resistance [55], and is a drug target for psoriasis treatment [56]. Interestingly, AHR has been implicated as a drug target for the treatment of SARS-CoV2 infection since AHR may alter the lung function in favor of supporting SARS-CoV2 infection [57, 58]. Regarding the role of AHR in lung tumorigenesis, there are conflicting reports on the effect of AHR on the epithelial-mesenchymal transition (EMT). Although some researchers observed positive correlation between the AHR action and the aggressive phenotypes of invasion and metastasis in lung and other cell types [59-62], others reported that AHR suppressed metastasis by inhibiting the lung EMT [63, 64]. Nonetheless, the expression levels of AHR must correlate positively with its function in the lung. We are interested in studying the degradation mechanisms of AHR in lung epithelial cells in affecting the AHR function.

AHR exists as a complex in the cytoplasm with heat shock protein 90 (HSP90), prostaglandin E synthase 3 (p23), hepatitis B virus-x associated protein 2 (XAP2), and possibly proto-oncogene tyrosine-protein kinase (Src) [65-67]. Exposure of the nuclear

localization sequence of AHR after ligand binding leads to nuclear translocation of the complex. Binding of aryl hydrocarbon receptor nuclear translocator (ARNT) to AHR in the nucleus dissociates the complex [67]. The AHR-ARNT heterodimer binds to its dioxin response element (DRE) enhancer, activating the transcription of its target genes, such as cytochrome P450 1a1 (*cyp1a1*). Alternatively, AHR serves as a substrate protein that recruits its target proteins (for example, ERα) to CUL4B E3 ligase for proteasomal degradation [68].

Interestingly, AHR is degraded via autophagy in many human cell lines, namely the lung A549, liver Hep3B, and breast T-47D and triple-negative MDA-MB-468 cells [69]. Proteins can be selectively degraded via selective macroautophagy and chaperone-mediated autophagy (CMA) [70, 71]. Selective macroautophagy employs p62 to escort client proteins into autophagosomes by interaction with microtubule-associated protein 1 light chain (LC3) at the autophagosome membrane, followed by fusion with lysosomes. This fusion leads to lysosomal degradation of the client proteins. Many autophagy-related gene proteins, such as *ATG5*, are essential for LC3 lipidation at the membrane during the process of selective macroautophagy [72, 73]. Alternatively, client proteins are escorted by heat shock cognate 70 kDa protein (HSC70) to lysosomes by interaction with the lysosomal membrane glycoprotein LAMP2A, leading to internalization of the client proteins for degradation. This process is called chaperone-mediated autophagy (CMA). LAMP2A plays an important role in the CMA process by mediating the lysosomal degradation of proteins in response to various stresses and keeping the normal turnover of proteins with a long biological half-life [74]. We have observed that degradation of AHR via autophagy is cell line specific: AHR undergoes

selective macroautophagy in human cervical HeLa cells [69] and CMA in triple-negative breast cancer MDA-MB-468 cells [75]. Here, we provide evidence that CMA is responsible for AHR degradation in human lung epithelial A549 cells. Targeting the AHR degradation mechanism can be a viable approach in the lung since modulation of the AHR protein level via CMA alters the AHR function in A549 cells.

Results

CQ increases the AHR protein levels of A549 cells in a functionally relevant manner

CQ is a general autophagy inhibitor which inhibits the lysosomal proteases. We addressed whether AHR undergoes autophagy in A549 cells by examining the AHR content in the presence of CQ. Treatment of A549 cells with 60 and 100 μM CQ for 6 hours increased the AHR protein levels to 1.5- and 2-fold, respectively (Fig. 2.1A). To address whether a 2-fold increase of the AHR content would elicit any functional significance, we examined the effect of this fold change on the ligand dependent upregulation of the AHR target gene *cyp1a1*. As expected, treatment with 100 μM CQ for 6 hours increased the AHR protein content by 2-fold in the presence or absence of benzo[a]pyrene (BaP) (Fig. 2.1B). Treatment with 5 μM BaP alone for 4 hours reduced the AHR protein content due to proteasomal degradation of AHR after ligand binding [76, 77]. We observed that BaP caused a 10-fold increase of the *cyp1a1* transcript after 4 hours of treatment (Fig. 2.1C). This upregulation was enhanced from 10- to 38-fold in the presence of 100 μM CQ, showing that a 2-fold increase of the AHR content (when compared between BaP and BaP/CQ treatments) caused significant increase of the AHR function. Treatment with CQ alone did not change the *cyp1a1* transcript level,

confirming that the upregulation of the *cyp1a1* gene transcription was mediated by BaP, not CQ. Collectively, we conclude that a 2-fold increase of the content of A549 AHR by CQ can significantly enhance the BaP dependent AHR function.

Fig. 2.1

Inhibition of lysosomal degradation increased the AHR protein level and its ligand dependent activation of the cyp1a1 gene transcription in A549 cells.

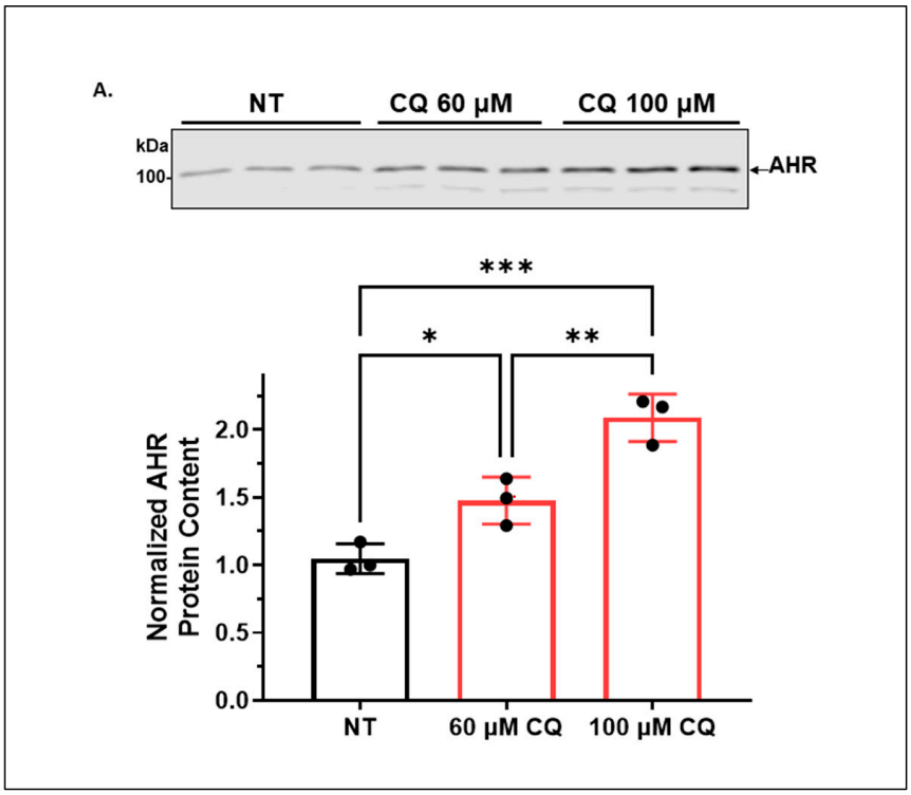

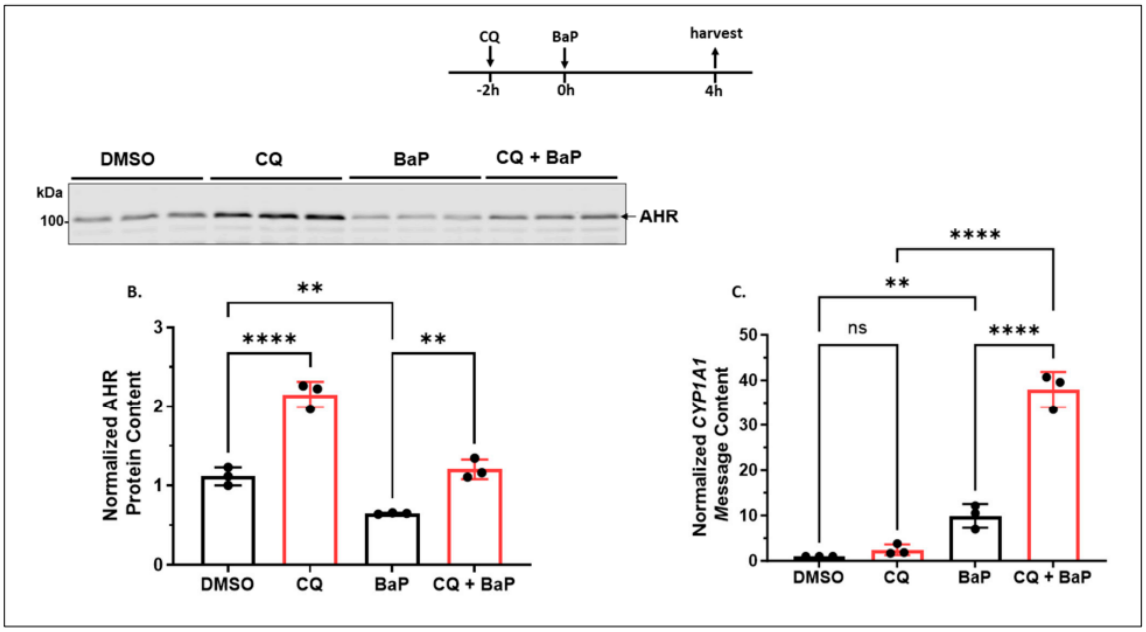

Note. (A) Western blot results of cells treated with 0, 60 or 100 μM CQ for 6h. The images above are biological triplicates of one experiment. (B) Western blot results of cells treated with 100 μM CQ for 6h. At 2h post CQ treatment, cells were co-treated with DMSO or 5 μM BaP for the remaining 4h. The images above are biological triplicates of one experiment. (C) RT-qPCR results of *cyp1a1* message level. Each experiment was with biological triplicate and was repeated once with similar results. The plots showed as the means with error bars (means ± SD, n = 3). The statistical significance of the differences between group means are evaluated by one-way ANOVA using Tukey test for multiple comparisons.

6-AN reduces the AHR protein content of A549 cells in a dose- and time-dependent manner with functional relevance

Next, we used activators of either selective macroautophagy or CMA to explore the autophagy mechanism for AHR degradation in A549 cells. Treatment with 6-AN, a

CMA activator, caused a dose-dependent reduction of the AHR protein content (Fig. 2.2A). This reduction was time-dependent as well, supporting that activation of CMA can effectively reduce the AHR protein content in A549 cells (Fig. 2.2B). When comparing to the reduction of the AHR protein content upon ligand (BaP) treatment, both 6-AN and BaP reduced the AHR protein content to a similar extent after 24-hour treatment. This prolonged suppression of the AHR levels is not surprising since TCDD and 3MC can cause similar suppression of AHR for 24h in Hepa1c1c7 cells [78]. However, unlike the BaP-induced AHR proteasomal degradation, the reduction of the AHR protein content by 6-AN was reversed in the presence of an autophagy inhibitor (CQ), but not a proteasomal inhibitor (MG132) (Fig. 2.2C and D). Treatment with MG132 even suppressed the AHR protein content further. This is consistent with our finding that treatment of A549 cells with MG132 alone for 6h also reduced the AHR protein levels and this reduction was reversed in the presence of CQ (Fig. 2.2E), which can be explained by the literature report that MG132 can induce autophagy [79, 80]. In fact, lactacystin, another proteasomal degradation inhibitor, has been reported to activate autophagy partly by upregulating LC3 expression [81]. Interestingly, MG132 reversed the inhibition of AHR autophagy by CQ (Fig. 2.2E), consistent with the notion that AHR undergoes autophagy and MG132 can activate autophagy to degrade AHR. However, both metformin (Met) and rapamycin (Rap), which are selective macroautophagy activators, did not reduce but increased the AHR protein content (Fig. 2.2F and G). This increase can be explained by the crosstalk between selective macroautophagy and CMA that activation of one autophagy mechanism may negatively regulate the other [82]. In any case, selective macroautophagy does not seem to be

involved in the degradation of AHR in A549 cells. To address whether 6-AN can suppress AHR function, we examined the effect of 6-AN on the ligand-induced, AHR dependent activation of the *cyp1a1* gene transcription. We observed that both BaP (5 μM) and FICZ (1 μM) upregulated the *cyp1a1* message by 10- and 20-fold, respectively, after 6 hours of treatment (Fig. 2.2H). 6-AN (100 μM) effectively suppressed the induction to less than 5-fold in both cases, showing that reduction of the AHR protein content by 6-AN to about 40% of its content in A549 cells significantly hampered its function.

Fig. 2.2

6-AN decreased the AHR protein level via CMA and suppressed the ligand-induced activation of its target gene transcription in A549 cells.

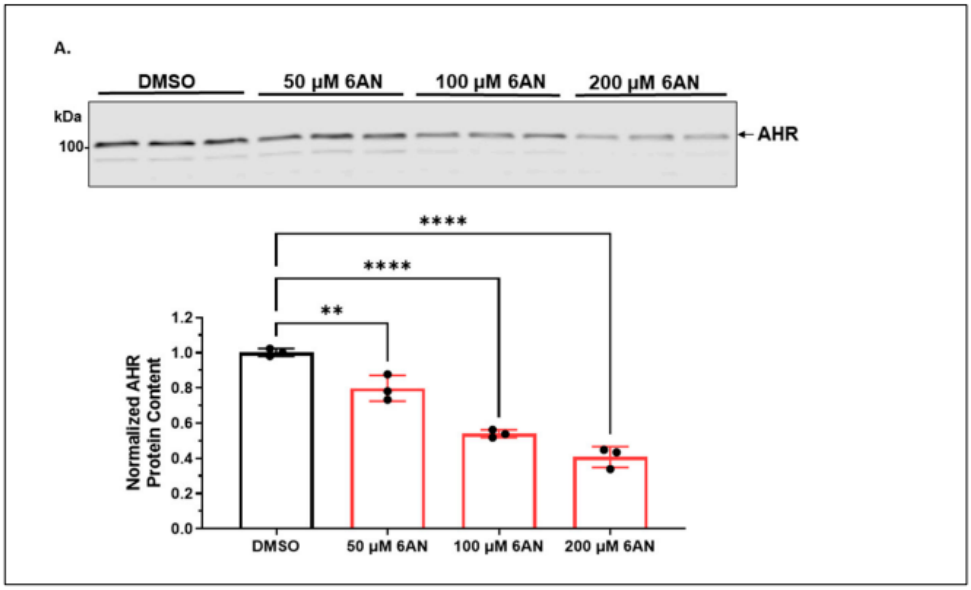

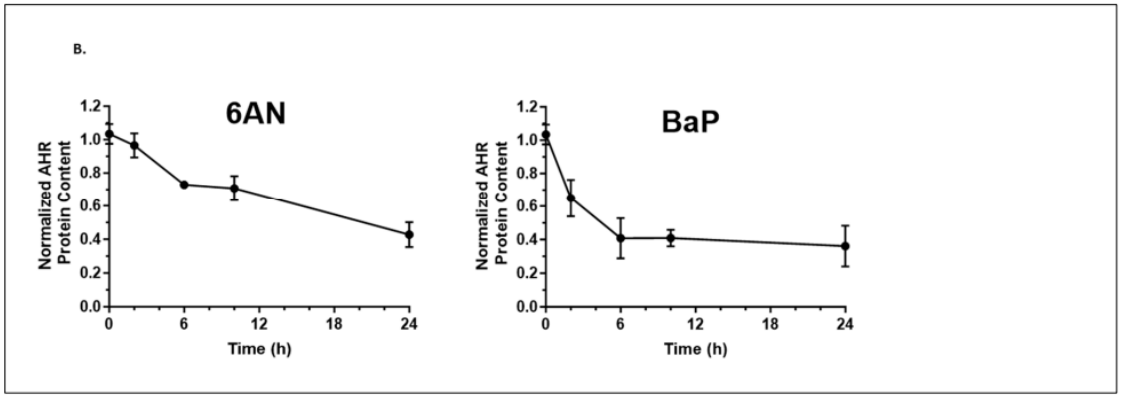
B.
6AN
BaP
Normalized AHR Protein Content
Time (h)

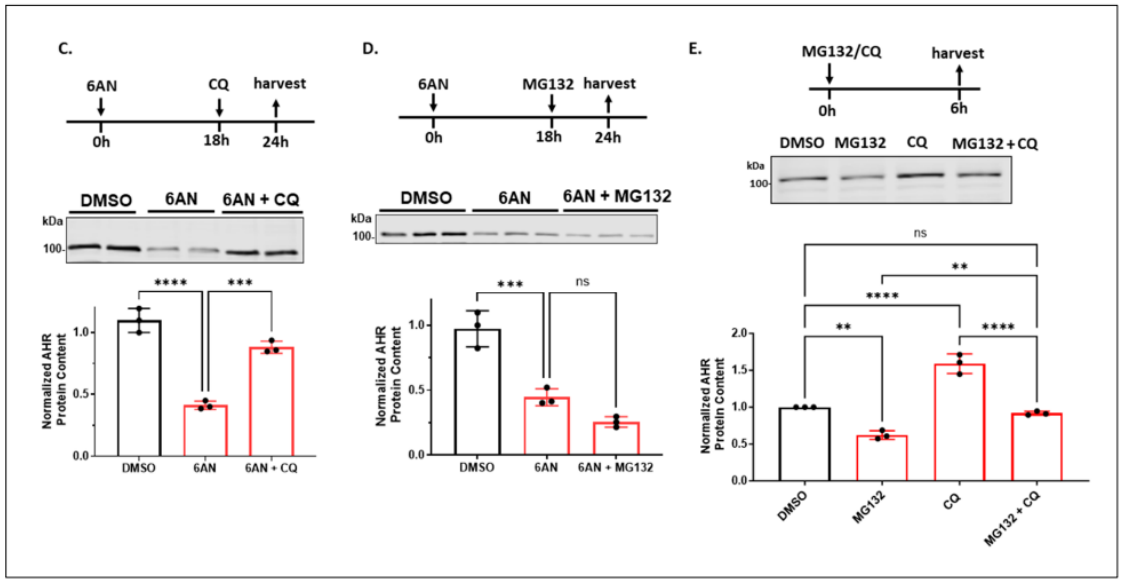
C.
6AN
CQ
harvest
0h
18h
24h
DMSO
6AN
6AN + CQ
kDa
100
Normalized AHR Protein Content
D.
6AN
MG132
harvest
6AN + MG132
E.
MG132/CQ
DMSO
MG132
CQ
MG132 + CQ
ns

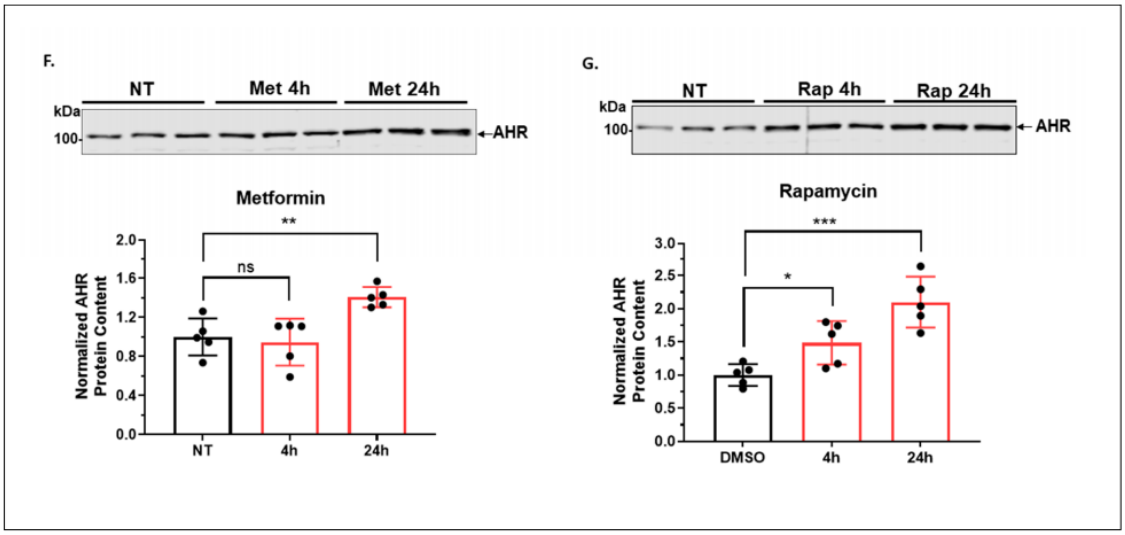
F.
NT
Met 4h
Met 24h
AHR
Metformin
G.
Rap 4h
Rap 24h
Rapamycin
Normalized AHR Protein Content
4h
24h

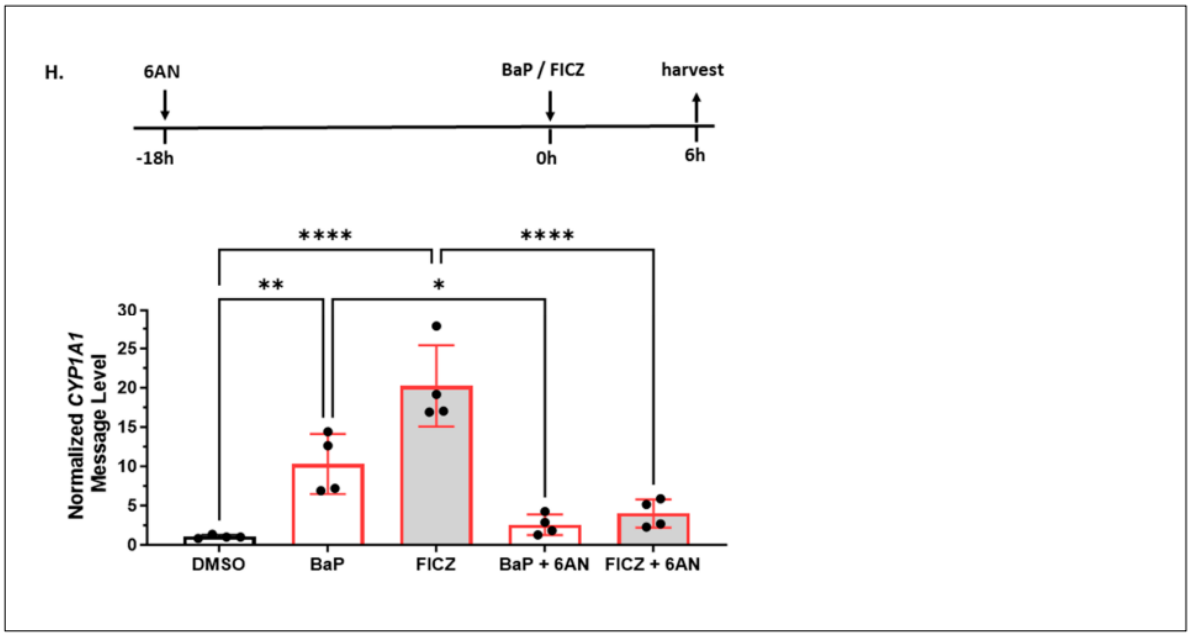

Note. (A) Western blot results of cells treated with DMSO or 6-AN (50, 100 or 200 μM) for 24h. The images above are biological triplicates of one experiment. (B) Western blot results of cells treated with 100μM 6-AN (B, left panel) or 5μM BaP (B, right panel) for 0, 2, 6, 10 or 24h. Each time point represents means ± SD, n = 3. (C) Western blot results of cells pretreated with DMSO or 100 μM 6-AN for 18h, followed by 100 μM CQ treatment for an additional 6h. The images above the plot are biological duplicates of one experiment. This experiment was repeated one more time to generate the plot. (D) Western blot results of cells pretreated with DMSO or 100 μM 6-AN for 18h followed by 10 μM MG132 treatment for an additional 6h. The images above the plot are biological triplicates of one experiment. This experiment was repeated once with similar results. (E) Western blot results of cells treated with DMSO, 10 μM MG132, 100 μM CQ or 10 μM MG132 plus 100 μM CQ for 6h. The images are representatives of the plotted data. All plots are the means with error bars (means ± SD, n = 3). (F) Western blot results of cells treated with 4 mM metformin (Met) for 0, 4 or 24h. The plot represents the means

with error bars (means ± SD, n = 5). The images above are biological triplicates of one experiment. The statistical significance of the differences between group means are evaluated by one-way ANOVA using Tukey test for multiple comparisons. (G) Western blot results of cells treated with 0.5 μM rapamycin (Rap) for 0, 4 or 24h. The plot represents the means with error bars (means ± SD, n = 5). The images above are biological triplicates of one experiment. (H) RT-qPCR results of cells pretreated with DMSO or 100 μM 6-AN for 18h, followed by BaP (5 μM) or FICZ (1 μM) treatment for another 6h. Experiment was performed with biological triplicates and was repeated once with similar results. The plot represents the means with error bars (means ± SD, n = 3). The statistical significance of the differences between group means are evaluated by one-way ANOVA using Tukey test for multiple comparisons.

Knockdown of LAMP2 in A549 cells abolishes the CQ-mediated increase of the AHR protein content

LAMP2A, a lysosomal membrane bound protein, is responsible for the internalization of CMA substrates into lysosomes for degradation. To further address whether CMA could degrade AHR in A549 cells, we used shRNA to knockdown the LAMP2 messages, which include the LAMP2A message, in A549 cells to see whether the AHR protein content is affected when CMA is less active. Using LAMP2 specific shRNA/siRNA to knockdown the LAMP2A message is a common approach to downregulate LAMP2A expression. We observed that the AHR protein content increased to 1.7-fold when LAMP2 is down-regulated (Fig. 2.3A), suggesting that LAMP2A plays a role in the degradation of AHR. Results from the LAMP2 western

showed a stretch of the LAMP2 region which represented both LAMP2A and LAMP2B. Additionally, CQ was unable to increase the AHR protein content when LAMP2 was downregulated, supporting that AHR is degraded via CMA in A549 cells. In contrast, knocking down ATG5, which is necessary for LC3 lipidation into LC3-phosphatidylethanolamine conjugate (LC3-II) during the formation of autophagosomes, decreased the AHR protein levels to 76% when compared to the wild-type A549 cells, suggesting that ATG5 is not involved in the degradation of AHR (Fig. 2.3B). The reduction of the AHR content could be the compensatory mechanisms that might activate CMA, since this kind of crosstalk between selective macroautophagy and CMA has been reported in the literature [82]. Treatment with CQ did not change the extent of the AHR protein content increase between the wild-type and ATG5 knockdown cells, suggesting that selective macroautophagy is not involved in AHR degradation in A549 cells.

Degradation of AHR via CMA is dependent on the NEKFF motif of AHR in A549 cells

Earlier, we reported that NEKFF at amino acids 558-562 of the human AHR could be the CMA motif that allows interaction with HSC70, followed by recruitment to LAMP2A for degradation [75]. To further investigate the CMA-mediated AHR degradation in A549 cells, we examined the necessity of NEKFF for AHR degradation. We had previously generated a few GFP fusions of the wild-type human AHR and its mutants by altering the NEKFF sequence via site-directed mutagenesis [75]. We confirmed the sequence by sequencing the whole AHR cDNAs of the GFP-AHR (NEKFF) and the GFP-AHR mutant (NAKAF). Although the only differences in the

amino acid sequence between the GFP-AHR (558-NEKFF-562) and GFP-AHR mutant (558-NAKAF-562) were E559A and F561A, we noticed two random mutations resulting in I581T and S590N when compared to the published human AHR cDNA sequence (NM_001621). To minimize any interference of the A549 AHR on the degradation of the GFP-AHR and GFP-AHR mutant due to shared machinery, we transfected the GFP plasmid into the *AHR* knockout A549 cells. First, we generated five clones of *AHR* knockout A549 cells using the clustered regularly interspaced short palindromic repeats/ CRISPR-associated protein 9 (CRISPR/Cas9) strategy, namely 4H2, 2F6, 3C9, 5F2, and 5G11 (Fig. 2.3C). Using the Synthego ICE knockout online analysis software, all clones were 100% edited with insertion or deletion (% indel score) and clone 5G11 was determined to be a homologous bi-allelic knockout with 47 nucleotide deletions at exon 2, resulting in a frame-shift mutation. Both wild type and mutant AHR cDNAs were cloned downstream to the GFP cDNA, followed by transient transfection into the *AHR* knockout A549 5G11 cells. The GFP fusion of the wild-type AHR containing NEKFF showed similar suppression as the A549 AHR when treated with 100 μM 6-AN for 24h (Fig. 2.3D vs. 2.2A). However, the GFP fusion of the NAKAF mutant was resistant to degradation upon 6-AN treatment, supporting that NEKFF is the CMA motif and AHR undergoes the CMA-mediated degradation. This observation is consistent with our immunoprecipitation results that treatment with CQ enhanced the interactions of AHR with HSC70 and LAMP2 in vitro (Fig. 2.3E). These interactions were also observed in MDA-MB-468 cells [75].

Fig. 2.3

Lysosomal degradation of AHR required LAMP2A and the presence of its CMA motif in A549 cells.

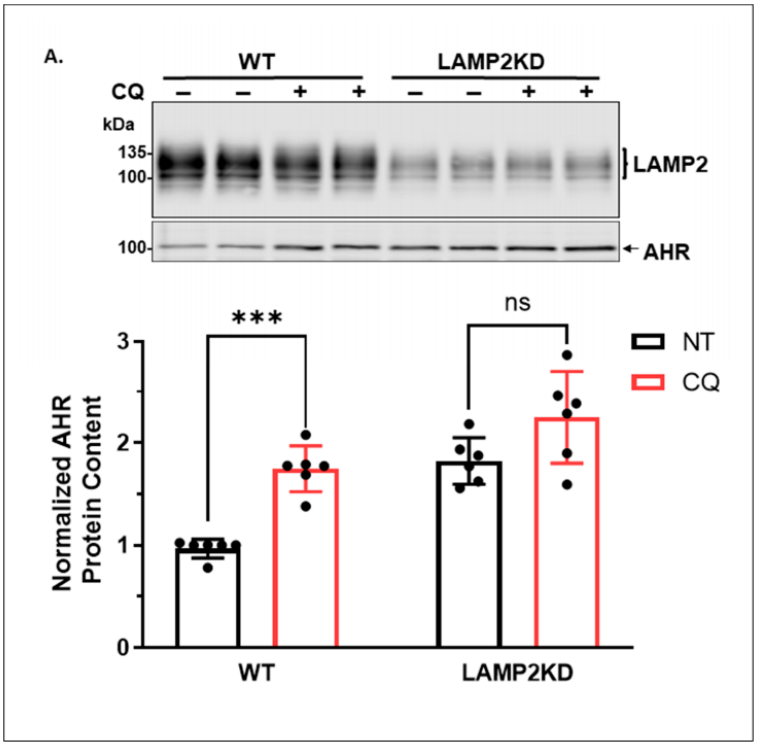

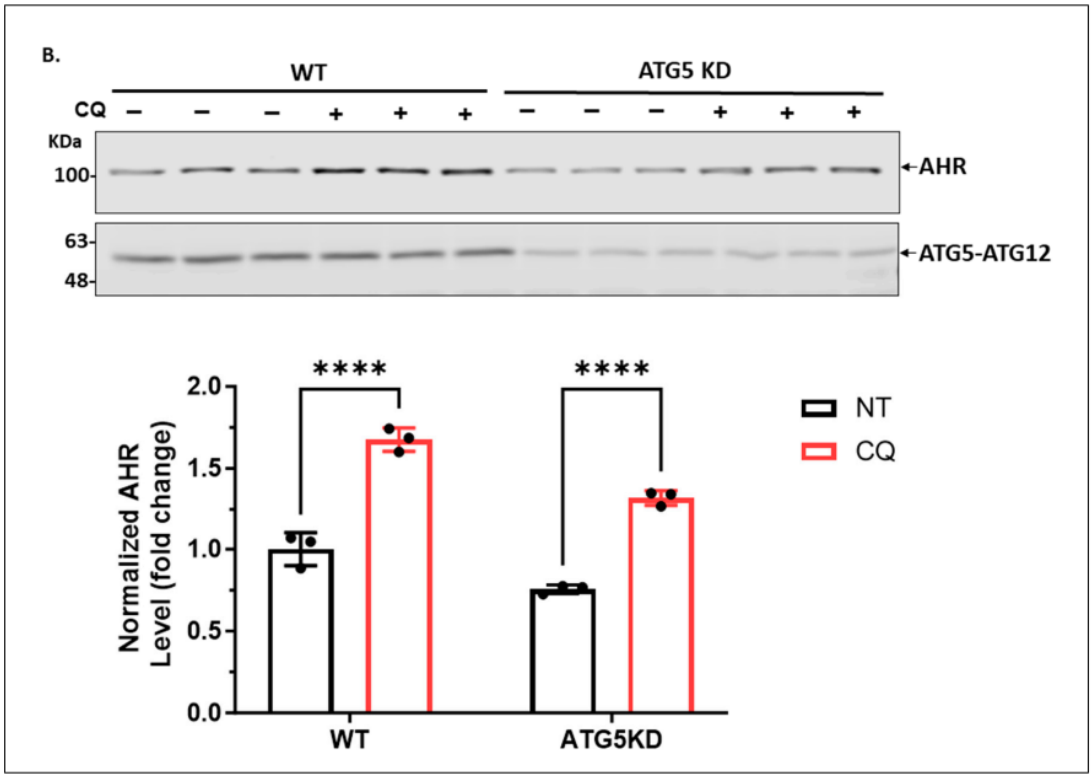

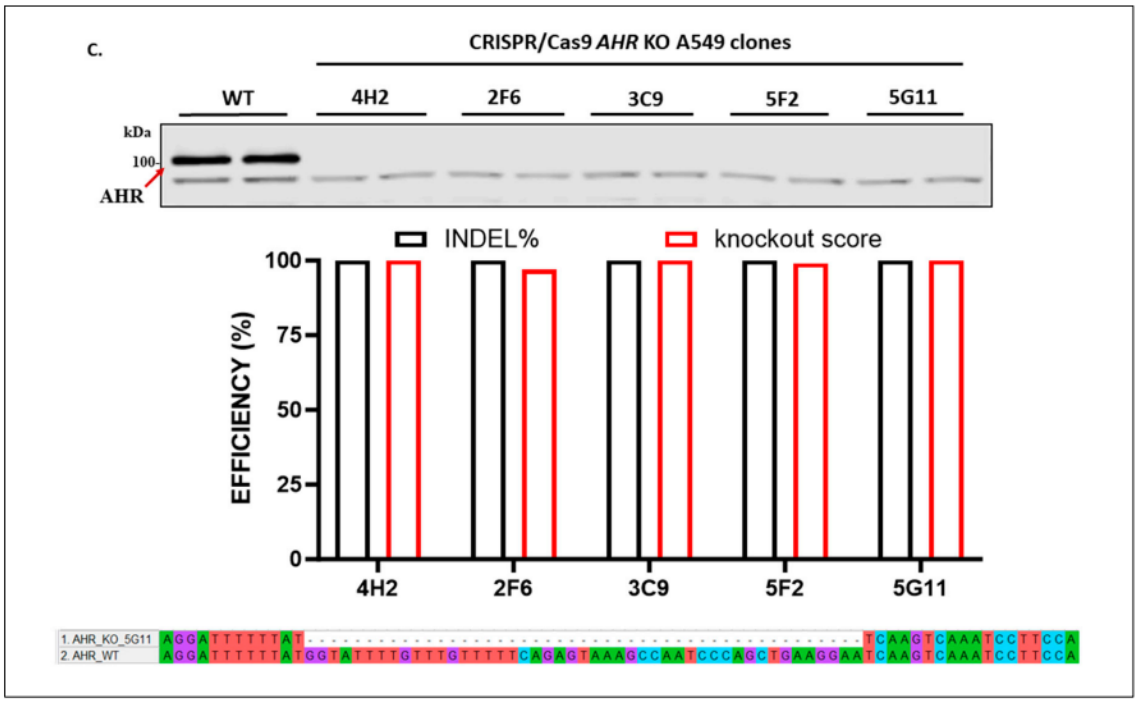
C.
CRISPR/Cas9 AHR KO A549 clones
WT
4H2
2F6
3C9
5F2
5G11
kDa
100
AHR
INDEL%
knockout score
EFFICIENCY (%)
100
75
50
25
0
4H2
2F6
3C9
5F2
5G11
1. AHR_KO_5G11
2. AHR_WT

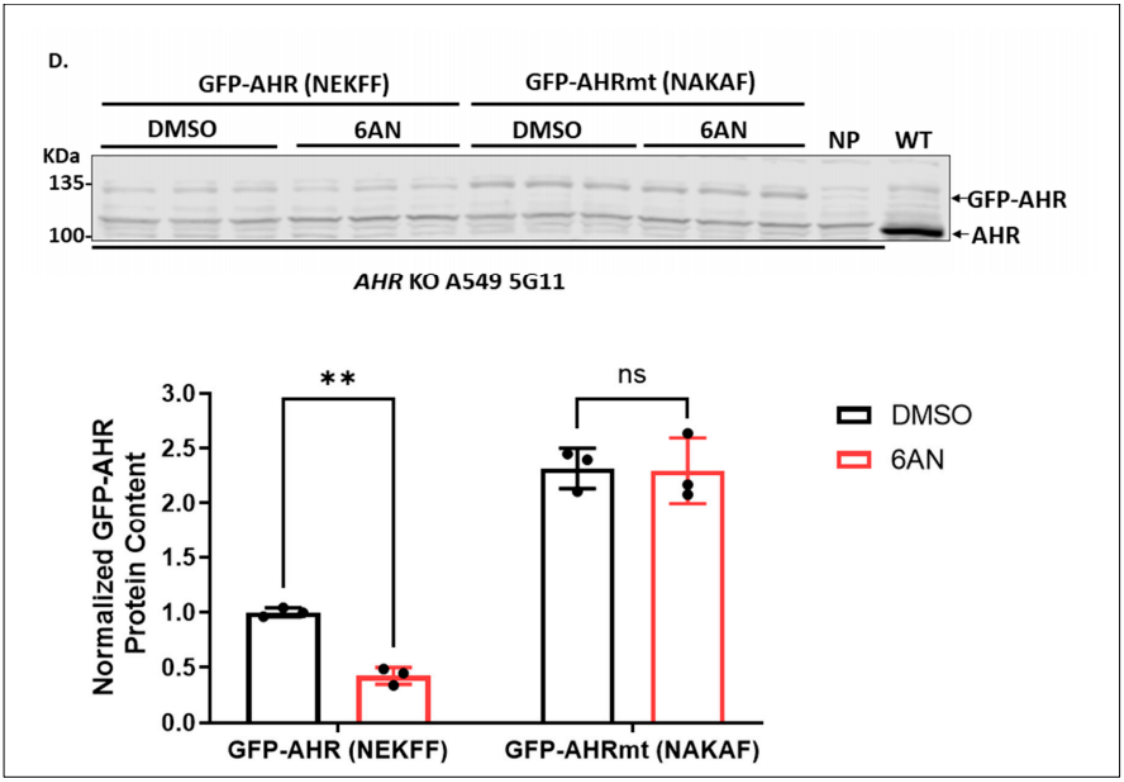
D.
GFP-AHR (NEKFF)
GFP-AHRmt (NAKAF)
DMSO
6AN
DMSO
6AN
NP
WT
KDa
135
100
GFP-AHR
AHR
AHR KO A549 5G11
**
ns
Normalized GFP-AHR Protein Content
3.0
2.5
2.0
1.5
1.0
0.5
0.0
DMSO
6AN
GFP-AHR (NEKFF)
GFP-AHRmt (NAKAF)

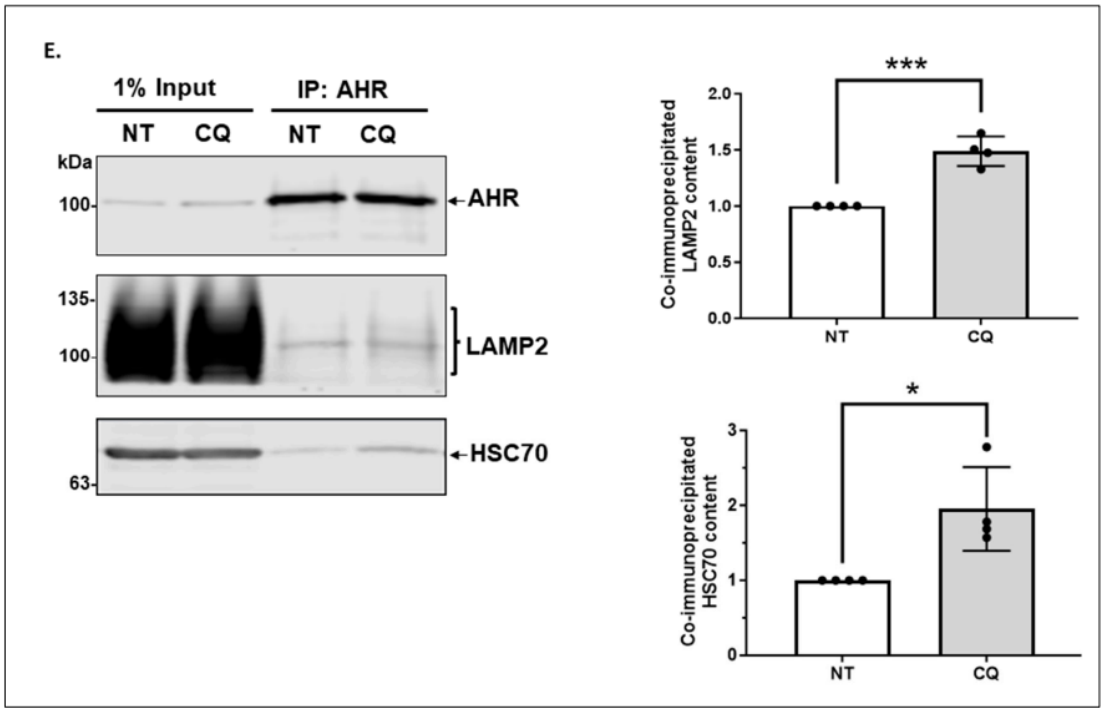

Note. (A) Western blot results of A549 wild-type (WT) and LAMP2 stable knockdown (LAMP2KD) cells treated with or without 100 μM CQ for 6h. Stable knockdown cells contain 30% of the wild-type LAMP2 content. Mature LAMP2, including LAMP2A, is highly glycosylated with a total molecular weight of about 100~130kDa. The plot represents the means with error bars (means ± SD, n = 6). The images above are biological duplicates of one experiment. (B) Western blot results of A549 wild type (WT) and ATG5 stable knockdown (ATG5KD) cells treated with or without 100 μM CQ for 6h. Stable knockdown cells contain 28% of the wild-type ATG5 content. Intracellular ATG5 is conjugated with ATG12. In western blot, a band at ~55 kDa represents the ATG5-ATG12 complex. The images are biological triplicates from one experiment and the experiment was repeated once with similar results. (C) CRISPR/Cas9-mediated knockout of *AHR* gene in A549 cells. Western blot analysis of AHR protein levels in wild-type (WT) and five CRISPR/Cas9 *AHR* knockout (KO) clones. Sequencing alignment showed that

clone 4H2, 2F6, 3C9, and 5F2 are heterozygous compound knockout. The plot indicates the INDEL efficiencies and knockout scores from the online Inference of CRISPR Edits (ICE) analysis. Clone 5G11 is homozygous knockout with 47 nucleotides deleted in the exon 2 region of *AHR* genomic DNA, leading to a frameshift deletion. (D) Western blot results of cells transiently expressing GFP-AHR wild type (NEKFF) or GFP-AHR mutant (NAKAF) treated with DMSO or 6-AN for 24h after 48h post-transfection. The plot represents the means with error bars (means ± SD, n = 3). Experiment was performed with biological triplicates and was repeated once with similar results. The images represent the biological triplicates of one experiment. NP represents A549 cells that have undergone the transfection process without the GFP plasmid whereas WT is the wild-type A549 cells. (E) Co-immunoprecipitation results of cells treated with or without 100 μM CQ for 6h. Anti-AHR antibody SA210 was used for immunoprecipitation of AHR (IP). 1% input represents 1% of the total protein lysate used for immunoprecipitation. The plot represents the means with error bars (means ± SD, n = 4). The images are representative of the plotted data. The statistical significance was evaluated by one-way (E) or two-way (B-D) ANOVA using Tukey test for multiple comparisons.

Autophagy of AHR is ongoing in the background while AHR is undergoing rapid degradation via the ubiquitin-proteasome system after treatment with an AHR ligand in A549 cells

It is well accepted that upon ligand treatment, AHR undergoes proteasomal degradation within hours of treatment [77]. We were interested in how autophagy of

AHR is affected by ligand treatment in A549 cells. As expected, AHR was degraded to 40% of its wild-type content within 2h of 5 μM BaP treatment via 26S proteasome since cotreatment with 10 μM MG132 completely reversed the degradation (Fig. 2.4A). Cotreatment of BaP-treated cells with 100 μM CQ, however, increased the AHR protein levels to 1.8-fold when compared to cells treated with BaP alone. This fold change was close to the increase we observed when we treated A549 cells with 100 μM CQ for 6h (Fig. 2.1A), suggesting that AHR underwent the usual rate of degradation via autophagy while proteasomal degradation of AHR was triggered by a ligand. Interestingly, cotreatment of A549 cells with 5 μM BaP and 10 μM MG132 for an additional 4h (a total of 6h) showed that the AHR protein levels was pronouncedly dropped to less than 30% content (Fig. 2.4A and B). Considering that MG132 can activate autophagy, we examined the possibility that AHR underwent autophagy between the second and the sixth hours of MG132 treatment. We exposed the BaP-treated cells with both MG132 and CQ for 6h and observed only a 2-fold increase of the AHR protein levels (from 29% to 58%) (data not shown). The strong reduction of the AHR protein levels from the second to the sixth hours of MG132 treatment cannot be fully explained by merely lysosomal degradation of AHR. The AHR protein levels were similar from 6h up to 24h after BaP treatment (Fig. 2.2B, right). Interestingly, similar inhibition of AHR autophagy by CQ was observed within the 6h to 24h period since 1.5 to 1.8-fold increase of the AHR levels was observed when we compared BaP and BaP/CQ treatment groups (Fig. 2.4A-D). Fig. 2.4E was the representative Western images of Fig. 2.4A-D, which showed that from 6h to 24h, the AHR levels were increased in the presence of CQ

whereas MG132 did not have any effect. Collectively, we concluded that autophagy is likely involved for maintaining the AHR levels after ligand treatment.

Fig. 2.4

Lysosomal degradation of AHR was ongoing in the background while AHR underwent rapid proteasomal degradation after ligand treatment in A549 cells.

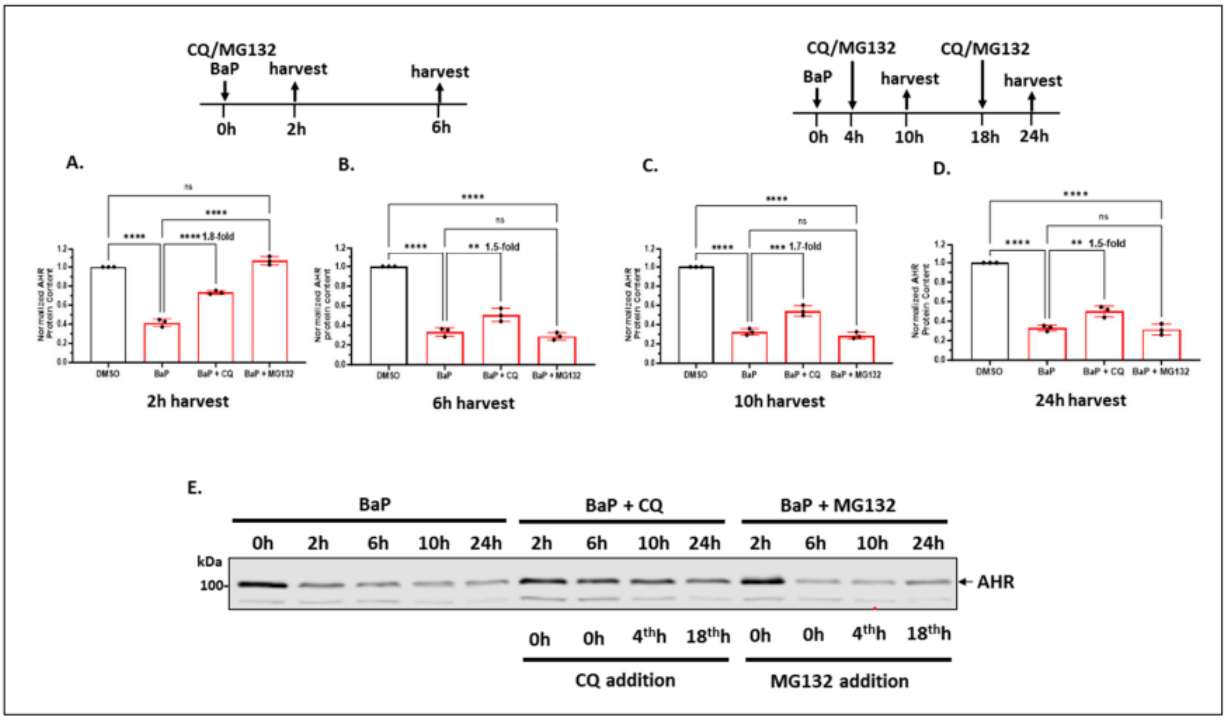

Note. Cells were treated with 5 μM BaP (or DMSO), 100 μM CQ (or water), and 10 μM MG132 (or DMSO) in different combinations, followed by Western blot analysis of the AHR content. Treatment conditions are diagrammed above the plots in A-D. The plots represent the means with error bars (means ± SD, n = 3). Experiment was performed with biological triplicates and was repeated once with similar results. The statistical significance of the differences between group means are evaluated by one-way ANOVA using Tukey test for multiple comparisons. (E) A representative of the western images of A-D in one Western blot analysis.

Autophagy is not involved in the quick-onset degradation of AHR triggered by low dose of geldanamycin (GA) but is involved in controlling the AHR levels after both low and high doses of GA treatment in A549 cells

It is known that treatment with a low dose of GA (0.1 μM) causes proteasomal degradation of AHR [83]. We examined whether autophagy might also be involved in this GA-mediated degradation. Our results showed that treatment with a low dose of GA (0.1 μM) for 2h caused pronounced reduction of the AHR content to 17% in A549 cells which could be partially reversed to 41% content by 10 μM MG132 (Fig. 2.5A). The fact that MG132 could reverse 100% of the BaP-mediated degradation of AHR (Fig. 2.4A) but to a much lesser extent with the GA-mediated degradation of AHR (Fig. 2.5A) suggested that the GA effect on AHR degradation is more complex than merely proteasomal degradation. On the other hand, inhibition of autophagy by CQ (100 μM) did not alter the low AHR levels caused by 0.1 μM GA. Realizing that a low dose of GA (0.5 μM) could inhibit autophagy by suppressing the Atg7, Beclin-1, and ULK1 protein levels, as reflected by reduction of the autophagic flux [84], AHR degradation via autophagy might have been inhibited in the presence of 0.1 μM GA. Although two additional hours of GA exposure (which was 4h treatment) did not further suppress AHR but rather a slight increase in content (28% vs. 17%), MG132 restored more AHR content when compared to 2 h (66% vs. 41%). These results suggested that there might be newly synthesized AHR between 2 and 4 hours that was degraded by proteasomal degradation (Fig. 2.5B). In addition, CQ also increased the AHR content from 28% to 43%, suggesting autophagy was also at play between the second and the fourth hours of GA treatment.

It has been reported that treatment with a high dose of GA (2-10 μM) for 24h causes degradation of IKK via the ATG5-dependent autophagy in 293, HeLa, and B and T cells [85]. Activity of CMA is doubled when IMR-90 cells are treated with 2 μM of GA [86]. Therefore, we examined whether autophagy and proteasomal degradation might play a role in the sustained low levels of AHR many hours after a high dose of GA treatment. We treated the cells with 1 μM GA (high dose) for 24h, followed by exposure to CQ, MG132, or the DMSO vehicle in the last 6h before harvesting in A549 cells. We used 1 μM because higher dose (2 μM) of GA caused apparent cell death after 24h. We observed that CQ increased the AHR levels significantly from 29 to 58% whereas MG132 did not alter the AHR levels in a statistically significant manner (Fig. 2.5C and D), showing that autophagy, but not proteasomal degradation, is essential for maintaining the AHR protein levels. The slight reduction of AHR levels by MG132 in this case is probably due to the activation of autophagy by MG132, as observed in Fig. 2.2D and E. Results from the time-dependent experiment showed that high dose of GA suppressed the AHR protein levels more effectively than low dose of GA (Fig. 2.5E), supporting that high dose of GA causes more AHR degradation, possibly through autophagy. However, we cannot rule out the possibility that higher dose of GA may also cause an increase of the proteasomal degradation of AHR. Collectively, AHR undergoes autophagy which can be triggered by high dose of GA and blocked by CQ (Fig. 2.5C and E).

Fig. 2.5

Lysosomal degradation of AHR occurred after A549 cells were treated with low or high dose of GA.

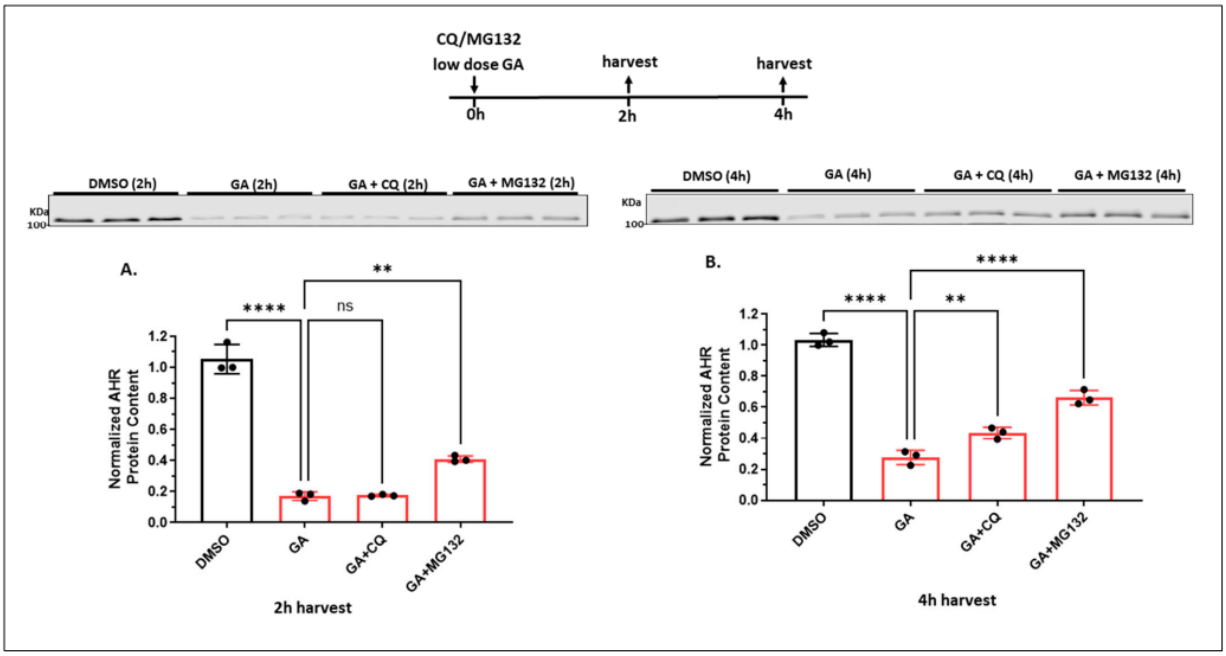

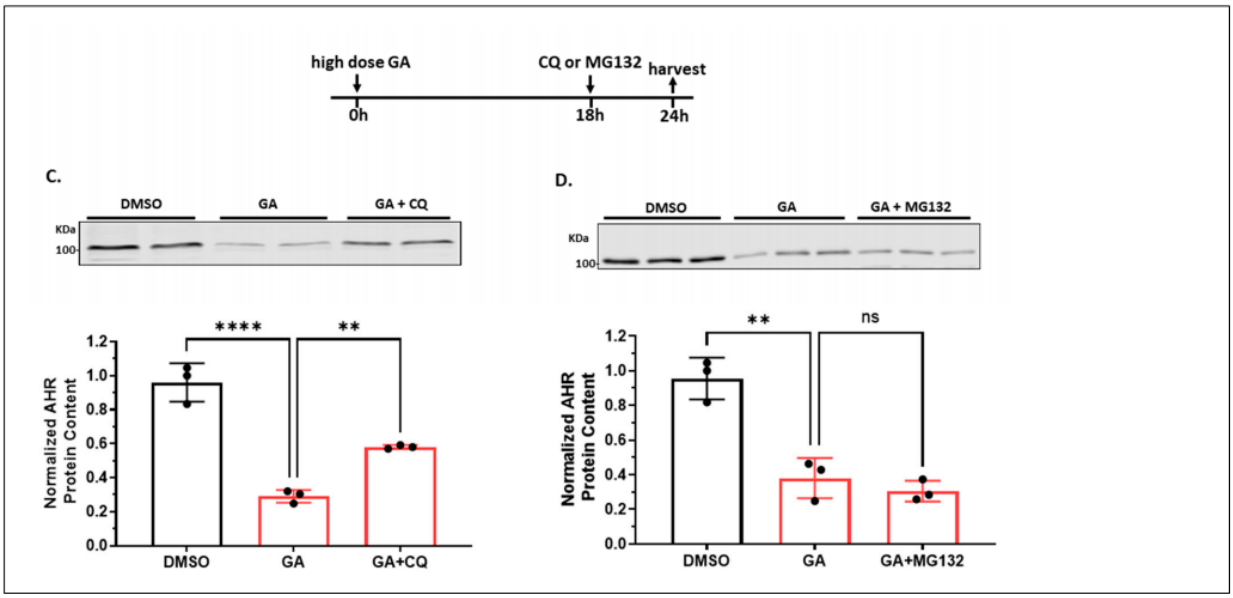

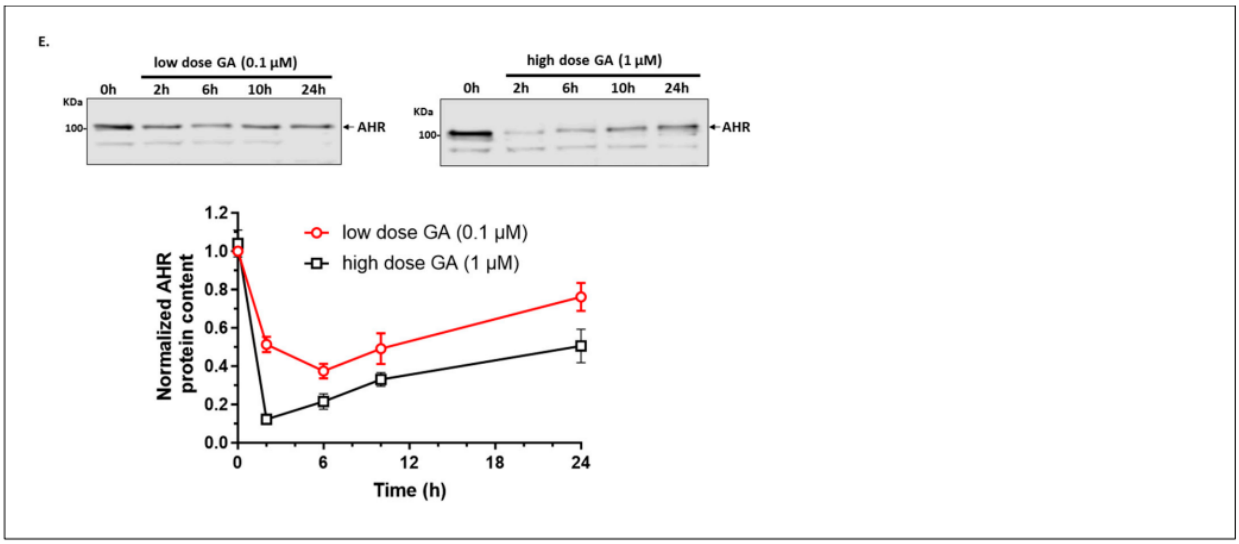

Note. Western blot results of cells treated with DMSO, 0.1 μM GA (low dose), 0.1 μM GA plus 100 μM CQ or 0.1 μM GA plus 10 μM MG132 for 2h (A) or 4h (B). The images represent the biological triplicates of one experiment. (C) Western blot results of cells pretreated with 1 μM GA (high dose) for 18h, followed by 100 μM CQ treatment for another 6h. The images represent the biological duplicates of one experiment. (D) Western blot results of cells pretreated with 1 μM GA (high dose) for 18h, followed by 10 μM MG132 treatment for another 6h. The images represent the biological triplicates of one experiment. For A-D, all plots represent the means with error bars (means ± SD, n = 3); all experiments were performed with biological triplicates and were repeated once with similar results; the statistical significance of the differences between group means are evaluated by one-way ANOVA using Tukey test for multiple comparisons. (E) A plot showing the western blot results of cells treated with either low dose of GA (0.1 μM) or high dose of GA (1 μM) for 0, 2, 6, 10 or 24h. Each time point represents means ± SD, n = 3.

6-AN is not an AHR ligand

Although our data supported that 6-AN activates CMA to degrade AHR, we examined whether 6-AN is also an AHR ligand, knowing that binding of an AHR ligand normally causes AHR protein degradation. For this experiment, we used the rat H4G1.1c3 cells stably expressing the DRE-driven GFP protein [75]. Treating these cells with a prototypical AHR ligand such as BaP and FICZ for 12 hours caused the GFP expression that could be captured by fluorescence microscopy (Fig. 2.6). This GFP fluorescence was suppressed in the presence of an AHR antagonist CH223191, supporting that the fluorescence corresponded to the AHR ligand-activated GFP expression. We observed that 100 μM 6-AN, which caused AHR protein degradation at that concentration, did not show any more fluorescence than the DMSO vehicle control, supporting that 6-AN is not an AHR ligand. We also determined that both MG132 (10 μM) and GA (0.1 μM) did not cause GFP expression and are not AHR ligands; however, all of them (6-AN, MG132, and GA) can reduce the AHR protein levels (Fig. 2.2A, 2.2E and 2.5A).

Fig. 2.6

6-AN, (S)-MG132, and GA are not AHR ligands.

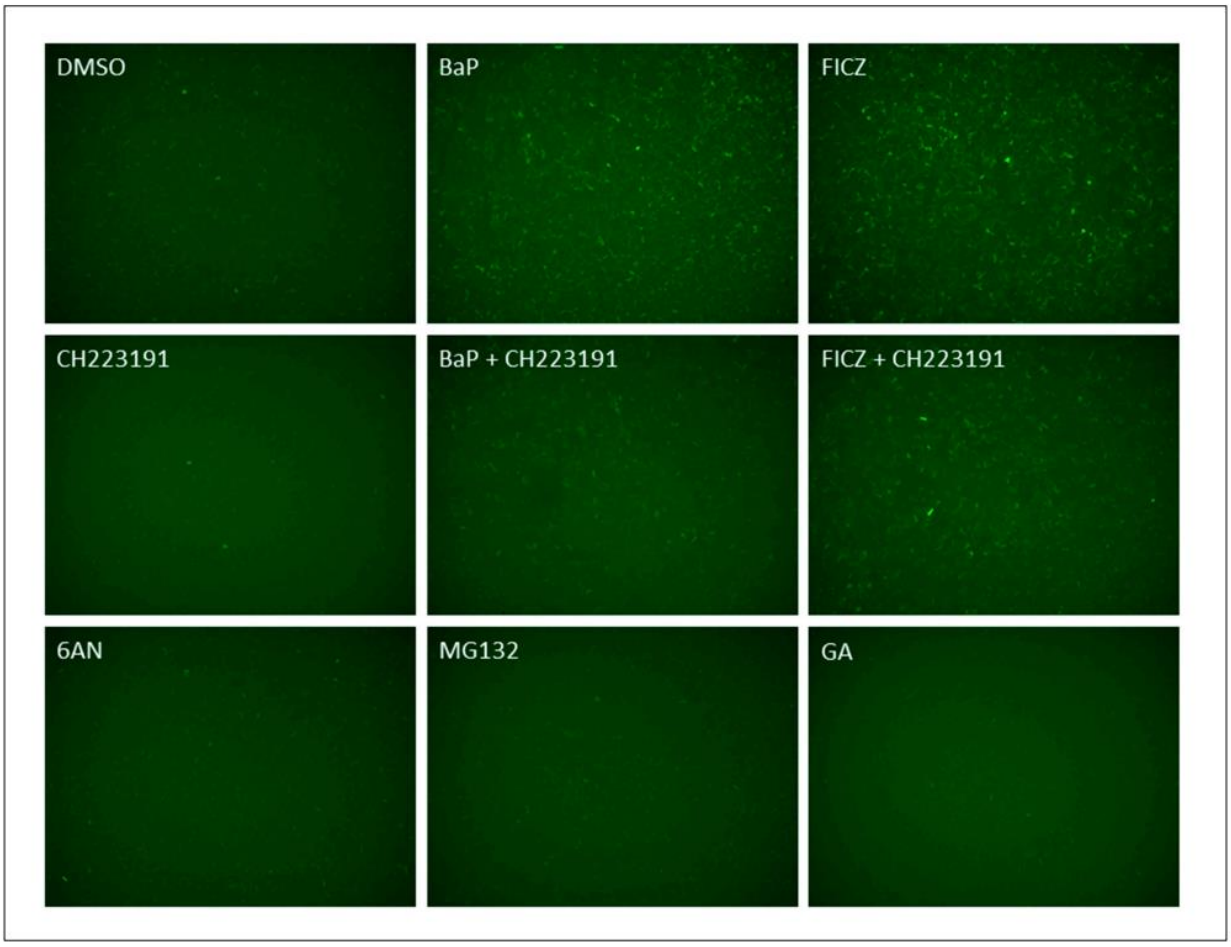

Note. Treatment with 6-AN, MG132, GA, BaP, FICZ, and CH223191 in rat H4G1.1c3 stable cells carrying a DRE-driven GFP cDNA. Cells were treated for 12h with 0.2% DMSO, 100 μM 6-AN, 10 μM MG132, 100 nM GA, 5 μM BaP, 1 μM FICZ, 10 μM CH223191, 5 μM BaP plus 10 μM CH223191, or 1 μM FICZ plus 10 μM CH223191. The experiment was repeated two more times with similar results. Magnification: 4x.

AHR promotes migration of A549 cells in a wound healing assay

There have been conflicting reports on the role of AHR in cell migration and metastasis, particularly on lung epithelial cells that some researchers showed

suppression of migration and metastasis by AHR using the knockdown approach in A549 cells [63]. Here, we used our *AHR* knockout (5G11) A549 cells to determine the role of AHR on cell migration in a wound healing assay. We observed that A549 cells migrated slower when AHR protein was absent (Fig. 2.7A). Promoting CMA by 100 μM 6-AN treatment of A549 cells for up to 48h showed similar retardation of migration as observed in *AHR* knockout 5G11 cells. This inhibition of cell migration by 6-AN was expected since 6-AN was shown to suppress the migration of acute myelogenous leukemia cells by inhibiting enzymes involved in the pentose phosphate pathway [87]. However, this suppression of migration by 6-AN was abolished in *AHR* knockout 5G11 cells, supporting that this 6-AN effect on A549 cells is AHR dependent.

AHR promotes EMT in A549 cells

Next, we examined the role of AHR on EMT of A549 cells. We measured the transcript and protein levels of an epithelial marker E-cadherin and the mesenchymal markers vimentin and N-cadherin in wild-type and *AHR* KO 5G11 A549 cells. We observed that the transcript levels of E-cadherin and vimentin were 2.6- and 0.5-fold, respectively, in *AHR* knockout 5G11 cells when compared to the wild-type A549 cells (Fig. 2.7B), although the reduction of the vimentin transcript was not significant. The Western blot results showed that E-cadherin and vimentin proteins had the same trend as the transcripts, with a clear increase of E-cadherin and a decrease of vimentin in a statistically significant manner (Fig. 2.7C). These results clearly supported the fact that AHR favors the mesenchymal phenotype in A549 cells. However, there was no change in the N-cadherin transcript and protein levels in the presence or absence of AHR (Fig. 2.7B and C). Treatment of A549 cells with 100 μM 6-AN for 24h did not seem to alter

the E-cadherin and vimentin protein levels in A549 cells, and lacking AHR in 5G11 did not reveal any trend of the 6-AN effect that was AHR dependent (Fig. 2.7C). Realizing that there should be about 50% of AHR content after this 6-AN treatment, it is conceivable that 50% of AHR content might be sufficient to maintain the levels of these markers, and 6-AN might very well elicit some AHR-independent effect that complicated the picture. Next, we were interested to see any effect on these markers when the AHR content was increased < 2-fold by knocking down LAMP2 in A549 cells (Fig. 2.3A). We observed that vimentin was upregulated in LAMP2 knockdown A549 cells when compared to the wild-type A549 cells (Fig. 2.7D), consistent with the predicted pattern when AHR was upregulated. However, E-cadherin was also upregulated, showing a more complex picture that might be complicated by the inhibition of the CMA-mediated degradation of an EMT inhibitor when LAMP2 was downregulated. Downregulation of LAMP2 might also trigger partial EMT, causing cells to co-express both epithelial and mesenchymal markers. During partial EMT, the retained epithelial markers (such as E-cadherin) were shown to cluster cancer cells before migration [88]. Interestingly, upregulation of E-cadherin expression might not be sufficient to block invasion such as in the case of pancreatic cancer [89]. When we repeated the LAMP2 knockdown experiment using *AHR* knockout 5G11 cells, we observed that E-cadherin and vimentin were essentially unchanged when LAMP2 was knockdown, whereas a slight increase in N-cadherin levels was observed (Fig. 2.7E). When compared these results with the *AHR* knockout results in Fig. 2.7C, knocking down of LAMP2 appeared to suppress the E-cadherin and increase the vimentin levels, revealing a mesenchymal phenotype that was LAMP2 dependent but not AHR dependent.

To directly address the migration and invasion potential mediated by AHR, we conducted the Transwell assays to determine the migration and invasion potential of the wild-type and *AHR* knockout A549 cells. We observed that AHR significantly promoted cell migration and invasion by 2.1- and 1.8-fold, respectively, when we compared the *AHR* knockout 5G11 with the wild-type A549 cells (Fig. 2.7F and G). 6-AN similarly suppressed the migration and invasion of A549 cells by 1.9- and 3.2-fold, respectively, in an AHR dependent manner since this 6-AN effect was abrogated in the *AHR* knockout cells. Collectively, AHR clearly drives the invasion and migration of A549 cells. Activating the CMA degradation of AHR by 6-AN effectively slows down the invasion and migration of A549 cells in a mechanism that cannot be fully explained by the E-cadherin and vimentin levels.

Fig. 2.7

Suppression of the AHR protein level slowed down the epithelial-mesenchymal transition in A549 cells.

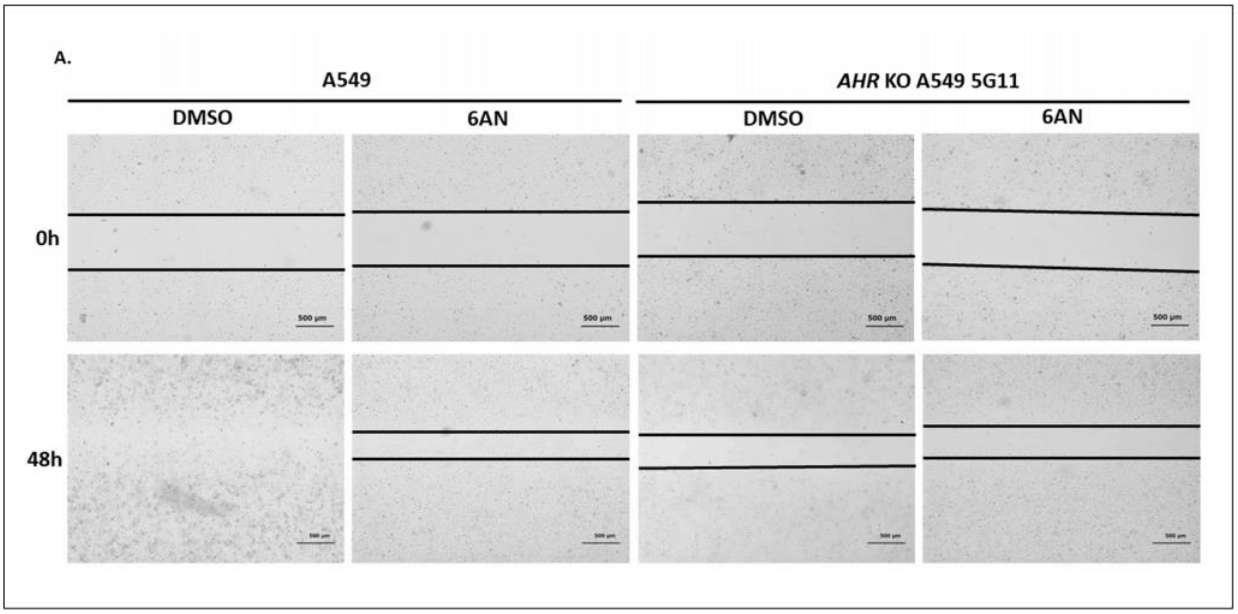

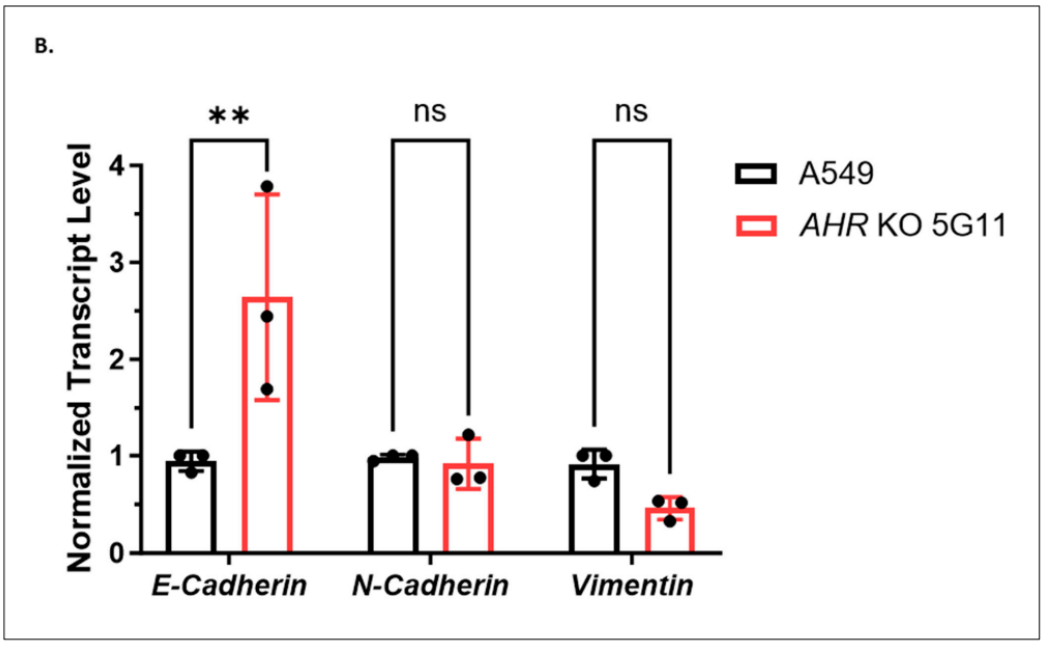
B.
**
ns
ns
Normalized Transcript Level
0
1
2
3
4
A549
AHR KO 5G11
E-Cadherin
N-Cadherin
Vimentin

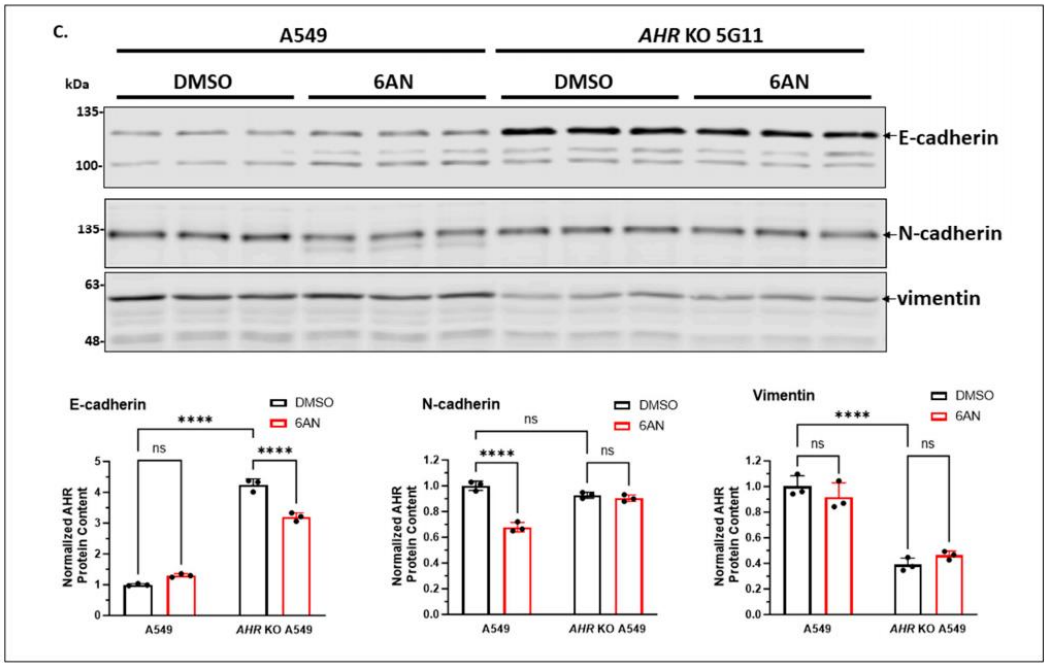
C.
A549
AHR KO 5G11
kDa
DMSO
6AN
DMSO
6AN
135
100
135
63
48
E-cadherin
N-cadherin
vimentin
E-cadherin
N-cadherin
Vimentin
DMSO
6AN
Normalized AHR Protein Content
****
ns
A549
AHR KO A549

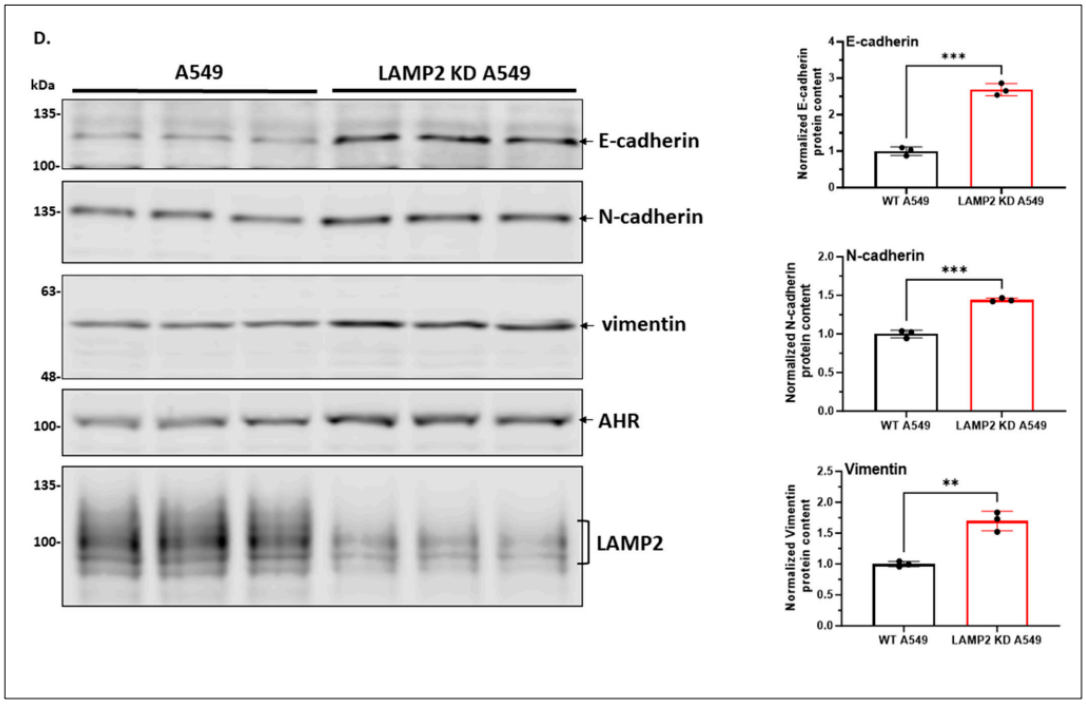
D.
A549
LAMP2 KD A549
kDa
135-
100-
E-cadherin
135-
N-cadherin
63-
48-
vimentin
100-
AHR
135-
100-
LAMP2
E-cadherin
***
Normalized E-cadherin protein content
WT A549
LAMP2 KD A549
N-cadherin
***
Normalized N-cadherin protein content
Vimentin
**
Normalized Vimentin protein content

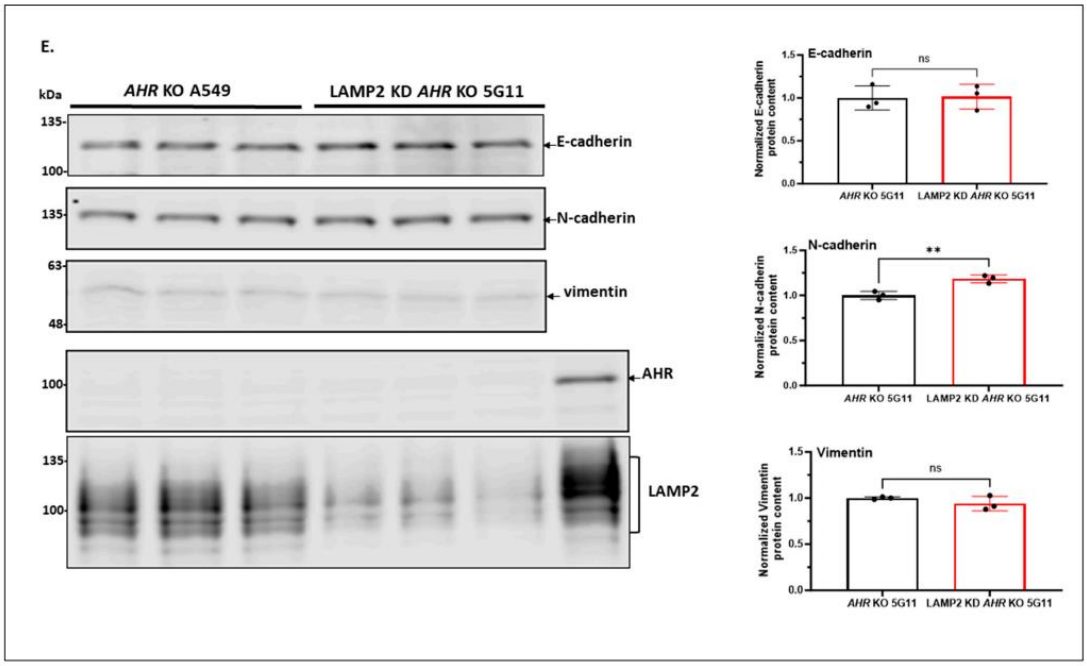
E.
AHR KO A549
LAMP2 KD AHR KO 5G11
kDa
135-
100-
E-cadherin
135-
N-cadherin
63-
48-
vimentin
100-
AHR
135-
100-
LAMP2
E-cadherin
ns
Normalized E-cadherin protein content
AHR KO 5G11
LAMP2 KD AHR KO 5G11
N-cadherin
**
Normalized N-cadherin protein content
Vimentin
ns
Normalized Vimentin protein content

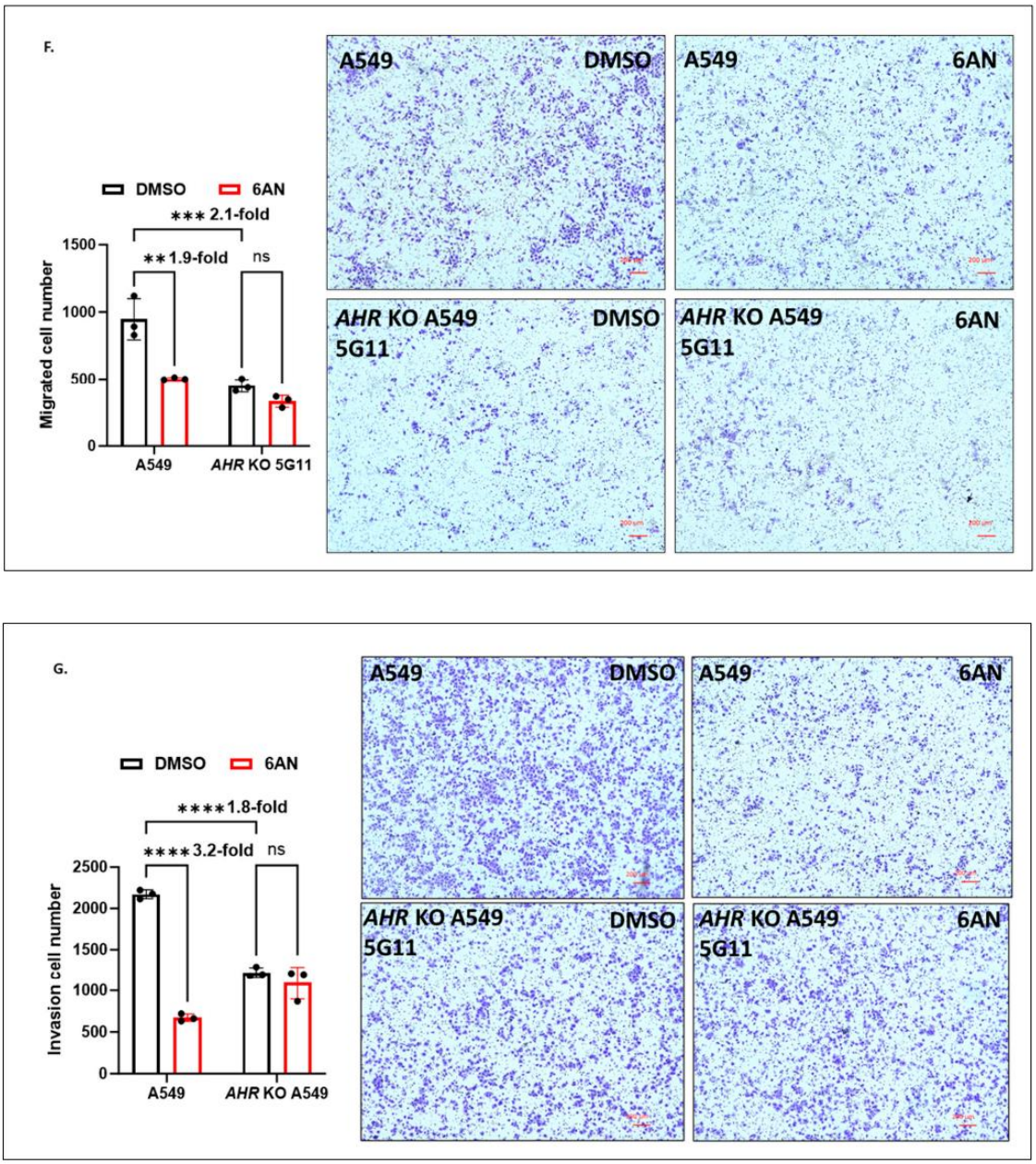

Note. (A) Wound healing assay results showing the migration capacities of the wild-type and *AHR* knockout (KO, 5G11) A549 cells. Both cell lines were treated with DMSO or 100 μM 6-AN for 48h. The microscopy images of wound closure were captured at 0 and 48h after wounding. The black lines represent the area lacking cells. Scale bars, 500 μm. The experiment was repeated two more times with similar results. Magnification: 4x.

(B) RT-qPCR results of the message levels of E-cadherin, N-cadherin, and vimentin in wild-type and *AHR* knockout (KO, 5G11) A549 cells. The plot represents the means with error bars (means ± SD, n = 3). The statistical significance of the differences between group means are evaluated by two-way ANOVA using Sidak test for multiple comparisons. Western blot results of E-cadherin, N-cadherin, and vimentin in (C) *AHR* knockout (KO, 5G11), (D) LAMP2 stable knockdown (LAMP2KD), and (E) LAMP2 stable knockdown (LAMP2 KD) of *AHR* knockout (KO) 5G11 A549 cells are shown as biological triplicates in one blot. Corresponding images in A549 wild-type cells are shown as the controls. 6-AN condition in C was performed with 100 μM 6-AN for 24h. (F) Transwell migration assay results of the wild-type and *AHR* knockout (KO, 5G11) A549 cells treated with DMSO or 6-AN for 24h. (G) Transwell invasion assay results of wild-type and *AHR* knockout (KO, 5G11) A549 cells treated with DMSO or 100 μM 6-AN for 24h. Representative images of migrated and invaded cells were captured. Scale bars, 200 μm. The number of migrated and invaded cells were quantitated by Image-J software. All plots (B-H) represent the means with error bars (means ± SD, n = 3) and were repeated once with similar results. The statistical significance of the differences between group means are evaluated by two-way (B, C, F, G) ANOVA using Tukey test for multiple comparisons. The statistical significance of the differences between group means are evaluated by unpaired t-test (D and E).

Fig. 2.8

A diagram of CMA-mediated degradation of AHR in A549 cells.

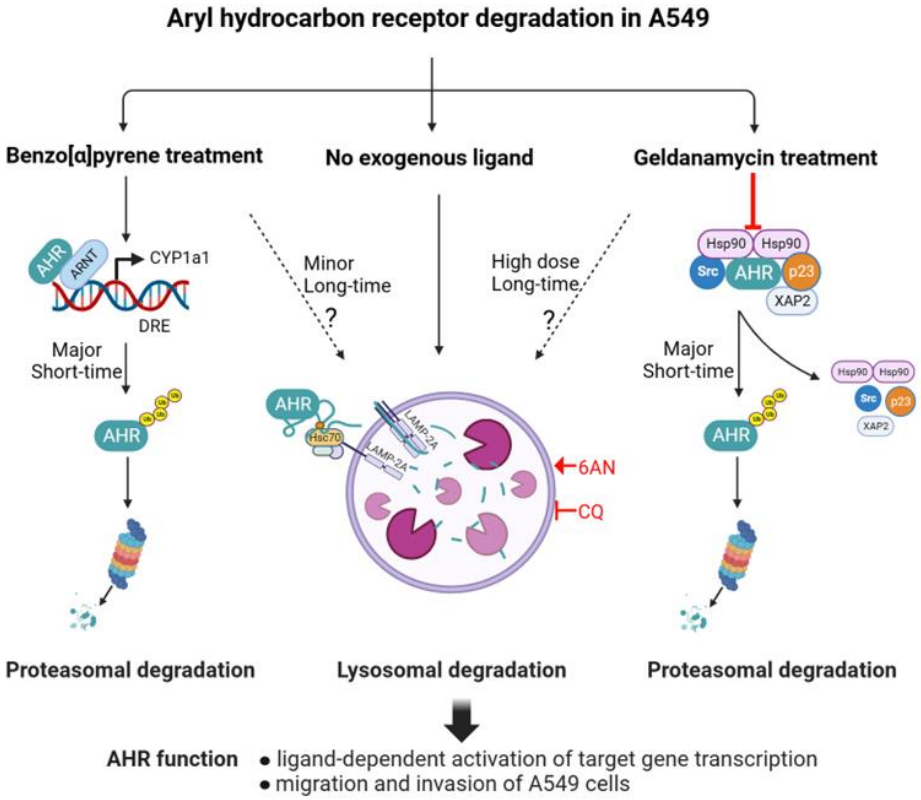

Discussion

Without exogenous ligand addition, AHR is subjected to autophagy in several human cell lines. Two autophagic mechanisms, namely selective macroautophagy and CMA, can selectively degrade client proteins such as human AHR. Here we provide evidence that AHR undergoes CMA regularly in A549 cells without the addition of any exogenous ligand (Fig. 2.8). This CMA-mediated AHR degradation can be activated by 6-AN in a dose- and time-dependent manner. Down-regulation of LAMP2A or mutation of the CMA motif of AHR abrogates this effect, strongly supporting the CMA mechanism in degrading AHR in A549 cells. Importantly, altering the degradation of AHR clearly

affects its activities in the ligand-activated gene transcription and modulation of the EMT of A549 cells. In the case of HeLa cells, downregulation of LC3 impairs the degradation of AHR, supporting that selective macroautophagy is responsible for the AHR protein degradation [69]. Interestingly, unlike A549 cells, treatment with 100 μM 6-AN for 24h does not change the AHR protein levels in HeLa cells [69], revealing that selective macroautophagy, but not CMA, degrades AHR in a different human cell-type. However, we also observed that AHR undergoes the LAMP2A-mediated degradation in the triple-negative MDA-MB-468 human breast cancer cells [75], revealing that AHR can undergo different autophagy mechanisms in a cell-specific manner. There is precedent in the literature that maintaining cellular protein levels via autophagy can be important. For example, CMA is responsible for the degradation of SMAD3 [90], Erk3 [91], Dicer [92], and oxidized PRL2 [93]. Analogous to human AHR, Tau and α-synuclein have been reported to undergo both selective macroautophagy and CMA [94-96]. Although AHR can be degraded via either CMA or selective macroautophagy in a cell-line specific manner, it is yet unclear how different human cells select which of the two autophagy mechanisms, or both, to degrade AHR.

Targeting autophagy dependent AHR degradation can potentially be an effective therapeutic approach. For example, activation of AHR in the gut can be beneficial for the treatment of inflammatory bowel disease [97]. Thus, AHR agonists might be effective for this treatment. Interestingly, P140, a 21mer phosphopeptide derived from U1-70K spliceosomal protein, suppresses CMA and is proposed to be a mechanism for the treatment of inflammatory bowel disease [98]. Suppression of CMA might increase the AHR protein levels in the gut and thereby elicit a synergistic effect of AHR activation

when used in combination with an AHR agonist – an interesting regimen for the treatment of inflammatory bowel disease.

CHIP, a cochaperone of HSC70, contains a U-box ring-finger motif found in ubiquitin ligases. This CHIP has been implicated to promote proteasomal degradation of CFTR [99], tau [100], and hypoxia inducible factor 1 alpha (HIF-1α) [101]. It is well known that binding of HSC70 to the CMA motif of proteins escorts proteins to LAMP2A at the lysosomal membrane, followed by internalization of proteins for degradation via CMA. Interestingly, HIF-1α also undergoes CMA and CHIP is required for the interaction of HSC70 and HIF-1α interaction [102]. Like HIF-1α, AHR has been shown to interact with CHIP in vitro [103]. It is conceivable that CHIP may be involved in the degradation of AHR via CMA.

Although it has been widely accepted that AHR ligands and GA cause degradation of AHR via the ubiquitin-proteasome pathway, it appears that autophagy might also be involved in determining the AHR levels after ligand or GA treatment in A549 cells (Fig. 2.8). Clearly, proteasomal degradation is primarily responsible for the degradation of AHR within 2 hours of ligand or low dose GA treatment in A549 cells. But in time, autophagy becomes active in degrading AHR in A549 cells, suggesting that degradation of AHR via autophagy may be temporarily interrupted soon after a low dose of GA treatment which activates proteasomal degradation of AHR. A high dose of GA (1 μM), however, promotes AHR degradation via autophagy in A549 cells.

Glutathione peroxidase 4 (GPX4) is known to be a CMA substrate. Inhibition of CMA increases the GPX4 protein levels, leading to inhibition of ferroptosis in mouse hippocampal HT-22 cells [104]. It has been reported that increased AHR protein levels

inhibit ferroptosis in human lung adenocarcinoma PC-9 cells by increasing the expression of SLC7A1, a molecule that suppresses ferroptosis by reducing the reactive oxygen species content [105]. Interestingly, AHR is also a CMA substrate and like GPX4, inhibition of the CMA-mediated degradation of AHR can be a viable approach for the regulation of ferroptosis.

Resveratrol has been reported to inhibit the ligand activated AHR transcriptional activity in a manner that is not acting as a typical AHR antagonist since no binding of resveratrol to AHR was observed [106]. Nevertheless, resveratrol inhibits AHR function. Interestingly, resveratrol also inhibits the transforming growth factor beta 1-mediated EMT by downregulating vimentin and upregulating E-cadherin in A549 cells [107]. This is the same outcome as observed in the ahr knockout A549 cells, suggesting that inhibition of the AHR function by resveratrol may be in part responsible for the EMT inhibition in A549 cells.

Although there is conflicting data in the literature showing the effect of AHR on the EMT in A549 cells, we clearly observed that AHR promotes the EMT in these cells via the CRISPR/Cas9 knockout approach. When the *AHR* gene is disrupted in A549 cells with no AHR protein production, E-cadherin is clearly upregulated whereas vimentin is also clearly downregulated, supporting the epithelial phenotype when AHR is absent. Wound healing, invasion, and migration experiments all unambiguously support the fact that AHR drives the EMT in A549 cells. Our finding is consistent with other researchers reporting that knocking down AHR in A549 cells suppresses invasion and migration potential [105]. Additionally, AHR drives non-small cell lung cancer tumorigenesis when the AHR protein is stabilized after deubiquitination by ubiquitin

carboxy-terminal hydrolase isozyme L3 [108], and this AHR action of cancer tumorigenesis may involve Jak2/STAT3 signaling [109].

When we attempted to modulate the AHR protein levels by either 6-AN or LAMP2 knockdown, we were unable to see any consistent trend of E-cadherin, vimentin, and N-cadherin expression which was AHR dependent. Naturally, we must keep in perspective the non-AHR dependent effects of 6-AN and LAMP2 knockdown on EMT marker expression. In the case of LAMP2 knockdown, mechanisms such as inhibition of the transcriptional activation of an EMT inducer that favors EMT and upregulation of some EMT inhibitor that favors the epithelial phenotype could be involved. Examining more than three markers of tumor invasion may be necessary in this case. For example, the levels of matrix metalloproteinase (MMPs), actin cytoskeleton proteins, and cell-extracellular matrix interaction molecules can be measured to possibly provide a better picture of how AHR drives EMT [110, 111].

Exploring how modulation of the AHR protein levels may alter the cancer stem cell-like properties and the associated gene expression can be insightful since overexpression of AHR has been implicated for an aggressive tumor phenotype in non-small cell lung cancer. [109]. Nevertheless, treatment with 6-AN clearly suppresses the invasion and migration of A549 cells in an AHR dependent manner. Although looking at the EMT marker levels alone fails to explain how reduction of the AHR levels (by 6-AN) favors the epithelial phenotype of A549 cells, modulation of the AHR protein levels can be a viable approach in controlling the AHR function.

Materials and Methods

Reagents and antibodies

CQ, BaP, GA, 6-AN, puromycin, CH223191, crystal violet, PMSF, and leupeptin were purchased from Sigma-Aldrich (St. Louis, MO, USA). (S)-MG132 and FICZ were purchased from Cayman Chemical (Ann Arbor, MI, USA). pLKO.1 Lentiviral LAMP2 shRNA plasmids and pLKO.1 Lentiviral ATG5 shRNA plasmids were purchased from Dharmacon (Lafayette, CO, USA). pGFP2-N2-AHR(NEKFF) and pGFP2-N2-mutant AHR(NAKAF) plasmids were previously generated by our lab [75]. pCMV-VSV-G was a gift from Bob Weinberg (Addgene plasmid # 8454; http://n2t.net/addgene:8454; RRID: Addgene_8454). pCMV-dR8.2 dvpr was a gift from Bob Weinberg (Addgene plasmid # 8455; http://n2t.net/addgene:8455; RRID: Addgene_8455). EndoFectin™ transfection reagent was purchased from GeneGopoeia (Rockville, MD, USA). TRI Reagent and Direct-zol RNA miniprep kit were purchased from Zymo Research (Irvine, CA, USA). MMLV high performance reverse transcriptase was purchased from Epicentre (Madison, WI, USA). iTaq SYBR green supermix was purchased from Bio-Rad (Hercules, CA, USA). Dynabeads™ Protein G was purchased from Invitrogen (Carlsbad, CA, USA). EnGen® Spy Cas9 NLS was purchased from NEB (Ipswich, MA, USA), multi-guide sgRNA was purchased from Synthego (Redwood, CA, USA), Lipofectamine RNAiMAX was purchased from Thermo Fisher Scientific (Waltham, MA, USA), QuickExtract DNA extraction solution was purchased from Lucigen (Middleton, WI, USA). PCR Master Mix was purchased from Promega (Madison, WI, USA), Falcon®24-well cell culture inserts with transparent PET membrane (8.0μm pore size) and Matrigel matrix were purchased from Corning Inc. (Corning, NY, USA). FBS (HyClone), DMEM (HyClone) and Opti-

MEM reduced serum medium were purchased from Thermo Fisher Scientific (Waltham, MA, USA). GlutaMAX-I and penicillin-streptomycin were purchased from Invitrogen (Carlsbad, CA, USA). Rabbit anti-AHR polyclonal antibody (SA210) was purchased from Enzo Life Sciences (Farmingdale, NY, USA). Mouse anti-LAMP2 monoclonal antibody (H4B4), mouse anti-Hsc70 monoclonal antibody (B-6), mouse anti-E-cadherin monoclonal antibody (G-10), mouse anti-Vimentin monoclonal antibody(V9), and mouse anti-N-cadherin monoclonal antibody (13A9) were purchased from Santa Cruz Biotechnology (Dallas, TX, USA). Rabbit anti-ATG5 polyclonal antibody (2630) was purchased from Cell Signaling Technology (Danvers, MA, USA). Donkey anti-rabbit and donkey anti-mouse secondary antibody conjugated with IRDye 680 or 800CW, RevertTM 700 Total Protein Stain and nitrocellulose membrane were purchased from LI-COR Bioscience (Lincoln, NE, USA).

Cell culture

A549 cells were a gift from Dr. John Livesey (University of the Pacific) and were authenticated by ATCC before being used for experiments in this paper. AD293 cells were purchased from Agilent Technologies (Santa Clara, CA, USA). Rat H4G1.1c3 stable cells carrying a DRE-driven GFP cDNA were a gift from Dr. Michael Denison (University of California, Davis). All the cell lines were cultured in DMEM supplemented with 10% fetal bovine serum (FBS), 1% penicillin-streptomycin and 1% GlutaMAX-I at 37 ℃, 5% CO2.

Preparation of whole cell extract and Western blot analysis

A549 cells were scraped in cold PBS and centrifuged at 400g for 5 min to collect cell pellets. The collected cells were washed once with cold PBS and then lysed in lysis

buffer (25mM HEPES pH7.4, 0.4 M KCl, 1mM EDTA, 1mM DTT, 10% glycerol, 1% NP40, 1mM PMSF, and 2μg/ml leupeptin). After 3 cycles of freeze and thaw, cell lysates were kept on ice for 30 min and then centrifuged at 16,000g for 15 min at 4 ℃. The supernatants were used as whole cell extracts. Total protein concentrations were measured by BCA assay. Proteins in 20μg of whole cell extract from each sample were separated by 12% SDS-PAGE and then transferred to nitrocellulose membranes via wet transfer method. Total protein staining was determined using LI-COR RevertTM 700 Total Protein Stain for normalization. Non-specific binding was blocked in blocking buffer (PBS, 0.1% Tween-20, 5% BSA) for 1h. The primary antibodies and their dilution are listed as follows: 1:2000 for anti-AHR (SA210); 1:1000 for anti-ATG5 (2630); 1:200 for anti-LAMP2 (H4B4); 1:200 for anti-Hsc70 (B-6); 1:200 for anti-E-cadherin (G-10); 1:200 for anti-Vimentin (V9); 1:200 for anti-N-cadherin (13A9). After washing with PBST (PBS and 0.1% Tween-20) 5 times, nitrocellulose membrane was incubated in 1:10,000 dilution of donkey secondary antibody conjugated with IRDye 680or 800 CW. Results were obtained and quantified by using LI-COR Odyssey CLx imaging system (Lincoln, NE, USA).

RNA extraction and reverse transcription-quantitative polymerase chain reaction (RT-qPCR)

Total RNA was extracted from A549 cells using TRI Reagent (Zymo Research) and RNA miniprep kit (Direct-zol) according to the manufacturer's recommendations. cDNA was reverse transcribed from 1μg of RNA by using MMLV high performance reverse transcriptase (Epicentre) into a final volume of 20 μl cDNA solution and 1 μl of it was used as the qPCR template. qPCR was performed with iTaq SYBR green supermix

(Bio-rad, USA) on a CFX Connect real-time PCR operating system (Bio-rad, USA) according to the following protocol: 95℃ for 2 min, 40 cycles of 95 ℃ for 15s and 60 ℃ for 1min. Relative gene expression was analyzed by the 2-ΔΔCq method [112] and 18s rRNA was used as an internal control for normalization. The primer sequences were as follows: 18s Forward: 5'-CGCCCCCTCGATGCTCTTAG-3' and Reverse: 5'-CGGCG-GGTCATGGGAATAAC-3'; cyp1a1 Forward: 5'-GGCCAC-ATCCGGGACA-TCACAGA-3' and Reverse: 5'-TGGGGATGGTGAAGGGGACGAA-3'; E-cadherin Forward: 5'-GCCT-CCTGAAAAGAGAGTGGAAG-3' and Reverse: 5'-TGG-CAGTGT-CTCTCCAAATCCG-3'; Vimentin Forward: 5'-TGTCCAAATCGATGTGGATG-TTTC-3' and Reverse: 5'-TTGTAC-CATTCTTCTGCCTCCTG-3'; N-cadherin Forward: 5'-ACAGTGGCCACCTACAAAGG-3' and Reverse: 5'-CCGAGATGGGGTTGATAATG-3'.

Generation of ATG5, LAMP2 stable knockdown A549 cells using lentivirus

Lentivirus containing ATG5 or LAMP2 shRNA was prepared as follows: AD293 cells (7×105) in 5ml of growth media (10% fetal bovine serum and 2mM GlutaMAX-I in DMEM) were seeded in a 25 cm2 flask. Cells were incubated at 37 ℃, 5% CO2 overnight. Then AD293 cells were transfected using 10μl EndoFectin™ transfection reagent with 5μg plasmids (2.5μg of pLKO.1 specific shRNA plasmid, 1.875μg of the pCMV-dR8.2 dvpr packaging plasmid, and 0.625μg of the pCMV-VSV-G envelope plasmid). Fresh complete medium was replaced 15h after transfection. After 24h, the medium containing lentiviral particles was transferred to a 15ml tube and stored at 4 ℃. Another 5ml of fresh complete medium was added to the cells and the medium containing lentiviral particles was harvested after 24h of incubation. The combined medium was centrifuged at 400g for 5min to pellet any AD293 cells and the supernatant

was used for infection. Stable ATG5 or LAMP2 knockdown cell lines were generated as follows: A549 cells were seeded in a 25 cm2 flask to achieve 50-70% confluent on the next day. Fresh complete medium containing 8μg/mL polybrene was replaced. 500μl of medium containing lentiviral particles was added into the flask. After 24h, the medium was replaced with fresh complete medium containing 1.5μg/ml of puromycin for stable cell line selection. Change to fresh medium containing puromycin every 2-3 days. ATG5 knockdown stable A549 cells were generated using pLKO.1 Lentiviral (TRC) ATG5 shRNA #5 (TRCN0000151963) plasmid; LAMP2 knockdown stable A549 cells were generated using pLKO.1 Lentiviral (TRC) LAMP2 shRNA #4 (TRCN0262) plasmid.

CRISPR/Cas9 mediated *AHR* knockout in A549 cells

Three different single guide RNA (sgRNA) targeting the exon 2 of the human *AHR* gene were used to knockout the *AHR* gene in A549 cells. The sequences were as follows, sgRNA1: 5'- GCTGAAGGAATCAAGTCAAA-3'; sgRNA2: 5'-ACAAGATGTTATTAATAAGT-3'; sgRNA3:5'- GAGAGCCAAGAGCTTCTTTG-3'. Cas9 nuclease NLS and sgRNAs were introduced as ribonucleoprotein (RNP) complex into A549 cells through transfection using the Lipofectamine RNAiMAX according to the manufacturer's recommendations. In brief, 3μM Cas9 nuclease NLS was combined with 3μM sgRNAs (1μM each of 3 sgRNAs) to form RNPs in 12.5μl volume with the Opti-MEM. Gently mixed the reaction and incubated at room temperature for 10min. 1.2μl of transfection reagent RNAiMAX was diluted in 12.5μl of the Opti-MEM and was added directly into the RNPs tube. The RNPs/liposome complexes were mixed gently and incubated at room temperature for 20min. Meanwhile, 3.2×105 cells/ml A549 cell suspension were prepared and 125μl of them were added into each well of a 96-well

plate, followed by mix with 25μl of RNPs/liposome complexes. The transfected cells were incubated at 37 ℃, 5% CO2 for 72h. Then the isolation of single cells from the knockout cell pool was accomplished through limiting dilution according to protocol from Synthego. 0.5-1 cell/100μl of the diluted cell suspension was seeded into each well of a 96-well plate. To genotype clones, genomic DNA was isolated using QuickExtract DNA extraction solution (Lucigen). PCR was performed to amplify the edited region using PCR Master Mix (Promega) with the following primers: OL921 Forward 5'-TCGGAAGAATTTAACC-CATTCCCT-3' and OL922 Reverse 5'-TGCAGCCACTGAAATGATGC-3'. The DNA fragment ~500bp was observed by agarose gel electrophoresis and was purified for Sanger sequencing (Functional Biosciences, WI, USA). The sequencing data was uploaded to online Inference of CRISPR Edits (ICE) analysis tool (http://ice.synthego.com) for knockout analysis.

Transient transfection

A549 cells were seeded in a 6-well plate at 90-95% confluency at the time of transfection. Plasmid DNA, EndoFectin™ transfection reagent, and Opti-MEM were equilibrated to room temperature before use. Cells were transfected with 4μg of plasmid and 8μl of transfection reagent. Both plasmids and transfection reagent were diluted in the Opti-MEM, respectively. Then the diluted transfection reagent and the diluted DNA were combined and kept at room temperature for 20min to allow DNA-transfection reagent complexes to form. The combined complexes were added to each well and mixed gently. The cells were harvested for analysis after 48h of incubation at 37 ℃, 5% CO2.

Co-immunoprecipitation

A549 cells were cultured in a 75 cm2 flask and reached 90-95% confluency at the time of experiment. Cells were treated with or without CQ for 6h and then were harvested to be lysed in lysis buffer (25mM HEPES pH7.4, 0.15 M KCl, 1mM EDTA, 1mM DTT, 10% glycerol, 10mM N-Ethylmaleimide, 1mM PMSF, and 2μg/ml leupeptin). About 2mg of the whole cell extract were incubated with rabbit anti-AHR antibody (SA210) for 30min at room temperature. Then the samples were added to the pre-equilibrated Dynabeads™ Protein G (Invitrogen) and q.s. to 1ml with IP buffer (25mM HEPES pH7.4, 1mM EDTA, 1mM DTT, 10% glycerol, 150mM NaCl, 0.05% Tween-20, and 1mg/mL BSA). The samples were rotated at 60rpm in the cold room for 16-18h. The magnetic beads-Ab-Ag complex were washed 3 times with cold IP buffer on the magnet. Resuspend the magnetic beads-Ab-Ag complex in 30μl of electrophoresis sample buffer and boiled at 95 ℃ for 3min to free the bound protein. 1% of the whole cell extract was used as an input control. All the samples were analyzed by western blot with antibodies against AHR, LAMP2, and Hsc70.

Ligand dependent, DRE-driven expression of GFP in H4G1.1c3 cells

H4G1.1c3 cells (3 x 105) were seeded into each well of a 24-well plate. After incubation at 37 ℃ and 5% CO2 for 24h, the cells reached 70-85% confluence. 1 ml of fresh complete medium was exchanged for each well. The cells were then treated with DMSO (0.2%), 6-AN (100 μM), MG132 (10 μM), GA (100 nM), BaP (5 μM), FICZ (1 μM), CH223191 (10 μM), BaP plus CH223191, and FICZ plus CH223191, respectively, and incubated for at 37 ℃ and 5% CO2 for 12h. Fresh complete medium was exchanged

after treatment. Fluorescence images were acquired by a Keyence BZ-X700 fluorescence microscope in 4x objective.

Wound healing assay

A549 cells were seeded in 6-well plates and formed monolayers at the time of wounding. A sterile 1ml pipette tip was used to scratch across the monolayers to form a linear wound. Then the disassociated cells and debris were removed by washing with PBS. Cells were treated with DMSO or 6-AN for 48h. Representative images were taken at 0 and 48h after the treatments at the same position under an inverted microscope (BZ-X700, KEYENCE, USA) with camera. The scale bar on the representative images is 500μm.

Transwell migration and invasion assay

Falcon® 24-well cell culture inserts with transparent PET membrane (8.0μm pore size) and Corning Matrigel matrix (1:5 dilution) were used to determine the cell migration and invasion capability. For migration assay, 5×104 cells were seeded into the upper chamber and 700μl of complete DMEM medium was added in the lower chamber placed in 24-well plates. For invasion assay, 1×105 cells were seeded into the upper chamber which was coated with Matrigel before use. After 24h incubation, the cells on the inserts were fixed with methanol for 10min and stained with 0.1% crystal violet for 5min. Then the cells on the top side of the membrane were removed with cotton swabs carefully. Only the cells that migrated or invaded through the membrane to the bottom of inserts were imaged by using an inverted microscope (BZ-X700, KEYENCE, USA) with camera. Three fields, which cover about 80% of the well, were randomly captured and analyzed by Image-J software.

Statistical analysis

GraphPad Prism 9 software (La Jolla, CA) was used for statistical analysis. The statistical significance of the differences between group means are evaluated by one-way or two-way ANOVA using Tukey or Sidak test for multiple comparisons. Statistical significance is indicated as follows: *$p < 0.05$, **$p < 0.01$, ***$p < 0.001$, ****$p < 0.0001$, and $p > 0.05$ (ns, not significant). The two-tailed unpaired t-test was used to determine the statistical significance in Fig. 2.7D and 2.7E.

CHAPTER 3: MECHANISMS OF P23 KNOCKDOWN MEDIATED AHR DEGRADATION IN A549 CELLS AND HALOTAG-AHR OVEREXPRESSION

Introduction

PTGES3/p23 was first discovered as a co-chaperone protein of Hsp90. The stabilization of the closed conformation of Hsp90 and inhibition of its ATPase activity are required for the client protein maturation, which is involved in numerous biological processes and tumorigenesis. Six years following its initial discovery, p23 underwent characterization as PTGES3, a prostaglandin E2 (PGE2) synthetase that promotes tumor growth via multiple mechanisms. The progression of cancer is influenced by the production of PGE2 through the COX/prostaglandin (COX/PG) pathway. Thus, p23 is recommended to be regarded as a plausible biomarker and target for therapy [113].

p23 is a 160 amino acids protein encoded by the *PTGES3* gene and it can be divided into two distinct domains, namely an amino-terminal region that binds to Hsp90 and an unstructured carboxyl-terminal region [114]. p23, the smallest component of the HSP90 chaperone machinery, is primarily recognized for its ability to bind to the ATP-bound form of HSP90. This binding event effectively hinders the intrinsic hydrolytic activity of HSP90 and promotes the stabilization of various HSP90-substrate complexes, including Fes tyrosine kinase, transcription factors like AHR, telomerase, and the reverse transcriptase enzyme. The prenatal or perinatal lethality observed in a p23 knockout mouse model further emphasizes the significance of p23 in cellular function and development. Although p23 has been found to possess prostaglandin E2 synthase activity, the exact significance of this activity remains unclear as p23 knockout mice do not show any impairment in prostaglandin enzymatic activity [115]. Despite its well-

known as an Hsp90 cochaperone, recent studies indicated that p23 may also possess certain functions independent of Hsp90. Some groups reported that p23 can still exert its functions on substrate proteins that have been released from Hsp90 complexes. Additionally, p23 has been observed to possess a passive, ATP-independent chaperoning activity in its carboxyl terminus that enabled p23 to prevent the aggregation of denatured proteins. Reebye et al. reported that the interaction between p23 and androgen receptor (AR) exhibits some degree of Hsp90 independence, and the transcriptional activity of AR is significantly increased by a mutant form of p23 that is incapable of binding to Hsp90, the extent is similar to the effect observed with wild type p23 [116]. Our lab has shown that p23 protects the human aryl hydrocarbon receptor from degradation via a heat shock protein 90-independent mechanism [117].

Lung cancer is a prevalent malignancy that has a significant incidence and mortality rate globally. Approximately 40% of all lung tumors are accounted for by lung adenocarcinoma (LUAD), which is a subtype of non-small cell lung cancer (NSCLC). Despite the significant contribution of conventional therapeutic approaches like surgical excision, radiotherapy, and chemotherapy in the last few decades, the overall survival (OS) rate of LUAD remains below 20% even after five years. It is due to the gradual advancement of LUAD, resulting in nonspecific symptoms during the early stages of the disease. Consequently, most patients are diagnosed at an advanced stage, which unfortunately leads to a poor prognosis [118]. Recently, the field of medicine has transitioned into the era of precision medicine and targeted therapy which has immense promise in the identification and prediction of diverse cancer types. Therefore, identifying novel biomarkers of LUAD is becoming more important and urgent in

enhancing the treatment and clinical outcomes for patients with LUAD. There has been an increase in studies investigating the expression of p23 in various types of cancer. Inês Cebola et al. reported that p23 is overexpressed in tumor tissues compared to the adjacent mucosa in colorectal cancer [119]. p23 mRNA expression was found to be elevated in NSCLCs compared to normal lung tissues. Nevertheless, there is a scarcity of research investigating the molecular mechanism and clinical implications of p23 in NSCLC [120]. In addition, Jinyun Chen discovered that downregulation of p23 prevented normal human epithelial cells from the AHR-mediated toxicities in the presence of benzo[a]pyrene or cigarette smoke condensate, suggesting that p23 plays an important role as a part of AHR cytoplasmic complex [1].

Our lab is dedicated to studying the AHR degradation in several different cell lines. Previous data suggested that downregulation of p23 in immortalized cancer cell lines (mouse hepatoma Hepa1c1c7, human hepatoma Hep3B, human cervical HeLa) and untransformed human lung bronchial/tracheal epithelial (HBTE) cell lines promoted the AHR degradation in the absence of AHR ligand [1] [69] [121]. Additionally, Yujie Yang et al. demonstrated that the degradation of AHR was increased by p23 knockdown in HeLa cells through an autophagy-lysosome pathway [69]. Thus, my research was to find out how AHR was degraded in p23 knockdown A549 cells, which is a commonly studied LUAD epithelial cell line.

In this chapter, my previous data suggested that p23 knockdown in A549 cells decreased AHR protein levels due to upregulated protein degradation and downregulated *AHR* transcript levels. Our hypothesis was that the degradation of AHR through p23 knockdown may be facilitated by a macroautophagy-lysosome pathway in

A549 cells. However, my following data showed that CQ treatment reversed AHR protein levels in both A549-WT and A549-p23KD cells to a similar extent. Furthermore, autophagic flux and AHR-LC3B interaction were not upregulated in p23KD-A549 cells compared to WT-A549 cells, suggesting that p23 knockdown induced AHR protein degradation was not due to the activation of macroautophagy in A549 cells. Meanwhile, it was not caused by proteasome degradation since proteasomal inhibitor MG132 failed to reverse AHR protein levels in p23KD-A549 cells. Directly analyzing HeLa-scramble cells and HeLa-p23KD cells constructed before failed to explain the discrepancy between HeLa-p23KD and A549-p23KD cells. Thus, complete knockout of p23 in HeLa cells by CRISPR/Cas9 technology could further clarify the underlying mechanisms.

Moreover, overexpression of HaloTag-AHR for HaloTag magnetic beads purification was intended to analyze amino acid sequence and post-translational modification of AHR via liquid chromatography with tandem mass spectrometry (LC-MS/MS). HaloTag-AHR was overexpressed in HeLa-WT, HeLa-AHRKO, A549-WT and A549-AHRKO cell lines by transient transfection of pHTC-HaloTag-AHR plasmids. HaloTag-AHR protein levels were extremely higher in HeLa-WT cells when compared to other transfected cell lines. However, after G418 selection, HaloTag-AHR was only overexpressed in the A549-AHRKO 5G11 cells but with a significantly lower content compared to the endogenous AHR protein levels in A549-WT. The exogenous HaloTag-AHR protein degradation could be blocked by CQ treatment as well.

Lastly, we are curious about whether mouse AHR could be degraded via autophagy-lysosome pathway. Since our previous data from Hepa1c1c7 cells with *AHR*^{b} allele showed that CQ could not increase AHR protein levels. Moreover,

sequencing analysis showed a higher similarity between *hAHR* and *AHR^d* allele. Thus, we hypothesized that mouse AHR with *AHR^d* allele could be degraded via lysosome, like the degradation of hAHR protein. However, KLN205 cell line from the lung of a DBA/2 mouse with squamous cell carcinoma did not express the *AHR^d* allele protein which showed no 104kDa (848aa) protein band. Instead, a 95kDa protein band usually representing mouse *AHR^b* allele protein was observed in KLN205 cells. More research will be needed to elucidate this observation in the future.

Results

Autophagy inhibitor blocked the basal AHR degradation with or without p23 stable knockdown in A549 cells

Our lab previously observed that downregulation of p23 in immortalized cancer cell lines (mouse hepatoma Hepa1c1c7, human hepatoma Hep3B, human cervical HeLa) and untransformed human lung bronchial/tracheal epithelial (HBTE) cell lines promoted the AHR degradation in the absence of AHR ligand [1][117] [121]. In this study, the p23 protein was stably knocked down in A549 cells using lentivirus-mediated shRNA technology. The p23 protein was knocked down to 40% compared to that of wild-type A549 cells (Fig. 3.1A). The AHR protein level in p23 stable knockdown A549 cells was about 50% when compared to that of wild type A549 cells (Fig. 3.1B), suggesting that knockdown of p23 decreased the AHR protein levels in A549 cells. Furthermore, we examined whether this p23 knockdown caused AHR degradation was mediated by autophagy-lysosomal pathway in A549 cells. Yujie Yang previously observed that the degradation of AHR in HeLa cells was increased by p23 knockdown via autophagy-lysosome pathway. The AHR protein levels in p23 stable knockdown

HeLa cells became even higher than the levels in wild-type HeLa cells after CQ treatment, suggesting that CQ reversed p23-mediated AHR degradation [69]. However, my data suggested that basal AHR protein degradation in A549 cells was reversed by CQ treatment with a p23-independent mechanism. Lysosomal inhibitor CQ increased the AHR protein levels by 1.5-fold with or without p23 knockdown, which is different from the results of HeLa cells [69].

Fig. 3.1

The AHR protein levels were elevated in both A549-WT and A549-p23KD cells upon inhibition of lysosomal degradation.

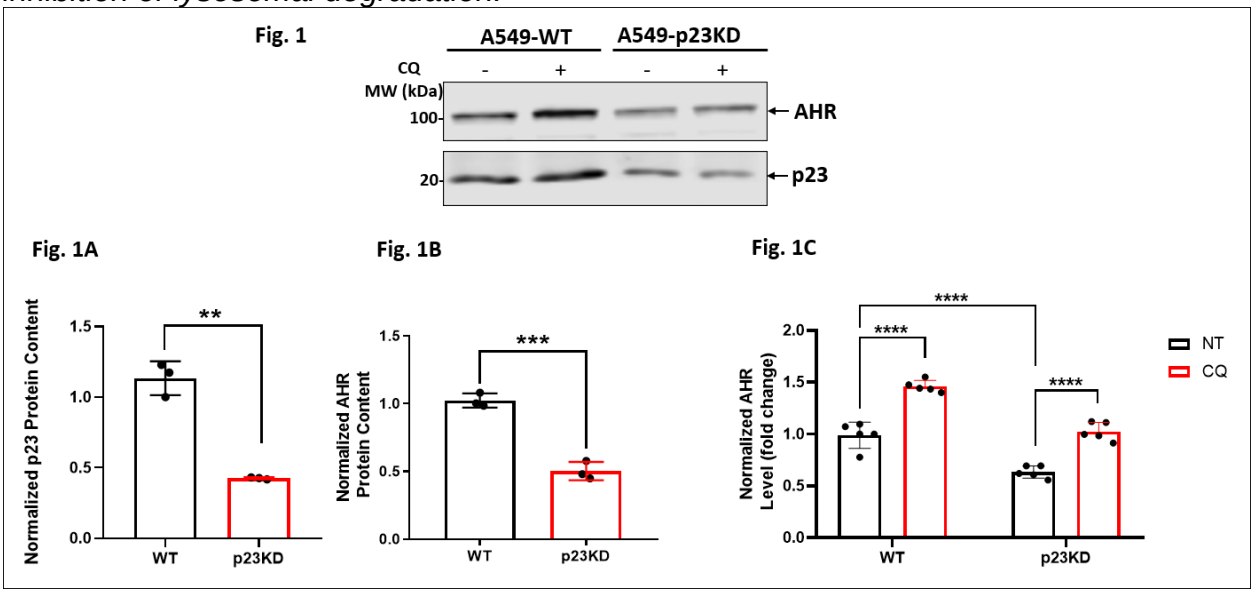

Note. Western blot results of A549-WT and A549-p23KD cells treated with 60μM CQ for 6h. The images are representatives of the plotted data. (A) Western blot results of p23 protein levels in A549-WT and A549-p23KD cells. The plots are the means with error bars (means ± SD, n = 3). (B) Western blot results of AHR protein levels in A549-WT and A549-p23KD cells. The plots are the means with error bars (means ± SD, n = 3). (C) Western blot results of A549-WT and A549-p23KD cells treated with 60μM CQ for 6h.

The plots are the means with error bars (means ± SD, n = 5). The statistical significance of the differences between group means was evaluated by unpaired *t*-test (A, B) and two-way ANOVA using Tukey's test for multiple comparisons (C). Statistical significance was indicated as follows: ** $p < 0.01$, *** $p < 0.001$, and **** $p < 0.0001$.

p23KD A549 cells expressed less *AHR* mRNA

Next, we examined whether the *AHR* mRNA level was changed in p23KD A549 cells. Real-time qPCR results showed that the AHR message RNA level was decreased by about 55% of the wild-type A549 cells (Fig. 3.2A), which is consistent with our lab's previous data in Hepa1c1c7 cells [121]. Additionally, we investigated the potential effect of *AHR* message RNA stability on the *AHR* message RNA levels in p23KD A549 cells. Actinomycin D was used to inhibit general transcription, and A549 cells were collected at 0, 3, and 6 h of actinomycin D treatment to determine the *AHR* mRNA levels. We observed that the *AHR* mRNA was degraded at a similar rate in both WT and p23KD A549 cells, suggesting that the reduced *AHR* mRNA levels in p23KD A549 cells could not be caused by an increased mRNA degradation (Fig. 3.2B).

Fig. 3.2

Effect of p23 knockdown on AHR transcription level and AHR message RNA stability.

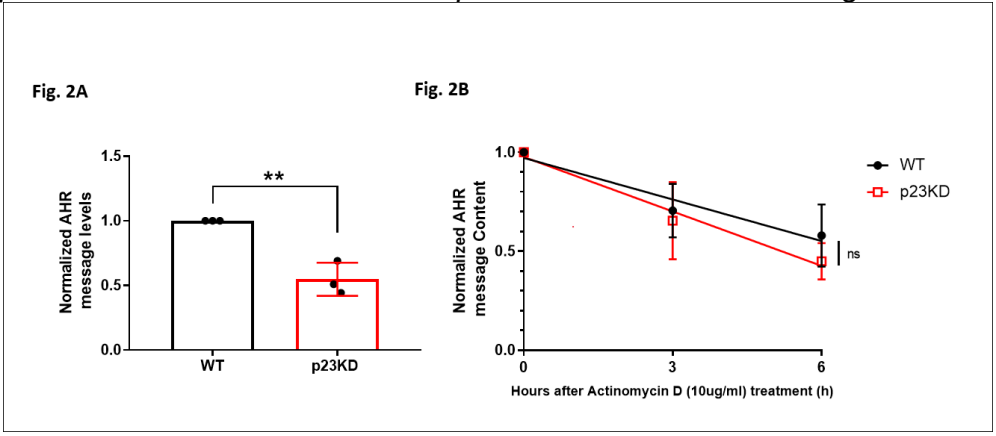

Note. (A) RT-qPCR results of *AHR* message RNA levels in WT and p23KD A549 cells. (B) RT-qPCR results of *AHR* message RNA levels after 10 μg/ml of actinomycin-D treatment for 0-6h. 18s mRNA was used for normalization. All plots are the means with error bars (means ± SD, n = 5). The statistical significance of the differences between group means was evaluated by unpaired *t*-test. Statistical significance is indicated as follows: ** $p < 0.01$, and $p > 0.05$ (ns, not significant).

The protein degradation rate of AHR was elevated in p23KD A549 cells

We examined whether the AHR degradation rate could play a role in the reduced AHR protein levels in p23KD A549 cells. Cycloheximide was used to inhibit protein synthesis. We observed that the AHR protein levels of wild-type A549 cells reduced to about 80%, while the AHR protein levels of p23KD A549 cells reduced to about 60% (Fig. 3.3). Thus, the protein degradation rate of AHR was significantly higher in p23KD cells than in WT cells, suggesting that AHR degradation could be involved in the reduced AHR protein levels in p23KD-A549 cells.

Fig. 3.3

p23 knockdown increased AHR protein degradation rate in A549 cells.

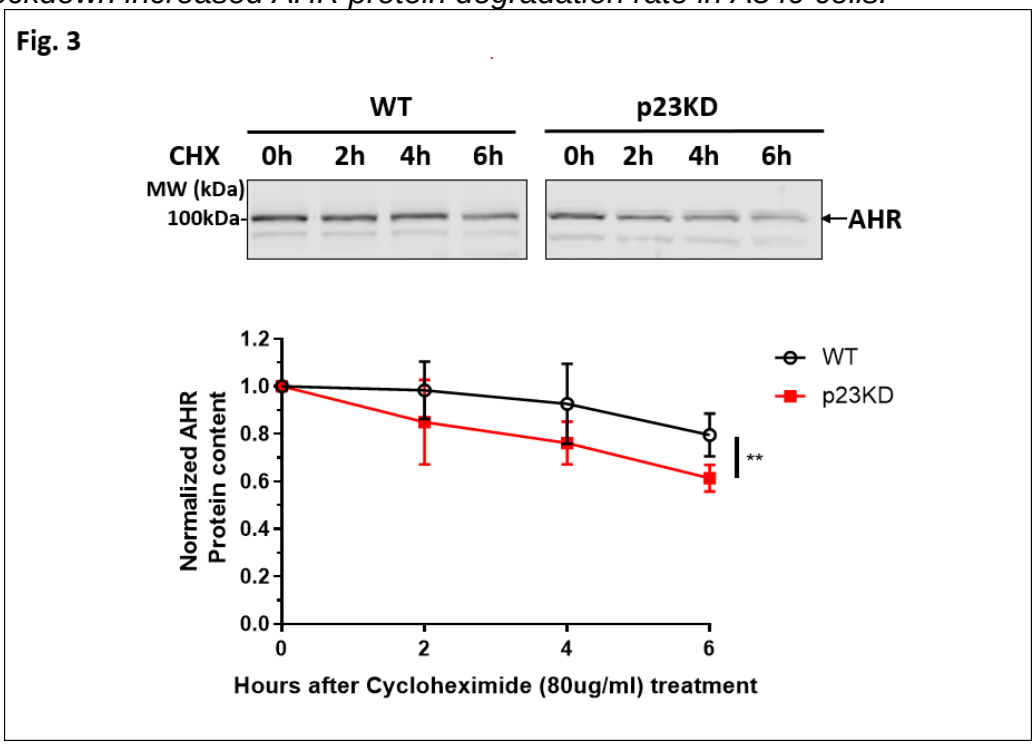

Note. Western blot results of A549-WT and A549-p23K cells treated with 80 μg/ml cycloheximide (CHX) for 0, 2, 4, 6 h. The images are representatives of the plotted data. All plots are the means with error bars (means ± SD, n = 5). The statistical significance of the differences between group means was evaluated by unpaired *t*-test. Statistical significance is indicated as follows: ** $p < 0.01$.

Proteasome inhibitor MG132 reduced AHR protein levels in both A549-WT and A549-p23KD cells

Next, we examined whether MG132 could reverse the reduction of AHR in p23KD cells. Intriguingly, we observed that in p23KD cells, MG132 not only failed to reverse the reduction of AHR but also further suppressed the levels of AHR protein (Fig. 3.4B). And this suppression of AHR protein content is similar between WT and p23KD

cells (Fig. 3.4A and 3.4B), which is different from the results of HeLa cells. In addition, the reduction caused by MG132 could be partially reversed by lysosomal inhibitor CQ, which can be explained by several papers that MG132 boosted autophagic degradation [122].

Fig. 3.4

Proteasome inhibitor MG132 decreased AHR protein levels in both A549-WT and A549-p23KD cells.

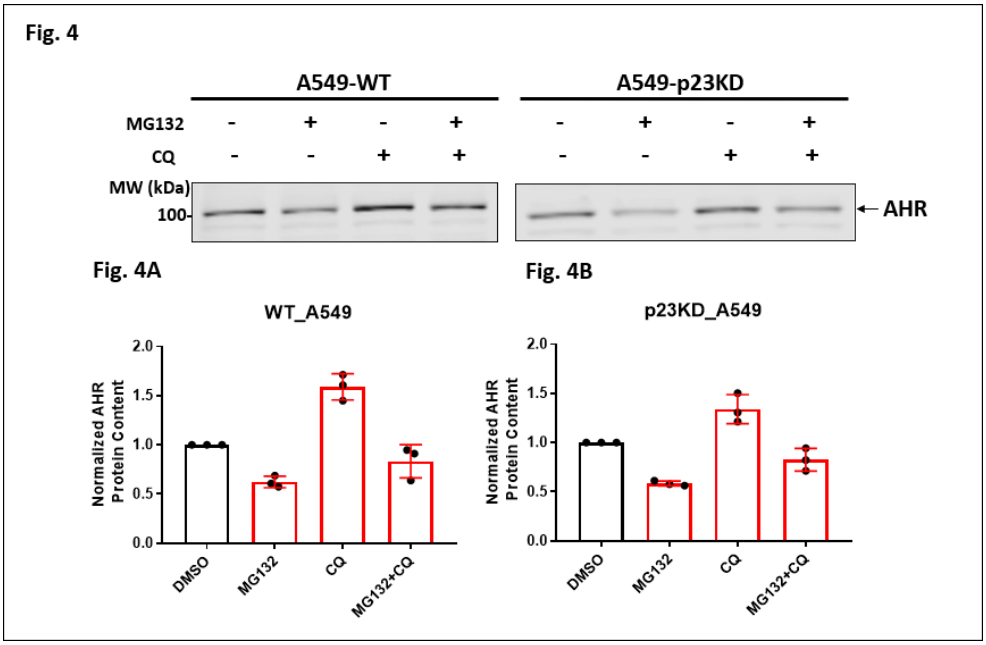

Note. Western blot results of A549-WT (A) and A549-p23KD (B) cells treated with DMSO, 10 μM MG132, 60 μM CQ, or 10 μM MG132 plus 60μM CQ for 6h. The images are representatives of the plotted data. All plots are the means with error bars (means ± SD, n=3). Total protein stain was used for Western normalization.

The autophagic flux was similar between A549-WT and A549-p23KD cells

We previously observed that p23 knockdown in HeLa cells exhibited higher autophagic flux, resulting in accelerated AHR protein degradation. LC3B-II is an autophagic marker since it is bound to the membranes of the autophagosome tightly. Thus, it reflects the number of autophagosomes. The progression of autophagy can be assessed by monitoring the conversion of LC3 from LC3B-I to LC3B-II and the subsequent lysosomal degradation of LC3B-II [123]. LC3B antibodies tend to have greater affinity for LC3B-II than LC3B-I. Thus, the use of LC3B-I as a denominator for quantifying LC3B-II (LC3B-II/LC3B-I) is unreliable [124]. Here, we compared the amount of LC3B-II with the total protein stain for quantification. Autophagic flux was determined by analyzing the rate of LC3B-II levels over time in the presence of CQ. Our results showed that the knockdown of p23 failed to change autophagic flux in A549 cells, which is different from the results of HeLa cells (Fig. 3.5).

Fig. 3.5

Autophagic flux remained unchanged in p23 knockdown A549 cells.

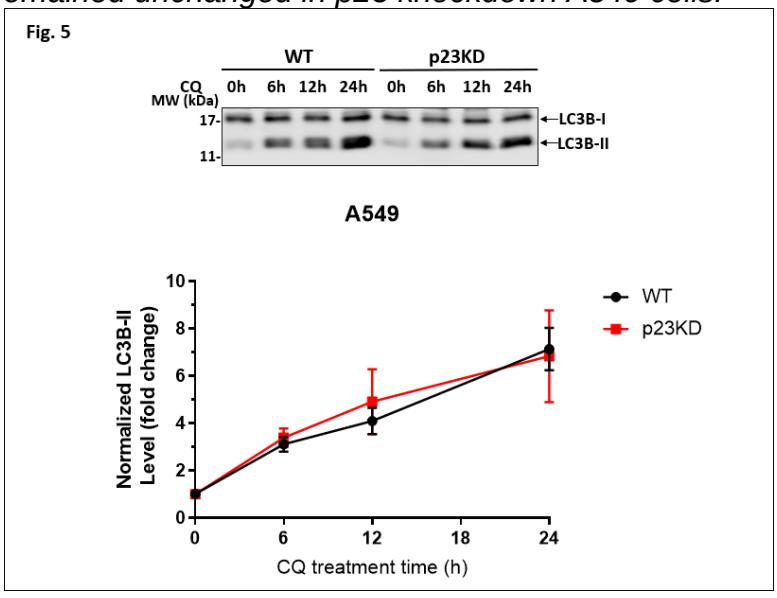

Note. Western blot results of A549-WT and A549-p23KD cells treated with 60μM CQ for 0, 6, 12, 18, or 24h. The images are representatives of the plotted data. All plots are the means with error bars (means ± SD, n = 5). Total protein stain was used for Western normalization.

The proximity ligation assay showed that AHR interacted with LC3B in both A549-WT and A549-p23KD cells

To determine the physical interaction of AHR and LC3B in A549 cells, the proximity ligation assay was executed. In both wild type and p23 knockdown A549 cells, the interaction between AHR and LC3B was observed in the presence of CQ since LC3B-II was accumulated by lysosomal inhibition (Fig. 3.6). However, there was not obviously higher AHR-LC3B interaction in p23KD A549 cells when compared to WT A549 cells. In addition, there is still little PLA signal in the negative control (NC) cells even though no primary antibodies were added against the interaction partners. Additional comprehensive PLA analysis is required to draw a definitive conclusion.

Fig. 3.6

The proximity ligation assay showed that AHR interacted with LC3B in both A549-WT and A549-p23KD cells to a similar extent.

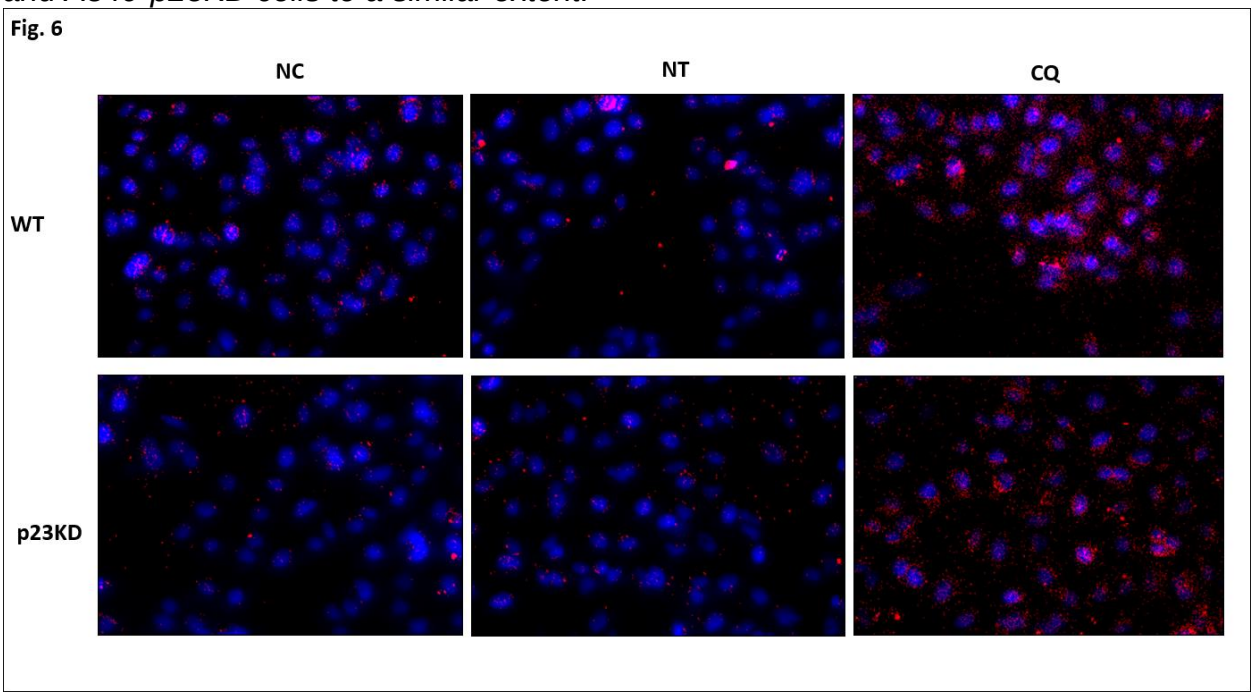

Note. Duolink® Proximity Ligation Assays (PLA) was used to detect the interaction between LC3B and AHR. Negative control (NC) represented cells incubated without primary antibodies; No treatment (NT) and 60μM CQ treatment cells were processed according to the manufacturer's recommendations. PLA signals were shown in red and the nuclei in blue.

3-methyladenine failed to inhibit AHR protein degradation in both A549-WT and A549-LAMP2KD cells.

3-methyladenine (3MA) inhibits autophagy by blocking autophagosome formation via the inhibition of class III phosphatidylinositol 3-kinases (PI3K) complex formation. PI3K plays an important role in activating mTOR, a key regulator of macroautophagy [125]. AHR protein levels were not increased after 8h of 5mM 3MA treatment in both

wild type and LAMP2KD A549 cells, suggesting that macroautophagy could not contribute to basal AHR degradation (Fig. 3.7). But we cannot rule out the possibility that a higher concentration of 3MA or prolonged incubation could further block AHR degradation via macroautophagy.

Fig. 3.7

A549-WT and A549-LAMP2KD cells did not exhibit an increase in AHR protein levels upon treatment with 3-methyladenine (3MA).

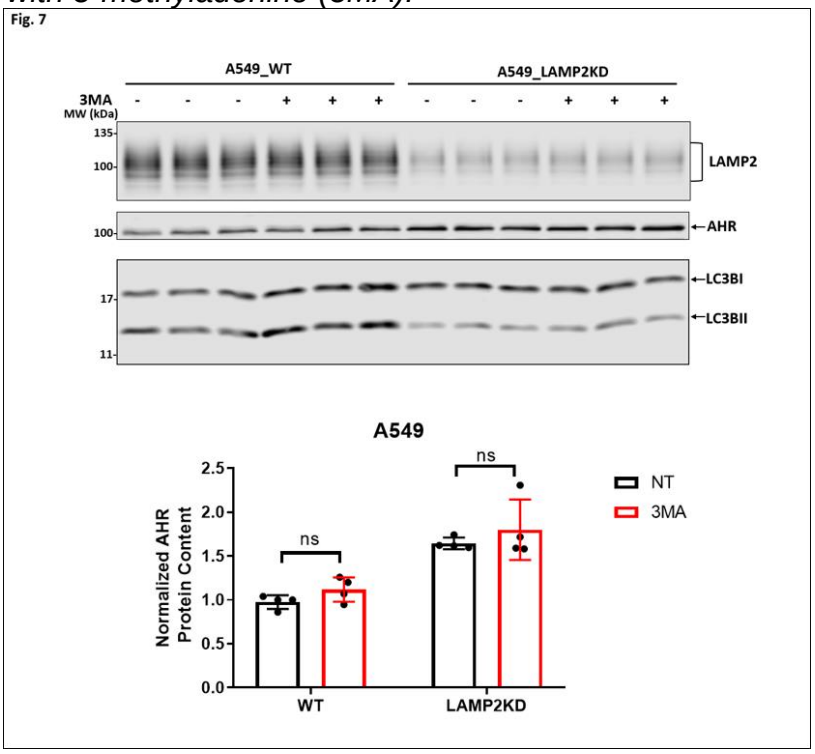

Note. Western blot results of A549-WT and A549-LAMP2KD cells treated with or without 5mM 3MA for 8h. The images are biological triplicates from one experiment, and the experiment was repeated once with a similar result. The statistical significance was evaluated by two-way ANOVA using Tukey's test for multiple comparisons. Statistical significance is indicated as follows: $p > 0.05$ (ns, not significant).

A comparison between the knockdown of p23 in A549 and HeLa cells

To find out the difference between HeLa-p23KD and A549-p23KD cells directly, we thawed the HeLa-scramble cells and HeLa-p23KD cells which were constructed by Yujie Yang. After 3 passages of culture with puromycin selection, CQ treatment was conducted in HeLa-scramble and HeLa-p23KD cells. HeLa-scramble cells stably expressed scrambled siRNA that should not lead to the degradation of any genes. We observed that the downregulation of p23 by 48% only decreased the AHR protein levels to 86% when compared with the HeLa-scramble shRNA negative control group (Fig. 3.8A and 3.8B), which was very different from Yujie's results that the cellular AHR protein levels in p23 stable knockdown HeLa cells were about 54% when compared to that of wild type HeLa cells. This could be explained by other regulatory mechanisms that are involved in the compensatory upregulating AHR protein levels of p23KD-HeLa cells. In addition, we observed a slight increase of p23 protein levels from passage 6 to passage 10 of HeLa-p23KD cells (Fig. 3.8), suggesting that the HeLa cells unstably expressed p23 specific siRNA. Furthermore, CQ treatment increased AHR protein levels by 1.7-fold in both HeLa-scramble and HeLa-p23KD cells (Fig. 3.8C), which was different from Yujie's data that the AHR protein levels in p23 stable knockdown HeLa cells became even higher than the levels in wild type HeLa cells after CQ treatment. To visualize the difference between HeLa cells and A549 cells simultaneously, samples from HeLa-scramble, HeLa-p23KD, A549-scramble, and A549-p23KD cells with or without CQ treatment were conducted in the same Western blot analysis. However, it showed a similar result as before. We should construct new HeLa-p23KD stable cell lines or use transient transfection to knock down p23 in HeLa cells directly.

Fig. 3.8

A comparison between the knockdown of p23 in A549 and HeLa cells.

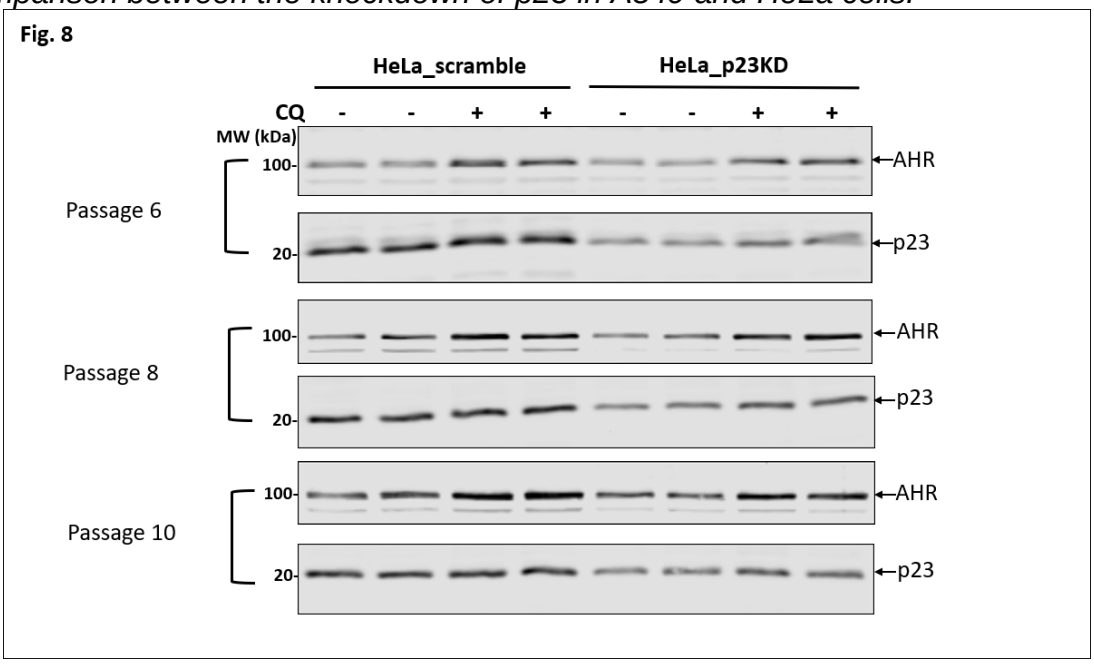

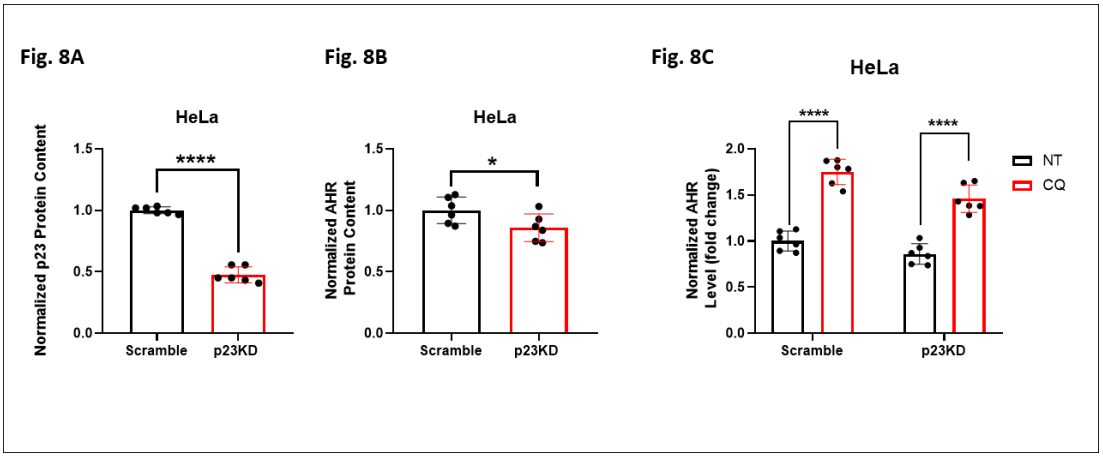

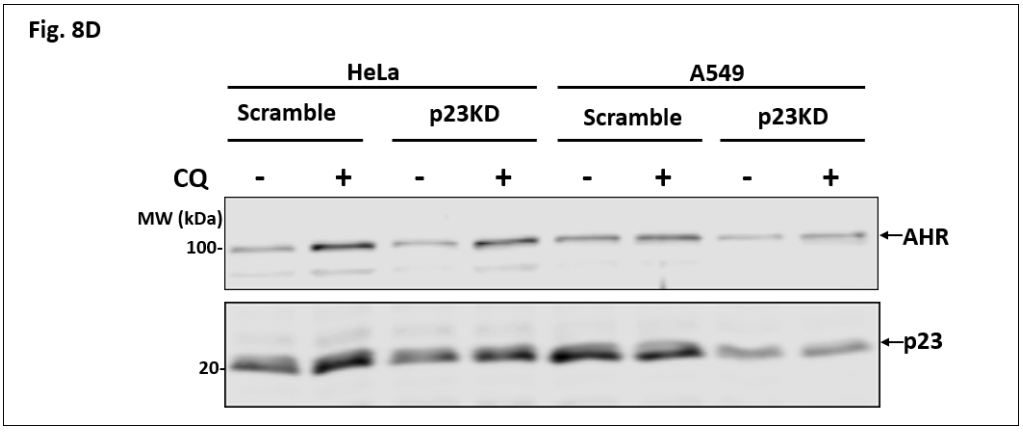

Note. Western blot results of HeLa-scramble and HeLa-p23KD cells treated with or without 40μM CQ for 6h. The images are representatives of the plotted data (A, B, and C). (A) Western blot results of p23 protein levels in HeLa-scramble and HeLa-p23KD cells. The plots are the means with error bars (means ± SD, n = 6). (B) Western blot results of AHR protein levels in HeLa-scramble and HeLa-p23KD cells. The plots are the means with error bars (means ± SD, n = 6). (C) Western blot results of A549-WT and A549-p23KD cells treated with 40μM CQ for 6h. The plots are the means with error bars (means ± SD, n = 6). The statistical significance of the differences between group means was evaluated by unpaired *t*-test (A, B) and two-way ANOVA using Tukey's test for multiple comparisons (C). Statistical significance is indicated as follows: * $p < 0.05$, and **** $p < 0.0001$. (D) Western blot results of HeLa-scramble, HeLa-p23KD, A549-scramble, and A549-p23KD cells treated with or without 60μM CQ for 6h. Total protein stain was used for Western normalization.

Transiently transfection of HaloTag-AHR plasmid in HeLa-WT, HeLa-AHRKO, and A549-WT cells.

To study the mechanism of AHR degradation, HaloTag fused AHR protein can be introduced for numerous applications including cellular localization, protein-protein interaction, and protein purification for LC-MS/MS. Here, HaloTag-AHR protein was transiently expressed in HeLa-WT, HeLa-AHRKO and A549-WT cells. HaloTag-AHR was the highest expressed in HeLa-WT cells, but the lowest in A549-WT cells (Fig. 3.9). Unfortunately, HaloTag-AHR failed to stably be expressed in HeLa-WT, HeLa-AHRKO,

and A549-WT cells after one month of G418 selection (could be technical problems, may optimize conditions further).

Fig. 3.9

Overexpression of HaloTag-AHR in HeLa-WT, HeLa-AHRKO and A549-WT cells.

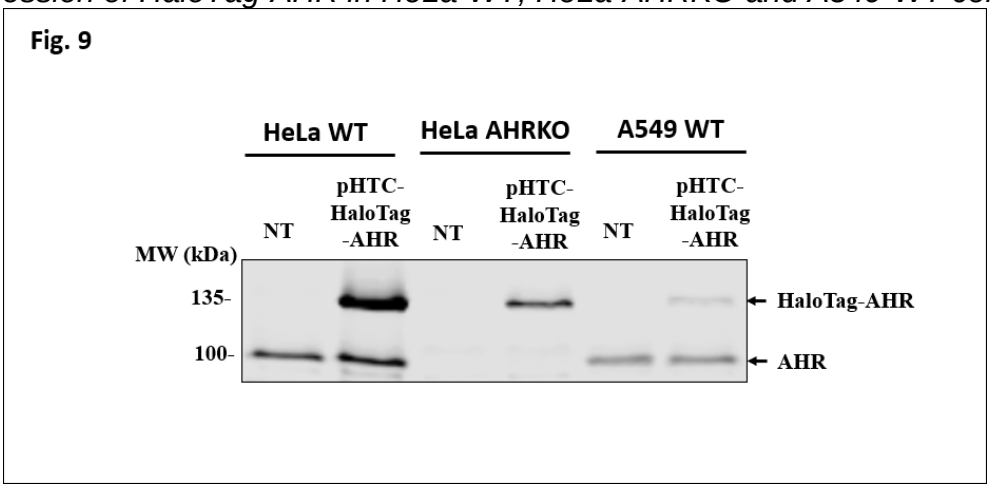

Note. pHTC-HaloTag-AHR plasmids were transiently transfected into HeLa-WT, HeLa-AHRKO, or A549-WT cell lines. After 48 hours of incubation, the cells underwent Western blot analysis to detect the levels of HaloTag-AHR and endogenous AHR protein levels using the SA210 antibody. 30μg of the whole cell extract was loaded into each lane. NT represents no transfection.

Western blot analysis of AHR protein levels in wild type A549, five *AHR* knockout A549 clones, and HaloTag-AHR overexpressed in one of the *AHR* KO A549 clones

Five clones of *AHR* knockout A549 cells (4H2, 2F6, 3C9, 5F2, and 5G11) have been generated by using CRISPR/Cas9 technology. Compared to wild-type A549 cells, there was no clear band around 104kDa confirming that *AHR* gene was successfully knocked out in A549 cells. Nucleotide sequence analysis showed that 5G11 was a

homologous bi-allelic knockout with 47 nucleotide deletions at exon 2, resulting in a frameshift mutation. HaloTag-AHR was stably expressed in *AHR* KO A549 clone 5G11 after one month of G418 selection, the HaloTag-AHR band (~137KDa) was shown clearly with no obvious endogenous AHR band (~104KDa) in this stable cell line (Fig. 3.10).

Fig. 3.10

CRISPR/Cas9-mediated knockout of AHR gene in A549 cell line and HaltoTag-AHR stably overexpressed in AHR KO (5G11) A549 cells.

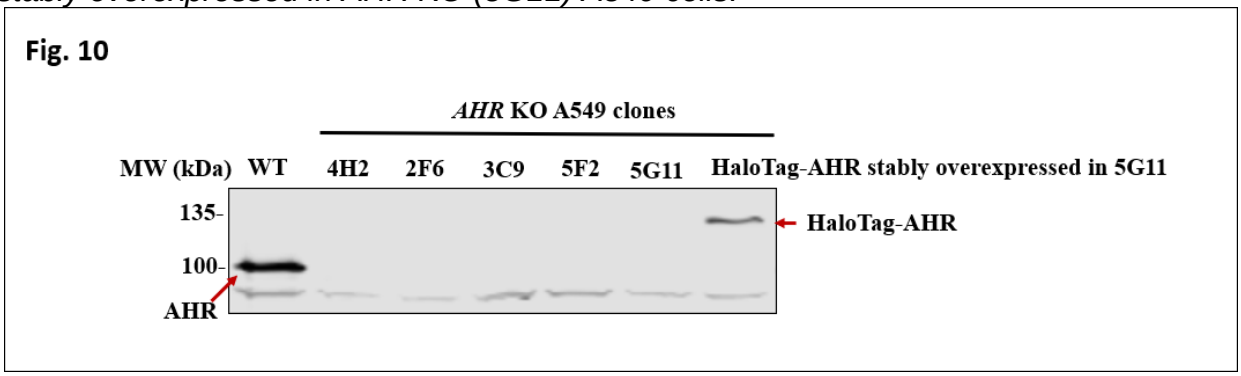

Note. LI-COR Western blot analysis of AHR protein levels in wild type (WT) and five CRISPR/Cas9 *AHR* knockout (KO) clones. The cell lysate in the last lane is from the stable transfection of pHTC-HaloTag AHR in *AHR* KO A549 clone 5G11.

The HaloTag-AHR protein levels were elevated in the stable overexpression of HaloTag-AHR in *AHR* knockout A549 cells upon the lysosomal inhibition

AHR KO A549 clone 5G11 was transiently transfected with pHTC-HaloTag-AHR plasmids using the EndoFectin transfection reagent. After one month of 2mg/ml G418 selection, cells were treated with or without CQ for 6h. We observed that the HaloTag-AHR protein level was increased by 1.4-fold after the lysosomal inhibition (Fig. 3.11),

suggesting that the degradation of exogenous HaloTag-AHR, which was similar to that of endogenous AHR, was inhibited by CQ treatment. In addition, the AviTag-AHR can be recognized by SA210 antibody but not FLAG antibody (M2) (not shown here).

Fig. 3.11

Exogenous HaloTag-AHR protein levels were increased after lysosomal inhibition.

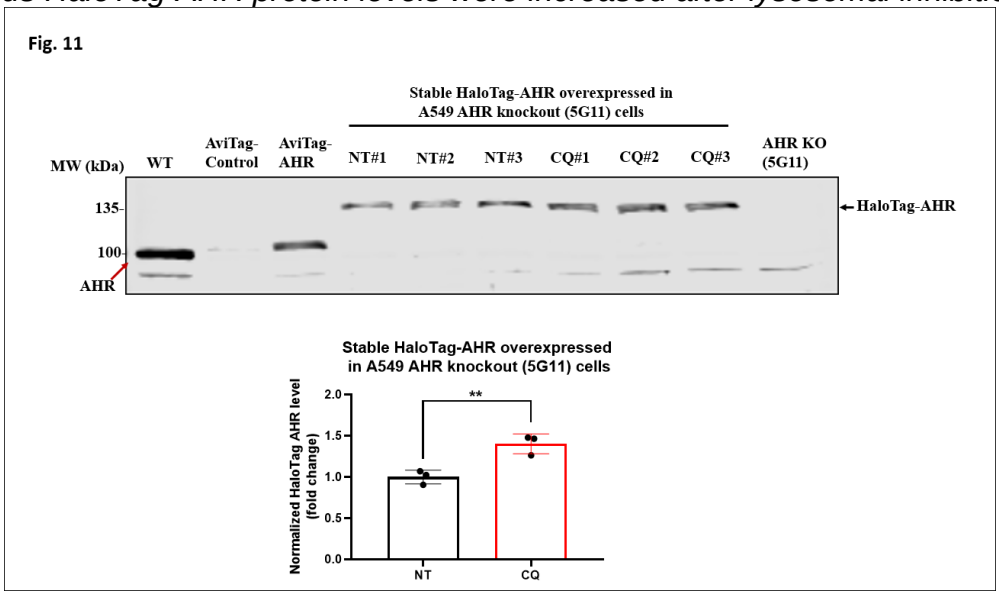

Note. Western blot results of stable expression HaloTag-AHR in *AHR* knockout A549 cells treated with or without 100μM CQ for 6h. The images are representatives of the plotted data. The plots are the means with error bars (means ± SD, n = 3). The statistical significance of the differences between group means was evaluated by unpaired *t*-test. Statistical significance is indicated as follows: ** $p < 0.01$. Lanes 2 and 3 are Western blot results of *AHR* knockout (5G11) A549 cells transiently transfected with AviTag-Control and AviTag-AHR plasmids.

Murine lung carcinoma cell line KLN 205 had no *AHR^d* allele

Since there are more similarities between *hAHR* and *AHR^d* allele. We are curious whether lysosome plays a role in the degradation of *AHR^d* allele protein. *AHR^d* occurs naturally in DBA/2, AKR, 129, SWR, RF, and NZB mouse strains. And KLN205 is a cell isolated from the lung of a DBA/2 mouse with squamous cell carcinoma. We speculated that *AHR^d* was expressed in the KLN205 cell line. SA210 antibody was used in Western blot (Fig. 3.12A), and the A-2 antibody was used in Western blot (Fig. 3.12B). The A-2 antibody is specific for an epitope mapping between amino acid 767-800 at the C-terminus of AHR of mouse origin. However, we did not see an *AHR^d* protein band at ~104kDa (848 aa). Instead, a weak ~95kDa band representing mouse *AHR^b* allele protein appeared in the KLN205 whole cell extract, but its protein levels were not increased by CQ treatment (Fig. 3.12A and 3.12B), suggesting our assumption was incorrect and *AHR^d* allele protein was not expressed in KLN 205.

Fig. 3.12

The AHR protein expression in murine lung carcinoma cell line KLN 205.

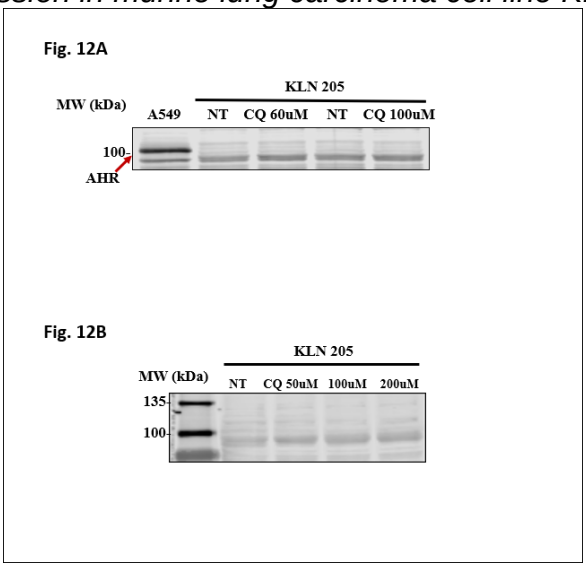

Note. (A) Western blot results of KLN205 cells treated with or without 60μM, 100μM CQ for 6h. A549 whole cell extract was used as a control. Rabbit anti-AHR polyclonal antibody (SA210) was used to detect AHR protein. (B) Western blot results of KLN205 cells treated with or without 50μM, 100μM, and 200 μM CQ for 6h. Mouse anti-AHR monoclonal antibody (A-2) was used to detect AHR protein.

Discussion

Previous studies showed that AHR protein degradation can be regulated by selective macroautophagy, and this degradation was significantly increased when p23 was knocked down in HeLa cells [69]. However, in human lung epithelial carcinoma A549 cells, stable knockdown of p23 reduced AHR protein levels, which could be attributed to the downregulation of AHR mRNA expression and the enhanced AHR protein degradation (Fig. 3.2 and Fig. 3.3). CQ increased AHR protein levels in both A549-WT and A549-p23KD cells to a similar extent, suggesting there was no more lysosomal degradation of AHR was induced by p23 knockdown in A549 cells (Fig. 3.1). To find out whether proteasome degradation could be involved in the p23 knockdown induced AHR protein degradation, MG132 was used to inhibit the 26S proteasome degradation. Intriguingly, we observed a reduced AHR protein level, instead of an increased AHR protein level, in both A549-WT and A549-p23KD cells (Fig. 3.4). In addition, CQ treatment reversed the AHR reduction to a similar extent in both cell lines. The observed reduction of AHR protein levels may be attributed to the fact that MG132 has been shown to promote autophagy by enhancing the stability of Atg proteins, in addition to its known role as a proteasome inhibitor. p23 knockdown induced AHR

protein degradation was not due to the proteasome degradation since it could not be reversed by MG132. Furthermore, the degradation of AHR protein via the autophagic-lysosome pathway was not enhanced in A549-p23KD cells in the presence of MG132, partially suggesting that p23 knockdown failed to further enhance autophagy in A549 cells (Fig. 3.4). The autophagic flux was not increased in A549-p23KD cells when compared to wild-type A549 cells, further suggesting that p23 knockdown didn't change the autophagic activity in A549 cells (Fig. 3.5). The proximity ligation assay, which was used to determine the protein-protein interaction visually, confirmed that AHR interacted with LC3B in A549 cells after CQ treatment (Fig. 3.6). However, this interaction was observed in both WT and p23KD A549 cells, without any increased PLA signals within A549-p23KD cells (Fig. 3.6). However, selectively inhibiting macroautophagy by 3MA failed to increase AHR protein levels in both A549-WT and A549-LAMP2KD cells, suggesting there might be a possibility that macroautophagy was not involved in the degradation of basal AHR (Fig. 3.7). In order to directly determine the discrepancy between HeLa-p23KD and A549-p23KD cells, HeLa-scramble and HeLa-p23KD cells constructed by Yujie Yang were thawed from liquid nitrogen. We were astonished to observe that a 52% knockdown of p23 resulted in only a 14% reduction of AHR protein levels in HeLa cells (Fig. 3.8A and Fig. 3.8B), which diverged from our previous data that a ~50% knockdown of p23 led to a ~50% reduction of the AHR protein levels in HeLa cells. This could be due to the AHR protein "adapts" to the low level of p23. Thus, other regulatory mechanisms might be involved in these upregulated AHR protein levels. In addition, we cannot rule out the possibility that the rest of the p23 protein levels could be sufficient to keep the basal AHR protein levels in HeLa cells. Therefore, the complete

elimination of p23 in HeLa cells by CRISPR/Cas9 mediated gene knockout could provide further elucidation on the underlying mechanisms clearly.

The HaloTag protein which is a modified haloalkane dehalogenase has been engineered to covalently bind to synthetic HaloTag ligands. The ligands consist of a chloroalkane linker connected to a range of beneficial compounds, including fluorescent dyes, affinity handles, or solid surfaces. The covalent bond formed between the HaloTag and chloroalkane linker is irreversible, highly specific, and rapid [126]. To study the mechanism of AHR degradation, HaloTag fused AHR protein can be introduced for numerous applications including cellular localization, protein-protein interaction, protein imaging, and protein purification for LC-MS/MS analysis. First of all, the HaloTag-AHR protein should be successfully overexpressed in HeLa cells or A549 cells to choose the optimal expression system. The procedure was as follows: HeLa-WT, HeLa-*AHR*KO, A549-WT, and A549-*AHR*KO cells were transiently transfected with pHTC-HaloTag-AHR-CMV-neo plasmids, respectively; cells were selected in the presence of 2mg/ml G418 for one month. Western blot results showed that HaloTag-AHR was the highest expressed in HeLa-WT cells transiently but was stably expressed in the A549 *AHR*KO 5G11 clone (Fig. 3.9 and Fig. 3.10). Additionally, the degradation of exogenous HaloTag-AHR was similar to that of the endogenous AHR since its protein level was increased in the presence of CQ (Fig. 3.11). Lastly, our western blot results showed that the AHR^d allele was not expressed in murine lung carcinoma cell line KLN205 (Fig. 3.12). One alternative approach to investigate the degradation of the AHR^d allele protein involves the overexpression of this AHR^d cDNA within a mouse *AHR* knockout cell line.

Conclusions

In summary, stable knockdown of p23 in A549 cells reduced AHR protein levels. The basal AHR protein level was regulated by lysosomal inhibitor CQ, but the autophagic activity was not upregulated by p23 knockdown in A549 cells. Collectively, there could be various ways to control AHR protein content in A549 cells besides ligands or geldanamycin caused 26S proteasome degradation. We aim to modulate the degradation of AHR protein via autophagy or the co-chaperone p23 in order to govern the magnitude and duration of the AHR-mediated target genes transcription in human lung epithelial carcinoma A549 cells. Meanwhile, the successful overexpression of the HaloTag-AHR fusion protein has opened up a new avenue for investigating the degradation mechanisms of AHR.

Materials and Methods

Reagents and Antibodies

CQ, actinomycin-D, rabbit anti-LC3B antibody (L7543), PMSF, leupeptin, and Duolink proximity ligation assay kit were purchased from Sigma-Aldrich (St. Louis, MO, USA). (S)-MG132 and 3MA were purchased from Cayman Chemical (Ann Arbor, MI, USA). G418 and puromycin were purchased from Goldbio (St Louis, MO, USA). pLKO.1 Lentiviral LAMP2 shRNA plasmid, pLKO.1 Lentiviral p23 shRNA plasmid and pLKO.1 Lentiviral scramble shRNA plasmid were purchased from Dharmacon (Lafayette, CO, USA). pCMV-VSV-G was a gift from Bob Weinberg (Addgene plasmid # 8454; http://n2t.net/addgene:8454; RRID: Addgene_8454). pCMV-dR8.2 dvpr was a gift from Bob Weinberg (Addgene plasmid # 8455; http://n2t.net/addgene:8455; RRID: Addgene_8455). EndoFectin™ transfection reagent, pReceiver-AviTag-FLAG-Control

and pReciever-AviTag-FLAG-AHR plasmids were purchased from GeneGopoeia (Rockville, MD, USA). TRI Reagent and Direct-zol RNA miniprep kit were purchased from Zymo Research (Irvine, CA, USA). MMLV high performance reverse transcriptase was purchased from Epicentre (Madison, WI, USA). iTaq SYBR green supermix was purchased from Bio-Rad (Hercules, CA, USA). EnGen® Spy Cas9 NLS was purchased from NEB (Ipswich, MA, USA), multi-guide sgRNA was purchased from Synthego (Redwood, CA, USA), Lipofectamine RNAiMAX was purchased from Thermo Fisher Scientific (Waltham, MA, USA), QuickExtract DNA extraction solution was purchased from Lucigen (Middleton, WI, USA). PCR Master Mix and pHTC HaloTag® CMV-neo Vector were purchased from Promega (Madison, WI, USA). Mouse anti-p23 monoclonal antibody (JJ3), FBS (HyClone), DMEM (HyClone) and Opti-MEM reduced serum medium were purchased from Thermo Fisher Scientific (Waltham, MA, USA). GlutaMAX-I and penicillin-streptomycin were purchased from Invitrogen (Carlsbad, CA, USA). Rabbit anti-AHR polyclonal antibody (SA210) was purchased from Enzo Life Sciences (Farmingdale, NY, USA). Mouse anti-LAMP2 monoclonal antibody (H4B4), Cycloheximide, and mouse anti-AHR monoclonal antibody (A-3x), mouse anti-AHR monoclonal antibody (A-2) were purchased from Santa Cruz Biotechnology (Dallas, TX, USA). Donkey anti-rabbit and donkey anti-mouse secondary antibody conjugated with IRDye 680 or 800CW, RevertTM 700 Total Protein Stain and nitrocellulose membrane were purchased from LI-COR Bioscience (Lincoln, NE, USA).

Cell culture

A549 cells were a gift from Dr. John Livesey (University of the Pacific) and were authenticated by ATCC before being used for experiments in this paper. HeLa cell line

was authenticated by ATCC. KLN205 cell line (B106A liquid nitrogen tank W-6) was purchased from ATCC. *AHR* knockout HeLa cell line was purchased from Ubigene Biosciences Co., Ltd (Guangzhou, China). AD293 cells were purchased from Agilent Technologies (Santa Clara, CA, USA). All the cell lines were cultured in DMEM supplemented with 10% fetal bovine serum (FBS), 1% penicillin-streptomycin and 1% GlutaMAX-I at 37 ℃, 5% CO_2.

Preparation of whole cell extract and Western blot analysis

A549 cells, HeLa, or KLN205 cells were scraped in cold PBS and centrifuged at 400g for 5 min to collect cell pellets. The collected cells were washed once with cold PBS and then lysed in lysis buffer (25mM HEPES pH7.4, 0.4 M KCl, 1mM EDTA, 1mM DTT, 10% glycerol, 1% NP40, 1mM PMSF, and 2μg/ml leupeptin). After 3 cycles of freeze and thaw, cell lysates were kept on ice for 30 min and then centrifuged at 16,000g for 15 min at 4 ℃. The supernatants were used as whole cell extracts. Total protein concentrations were measured by BCA assay. If not specified, proteins in 20μg of whole cell extract from each sample were separated by 12% SDS-PAGE and then transferred to nitrocellulose membranes via wet transfer method. 15% SDS-PAGE gel was used to separate p23 and LC3B protein. Total protein staining was determined using LI-COR Revert™ 700 Total Protein Stain for normalization. Non-specific binding was blocked in blocking buffer (PBS, 0.1% Tween-20, 5% BSA) for 1h. The primary antibodies and their dilution are listed as follows: 1:2000 for anti-AHR (SA210); 1:200 for anti-LAMP2 (H4B4); 1:1000 for anti-p23 (JJ3); 1:1000 for anti-LC3B (L7543). After washing with PBST (PBS and 0.1% Tween-20) 5 times, nitrocellulose membrane was incubated in 1:10,000 dilution of donkey secondary antibody conjugated with IRDye

680or 800 CW. Results were obtained and quantified by using LI-COR Odyssey CLx imaging system (Lincoln, NE, USA).

RNA extraction and reverse transcription-quantitative polymerase chain reaction (RT-qPCR)

Total RNA was extracted from A549 cells using TRI Reagent (Zymo Research) and RNA miniprep kit (Direct-zol) according to the manufacturer's recommendations. cDNA was reverse transcribed from 1μg of RNA by using MMLV high performance reverse transcriptase (Epicentre) into a final volume of 20 μl cDNA solution and 1 μl of it was used as the qPCR template. qPCR was performed with iTaq SYBR green supermix (Bio-rad, USA) on a CFX Connect real-time PCR operating system (Bio-rad, USA) according to the following protocol: 95℃ for 2 min, 40 cycles of 95 ℃ for 15s and 60 ℃ for 1min. Relative gene expression was analyzed by the $2^{-\Delta\Delta Cq}$ method [112] and *18s* rRNA was used as an internal control for normalization. The primer sequences were as follows: *18s* Forward: 5'-CGCCCCCTCGATGCTCTTAG-3' and Reverse: 5'-CGGCGGGTCATGGGAATAAC-3'; *AHR* Forward: 5'-ACATCACCTACGCCAGTCGC-3' and Reverse: 5'-TCTATGCCGCTTGGAAGGAT -3'.

Generation of p23, LAMP2 stable knockdown A549 cells using lentivirus

Lentivirus containing p23 or LAMP2 shRNA was prepared as follows: AD293 cells (7×10^5) in 5ml of growth media (10% fetal bovine serum and 2mM GlutaMAX-I in DMEM) were seeded in a 25 cm^2 flask. Cells were incubated at 37 ℃, 5% CO_2 overnight. Then AD293 cells were transfected using 10μl EndoFectin™ transfection reagent with 5μg plasmids (2.5μg of pLKO.1 specific shRNA plasmid, 1.875μg of the pCMV-dR8.2 dvpr packaging plasmid, and 0.625μg of the pCMV-VSV-G envelope plasmid). Fresh

complete medium was replaced 15h after transfection. After 24h, the medium containing lentiviral particles was transferred to a 15ml tube and stored at 4 ℃. Another 5ml of fresh complete medium was added to the cells and the medium containing lentiviral particles was harvested after 24h of incubation. The combined medium was centrifuged at 400g for 5min to pellet any AD293 cells and the supernatant was used for infection. Stable p23 or LAMP2 knockdown cell lines were generated as follows: A549 cells were seeded in a 25 cm^2 flask to achieve 50-70% confluence on the next day. Fresh complete medium containing 8μg/mL polybrene was replaced. 500μl of medium containing lentiviral particles was added into the flask. After 24h, the medium was replaced with fresh complete medium containing 1.5μg/ml of puromycin for stable cell line selection. Change to fresh medium containing puromycin every 2-3 days. p23 knockdown stable A549 cells were generated using pLKO.1 Lentiviral (TRC) p23 siRNA #1475 plasmid; LAMP2 knockdown stable A549 cells were generated using pLKO.1 Lentiviral (TRC) LAMP2 shRNA #4 (TRCN0262) plasmid.

Transient transfection

A549 cells were seeded in a 6-well plate at 90-95% confluency at the time of transfection. Plasmid DNA, EndoFectin™ transfection reagent, and Opti-MEM were equilibrated to room temperature before use. Cells were transfected with 4μg of plasmid and 8μl of transfection reagent. Both plasmids and transfection reagent were diluted in the Opti-MEM, respectively. Then the diluted transfection reagent and the diluted DNA were combined and kept at room temperature for 20min to allow DNA-transfection reagent complexes to form. The combined complexes were added to each well and mixed gently. The cells were harvested for analysis after 48h of incubation at 37 ℃, 5%

CO_2. For stable cell line selection, the medium was replaced with fresh complete medium containing 2mg/ml of G418 after 48h of incubation. Cells were passaged in T75 flasks with G418 selection for about one month, followed by Western blot analysis.

Proximity Ligation Assay (PLA)

The microscope glass coverslips (~1 cm^2) were placed in the wells of a 12-well plate, and cells were seeded onto them and grown to approximately 70-80% of confluence. Cells were treated with or without CQ for 6h and then were rinsed with ice-cold PBS twice. Cells were fixed and permeabilized with 100% methanol (chilled at -20℃ before) for 5min. After 3 times wash with ice-cold PBS, cells were ready for proximity ligation assay according to the Duolink® PLA Fluorescence Protocol. Briefly, one drop of Duolink Blocking Solution was added to each microscope glass coverslips to completely cover the samples. Samples were incubated at 37℃ for 1h, followed by incubation with mouse anti-AHR monoclonal antibody (A-3x) and rabbit anti-LC3B monoclonal antibody (1:100 diluted in the Duolink antibody diluent) for 1h at 37℃. Samples were washed 2×5min in 1×wash buffer A, followed by incubation with PLUS and MINUS PLA probes (1:5 diluted in the Duolink antibody diluent) for 1h at 37℃. Samples were washed 2×5min in 1×wash buffer A, followed by incubation with ligase (1:40 diluted in 1×ligation buffer) for 30min at 37℃. Samples were washed 2×5min in 1×wash buffer A, followed by incubation with polymerase (1:80 diluted in 1×amplification buffer) for 100 min at 37℃. Finally, samples were washed with 1×wash buffer B for 2×10 min and 0.01×wash buffer B for 1 min. Nucleus was stained by 1μg/mL DAPI in water for 1min. Nail polish was used to seal the edges of the coverslip to the

microscope slide. Samples were imaged by using an inverted microscope (BZ-X700, KEYENCE, USA) with a camera.

Statistical analysis

GraphPad Prism 8 software (La Jolla, CA) was used for statistical analysis. The statistical significance of the differences between group means are evaluated by one-way or two-way ANOVA using Tukey or Sidak test for multiple comparisons. Statistical significance was indicated as follows: *$p < 0.05$, **$p < 0.01$, ***$p < 0.001$, ****$p < 0.0001$, and $p > 0.05$ (ns, not significant). The two-tailed unpaired *t*-test was used to determine the statistical significance in Fig. 3.1A, 3.1B, 3.2A, 3.3, 3.8A, 3.8B, 3.11.

CHAPTER 4: SUMMARY AND DISCUSSION

In our study, we provided experimental evidence for the degradation of basal AHR in the lysosome via CMA in A549 cells. We confirmed that AHR protein, a cytoplasmic ligand-activated transcription factor, was increased upon treatment with a general lysosome inhibitor CQ. Notably, our data illustrated that CMA plays an important role in basal AHR degradation. We also provided evidence that macroautophagy was not involved in the lysosome degradation of AHR under basal conditions. Nevertheless, the unsuccessful knockdown of LC3B in A549 cells hindered my study on macroautophagy-mediated lysosomal degradation further. Moreover, it has been reported that several proteins that possess the ability to inhibit cell proliferation and cancer metastasis, have been confirmed to undergo degradation via CMA, such as RND3 and PED proteins [127][128]. On the other hand, certain proteins that facilitate the growth of cancer and metastasis are also degraded through CMA, including HIF-1a and PKM2 [129][130]. Here, we demonstrated that activated degradation of AHR through CMA by 6-AN treatment could result in the impaired migration and invasion capacity of A549 cells. It was mediated by AHR since knockout of *AHR* in A549 cells abolished the 6-AN's effect on migration and invasion. However, three of the EMT markers failed to fully explain the phenomenon. We cannot rule out the possibility that the effect of 6-AN and LAMP2 knockdown on the expression of EMT markers is independent of AHR since CMA could influence the process of EMT directly. Meanwhile, a comprehensive analysis of the EMT process is required for a better understanding of the role of CMA in AHR-mediated EMT program. Our research supported that the AHR

promotes the EMT process when complete knockout of AHR in A549 cells using CRISPR/Cas9 technology, which is contradictory to the inhibitory role of AHR on the EMT process in NSCLC cells reported in recent years [131][132].

Here, we provided a potential possibility that the autophagy-lysosome pathway might also play a role in the ligand or GA triggered AHR degradation apart from the 26S ubiquitin-proteasome pathway. There are similarities among the 6-AN, Bap, and GA treatments. AHR degradation was induced by all three drugs, but the reduction of AHR protein level was slower with the 6-AN treatment. 6-AN was widely used to induce CMA. It is an analog of niacin and works by competing with niacin for $NAD(P^+)$ to form 6-$ANAD(P^+)$. 6-$ANAD(P^+)$ acts as a competitive inhibitor for $NAD(P^+)$-requiring processes, including the production of NADPH. Consequently, it leads to the creation of an oxidative environment within cells. Oxidation of CMA substrates and oxidative stress itself activate the CMA process for translocation of substrates into the lysosome for degradation [133]. Benzo[a]pyrene (BaP), a polycyclic aromatic hydrocarbon (PAH), is primarily produced through the combustion of fossil fuels, wood, and other organic materials. It has been revealed that the AHR signaling pathway plays a crucial role in the BaP-induced reactive oxygen species (ROS) [134]. Despite the fact that the cytotoxicity of GA has been related to its disruption of Hsp90 complexes, this compound also possesses a benzoquinone moiety which is responsible for the production of ROS [135]. Thus, both Bap and GA could induce oxidative stress via the production of ROS. Undoubtedly, ubiquitin-proteasome is the major pathway accounting for the Bap and GA induced AHR degradation. However, the fact that a particular protein could be degraded by different proteolytic systems based on cellular conditions has been confirmed by

numerous studies. It is conceivable that the activation of the ubiquitin-proteasome pathway under oxidative stress enables the efficient elimination of the oxidized proteins rapidly. However, if the oxidative conditions are sustained, the oxidized proteins are directed toward lysosomes through CMA, allowing the proteasome to focus on crucial regulatory functions. However, we cannot accurately quantify the amount of proteins that are delivered to one or another proteolytic pathway since most of the experiments to quantify it using inhibitors of one proteolytic pathway probably enhance the activity of another pathway due to the compensatory mechanisms. Our lab observed that proteasome inhibitor MG132 induced basal AHR degradation in A549, HeLa, and Hepa1c1c7 with no ligand treatment. which can be explained by the literature report that MG132 can induce autophagy [79][80].

In summary, we provided evidence to elucidate that AHR undergoes lysosomal degradation through CMA in A549 cells from the following respects: 1) the lysosomal inhibitor CQ blocked AHR degradation and enhanced the Bap-induced *cyp1a1* transcription; 2) macroautophagy does not contribute to the degradation of basal AHR since no significant effect of Met, Rap and ATG5 knockdown on AHR protein levels; 3) CMA activator 6-AN induced AHR degradation and blocked the Bap-induced *cyp1a1* transcription, knockdown of LAMP2 alleviated CQ induced AHR accumulation, CMA motif identification, and AHR interacted with CMA regulators, all of them led us to believe that basal AHR degradation is regulated by CMA. Additionally, stable knockdown of p23 in A549 cells reduced the AHR protein levels, partially due to an elevated AHR protein degradation, which could be reversed by lysosome inhibitor CQ, but not proteasome inhibitor MG132. p23 knockdown failed to activate macroautophagy

for AHR protein degradation via lysosome in A549 cells. HaloTag-AHR was successfully overexpressed in HeLa and A549 cells for the following LC-MS/MS analysis.

References

1 Chen, J.; Poonam Yakkundi; Chan, W. K. Down-Regulation of P23 in Normal Lung Epithelial Cells Reduces Toxicities from Exposure to Benzo[A]Pyrene and Cigarette Smoke Condensate via an Aryl Hydrocarbon Receptor-Dependent Mechanism. *Toxicological Sciences* **2018**, *167* (1), 239–248.

2 Opitz, C. A.; Holfelder, P.; Prentzell, M. T.; Trump, S. The Complex Biology of Aryl Hydrocarbon Receptor Activation in Cancer and Beyond. *Biochemical Pharmacology* **2023**, *216* (115798), 115798.

3 Xu, C.; Li, C. Y.-T.; Kong, A.-N. T. Induction of Phase I, II and III Drug Metabolism/Transport by Xenobiotics. *Archives of Pharmacal Research* **2005**, *28* (3), 249–268.

4 Haarmann-Stemmann, T.; Abel, J. The Arylhydrocarbon Receptor Repressor (AhRR): Structure, Expression, and Function. *Biological Chemistry* **2006**, *387* (9).

5 Davarinos, N. A.; Pollenz, R. S. Aryl Hydrocarbon Receptor Imported into the Nucleus Following Ligand Binding Is Rapidly Degraded via the Cytosplasmic Proteasome Following Nuclear Export. *Journal of Biological Chemistry* **1999**, *274* (40), 28708–28715.

6 Larigot, L.; Juricek, L.; Dairou, J.; Coumoul, X. AhR Signaling Pathways and Regulatory Functions. *Biochimie Open* **2018**, *7* (7), 1–9.

7 García-Lara, L.; Pérez-Severiano, F.; González-Esquivel, D.; Elizondo, G.; Segovia, J. Absence of Aryl Hydrocarbon Receptors Increases Endogenous

Kynurenic Acid Levels and Protects Mouse Brain against Excitotoxic Insult and Oxidative Stress. *Journal of Neuroscience Research* **2015**, *93* (9), 1423–1433.

8 Opitz, C. A.; Litzenburger, U. M.; Sahm, F.; Ott, M.; Tritschler, I.; Trump, S.; Schumacher, T.; Jestaedt, L.; Schrenk, D.; Weller, M.; Jugold, M.; Guillemin, G. J.; Miller, C. L.; Lutz, C.; Radlwimmer, B.; Lehmann, I.; von Deimling, A.; Wick, W.; Platten, M. An Endogenous Tumour-Promoting Ligand of the Human Aryl Hydrocarbon Receptor. *Nature* **2011**, *478* (7368), 197–203.

9 Safe, S.; Lee, S.-O.; Jin, U.-H. Role of the Aryl Hydrocarbon Receptor in Carcinogenesis and Potential as a Drug Target. *Toxicological Sciences* **2013**, *135* (1), 1–16.

10 Su, J.-M.; Lin, P.; Chang, H. Prognostic Value of Nuclear Translocation of Aryl Hydrocarbon Receptor for Non-Small Cell Lung Cancer. *Anticancer Research* **2013**, *33* (9), 3953–3961.

11 Vogel, C. F. A.; Khan, E. M.; Leung, P. S. C.; Gershwin, M. E.; Chang, W. L. W.; Wu, D.; Haarmann-Stemmann, T.; Hoffmann, A.; Denison, M. S. Cross-Talk between Aryl Hydrocarbon Receptor and the Inflammatory Response. *Journal of Biological Chemistry* **2013**, *289* (3), 1866–1875.

12 Saito, R.; Miki, Y.; Hata, S.; Takagi, K.; Iida, S.; Oba, Y.; Ono, K.; Ishida, T.; Suzuki, T.; Noriaki Ohuchi; Sasano, H. Aryl Hydrocarbon Receptor in Breast Cancer—a Newly Defined Prognostic Marker. *Hormones and Cancer* **2013**, *5* (1), 11–21.

13 Barhoover, M. A.; Hall, J. M.; Greenlee, W. F.; Thomas, R. S. Aryl Hydrocarbon Receptor Regulates Cell Cycle Progression in Human Breast Cancer Cells via a

Functional Interaction with Cyclin-Dependent Kinase 4. *Molecular Pharmacology* **2010**, *77* (2), 195–201.

14 Abdelrahim, M.; Smith, R.; Safe, S. Aryl Hydrocarbon Receptor Gene Silencing with Small Inhibitory RNA Differentially Modulates Ah-Responsiveness in MCF-7 and HepG2 Cancer Cells. *Molecular Pharmacology* **2003**, *63* (6), 1373–1381.

15 Watabe, Y.; Nazuka, N.; Tezuka, M.; Shimba, S. Aryl Hydrocarbon Receptor Functions as a Potent Coactivator of E2F1-Dependent Trascription Activity. *Biological & Pharmaceutical Bulletin* **2010**, *33* (3), 389–397.

16 Kolluri, S. K.; Weiss, C.; Koff, A.; Göttlicher, M. P27Kip1 Induction and Inhibition of Proliferation by the Intracellular Ah Receptor in Developing Thymus and Hepatoma Cells. *Genes & Development* **1999**, *13* (13), 1742–1753.

17 Caruso, J. A.; Mathieu, P. A.; Joiakim, A.; Leeson, B.; Kessel, D.; Sloane, B. F.; Reiners, J. J. Differential Susceptibilities of Murine Hepatoma 1c1c7 and Tao Cells to the Lysosomal Photosensitizer NPe6: Influence of Aryl Hydrocarbon Receptor on Lysosomal Fragility and Protease Contents. *Molecular Pharmacology* **2004**, *65* (4), 1016–1028.

18 Bock, K. W.; Köhle, C. Ah Receptor- and TCDD-Mediated Liver Tumor Promotion: Clonal Selection and Expansion of Cells Evading Growth Arrest and Apoptosis. *Biochemical Pharmacology* **2005**, *69* (10), 1403–1408.

19 Christoph Köhle; Harald Gschaidmeier; Lauth, D.; Topell, S.; Zitzer, H.; Karl Walter Bock. 2,3,7,8-Tetrachlorodibenzo- P -Dioxin (TCDD)-Mediated Membrane Translocation of C-Src Protein Kinase in Liver WB-F344 Cells. *Archives of Toxicology* **1999**, *73* (3), 152–158.

20 Ikuta, T.; Kawajiri, K. Zinc Finger Transcription Factor Slug Is a Novel Target Gene of Aryl Hydrocarbon Receptor. *Experimental Cell Research* **2006**, *312* (18), 3585–3594.

21 Ikuta, T.; Kobayashi, Y.; Kawajiri, K. Cell Density Regulates Intracellular Localization of Aryl Hydrocarbon Receptor. *Journal of Biological Chemistry* **2004**, *279* (18), 19209–19216.

22 Thackaberry, E. A.; Jiang, Z.; Johnson, C. D.; Ramos, K. S.; Walker, M. K. Toxicogenomic Profile of 2,3,7,8-Tetrachlorodibenzo-p-Dioxin in the Murine Fetal Heart: Modulation of Cell Cycle and Extracellular Matrix Genes. *Toxicological Sciences* **2005**, *88* (1), 231–241.

23 Villano, C. M.; Murphy, K. A.; Akintobi, A.; White, L. A. 2,3,7,8-Tetrachlorodibenzo-p-Dioxin (TCDD) Induces Matrix Metalloproteinase (MMP) Expression and Invasion in A2058 Melanoma Cells. *Toxicology and Applied Pharmacology* **2006**, *210* (3), 212–224.

24 Peng, T.; Chen, J.; Mao, W.; Song, X.; Chen, M. Aryl Hydrocarbon Receptor Pathway Activation Enhances Gastric Cancer Cell Invasiveness Likely through a C-Jun-Dependent Induction of Matrix Metalloproteinase-9. *BMC Cell Biology* **2009**, *10* (1).

25 Santiago-Josefat, B.; Mulero-Navarro, S.; Dallas, S. L.; Fernandez-Salguero, P. M. Overexpression of Latent Transforming Growth Factor-β Binding Protein 1 (LTBP-1) in Dioxin Receptor-Null Mouse Embryo Fibroblasts. *Journal of Cell Science* **2004**, *117* (6), 849–859.

26 Wang, F.; Samudio, I.; Safe, S. Transcriptional Activation of Cathepsin D Gene Expression by 17β-Estradiol: Mechanism of Aryl Hydrocarbon Receptor-Mediated Inhibition. *Molecular and Cellular Endocrinology* **2001**, *172* (1-2), 91–103.

27 Son, D.-S.; Rozman, K. 2,3,7,8-Tetrachlorodibenzo- P -Dioxin (TCDD) Induces Plasminogen Activator Inhibitor-1 through an Aryl Hydrocarbon Receptor-Mediated Pathway in Mouse Hepatoma Cell Lines. *Archives of Toxicology* **2002**, *76* (7), 404–413.

28 Angel Carlos Roman; Jose Maria Carvajal-Gonzalez; Rico-Leo, E. M.; Fernández-Salguero, P. M. Dioxin Receptor Deficiency Impairs Angiogenesis by a Mechanism Involving VEGF-A Depletion in the Endothelium and Transforming Growth Factor-β Overexpression in the Stroma. *Journal of Biological Chemistry* **2009**, *284* (37), 25135–25148.

29 Zudaire, E.; Cuesta, N.; Murty, V.; Woodson, K.; Adams, L.; Gonzalez, N.; Martínez, A.; Narayan, G.; Kirsch, I.; Franklin, W.; Hirsch, F.; Birrer, M.; Cuttitta, F. The Aryl Hydrocarbon Receptor Repressor Is a Putative Tumor Suppressor Gene in Multiple Human Cancers. *Journal of Clinical Investigation* **2008**, *118* (640-650).

30 Zaffagnini, G.; Martens, S. Mechanisms of Selective Autophagy. *Journal of Molecular Biology* **2016**, *428* (9), 1714–1724.

31 Rogov, V.; Dötsch, V.; Johansen, T.; Kirkin, V. Interactions between Autophagy Receptors and Ubiquitin-like Proteins Form the Molecular Basis for Selective Autophagy. *Molecular Cell* **2014**, *53* (2), 167–178.

32 Kabeya, Y.; Mizushima, N.; Yamamoto, A.; Oshitani-Okamoto, S.; Ohsumi, Y.; Yoshimori, T. LC3, GABARAP and GATE16 Localize to Autophagosomal Membrane Depending on Form-II Formation. *Journal of Cell Science* **2004**, *117* (13), 2805–2812.

33 Schreiber, A.; Peter, M. Substrate Recognition in Selective Autophagy and the Ubiquitin–Proteasome System. *Biochimica et Biophysica Acta (BBA) - Molecular Cell Research* **2014**, *1843* (1), 163–181.

34 Lamark, T.; Svenning, S.; Johansen, T. Regulation of Selective Autophagy: The P62/SQSTM1 Paradigm. *Essays In Biochemistry* **2017**, *61* (6), 609–624.

35 Pankiv, S.; Clausen, T. H.; Lamark, T.; Brech, A.; Bruun, J.-A.; Outzen, H.; Øvervatn, A.; Bjørkøy, G.; Johansen, T. P62/SQSTM1 Binds Directly to Atg8/LC3 to Facilitate Degradation of Ubiquitinated Protein Aggregates by Autophagy. *Journal of Biological Chemistry* **2007**, *282* (33), 24131–24145.

36 Long, J.; Thomas; Cavey, J. R.; Sheppard, P. W.; Ralston, S. H.; Layfield, R.; Searle, M. S. Ubiquitin Recognition by the Ubiquitin-Associated Domain of P62 Involves a Novel Conformational Switch. *Journal of Biological Chemistry* **2008**, *283* (9), 5427–5440.

37 Korolchuk, V. I.; Mansilla, A.; Menzies, F. M.; Rubinsztein, D. C. Autophagy Inhibition Compromises Degradation of Ubiquitin-Proteasome Pathway Substrates. *Molecular Cell* **2009**, *33* (4), 517–527.

38 Komatsu, M.; Waguri, S.; Chiba, T.; Murata, S.; Iwata, J.; Tanida, I.; Ueno, T.; Koike, M.; Uchiyama, Y.; Kominami, E.; Tanaka, K. Loss of Autophagy in the

Central Nervous System Causes Neurodegeneration in Mice. *Nature* **2006**, *441* (7095), 880–884.

39 Cuervo, A. M.; Terlecky, S. R.; Dice, J. F.; Knecht, E. Selective Binding and Uptake of Ribonuclease a and Glyceraldehyde-3-Phosphate Dehydrogenase by Isolated Rat Liver Lysosomes. *Journal of Biological Chemistry* **1994**, *269* (42), 26374–26380.

40 Bandyopadhyay, U.; Kaushik, S.; Varticovski, L.; Cuervo, A. M. The Chaperone-Mediated Autophagy Receptor Organizes in Dynamic Protein Complexes at the Lysosomal Membrane. *Molecular and Cellular Biology* **2008**, *28* (18), 5747–5763.

41 Koga, H.; Martinez-Vicente, M.; Macian, F.; Verkhusha, V. V.; Cuervo, A. M. A Photoconvertible Fluorescent Reporter to Track Chaperone-Mediated Autophagy. *Nature Communications* **2011**, *2* (1).

42 Fred Dice, J. Peptide Sequences That Target Cytosolic Proteins for Lysosomal Proteolysis. *Trends in Biochemical Sciences* **1990**, *15* (8), 305–309.

43 Lv, L.; Li, D.; Zhao, D.; Lin, R.; Chu, Y.; Zhang, H.; Zha, Z.; Liu, Y.; Li, Z.; Xu, Y.; Wang, G.; Huang, Y.; Xiong, Y.; Guan, K.-L.; Lei, Q.-Y. Acetylation Targets the M2 Isoform of Pyruvate Kinase for Degradation through Chaperone-Mediated Autophagy and Promotes Tumor Growth. *Molecular Cell* **2011**, *42* (6), 719–730.

44 Sahu, R.; Kaushik, S.; Clement, C. C.; Cannizzo, E. S.; Scharf, B.; Follenzi, A.; Potolicchio, I.; Nieves, E.; Cuervo, A. M.; Santambrogio, L. Microautophagy of Cytosolic Proteins by Late Endosomes. *Developmental Cell* **2011**, *20* (1), 131–139.

45 Cuervo, A. M.; Knecht, E.; Terlecky, S. R.; Dice, J. F. Activation of a Selective Pathway of Lysosomal Proteolysis in Rat Liver by Prolonged Starvation. *American Journal of Physiology-Cell Physiology* **1995**, *269* (5), C1200–C1208.

46 Massey, A. C.; Kaushik, S.; Sovak, G.; Kiffin, R.; Cuervo, A. M. Consequences of the Selective Blockage of Chaperone-Mediated Autophagy. *Proceedings of the National Academy of Sciences of the United States of America* **2006**, *103* (15), 5805–5810.

47 Chava, S.; Lee, C.; Aydin, Y.; Chandra, P. K.; Dash, A.; Chedid, M.; Thung, S. N.; Moroz, K.; Wu, T.; Nayak, N. C.; Dash, S. Chaperone-Mediated Autophagy Compensates for Impaired Macroautophagy in the Cirrhotic Liver to Promote Hepatocellular Carcinoma. *Oncotarget* **2017**, *8* (25).

48 Koga, H.; Martinez-Vicente, M.; Arias, E.; Kaushik, S.; Sulzer, D.; Cuervo, A. M. Constitutive Upregulation of Chaperone-Mediated Autophagy in Huntington's Disease. *Journal of Neuroscience* **2011**, *31* (50), 18492–18505.

49 Tekirdag, K.; Cuervo, A. M. Chaperone-Mediated Autophagy and Endosomal Microautophagy: Jointed by a Chaperone. *Journal of Biological Chemistry* **2018**, *293* (15), 5414–5424.

50 Zhang, L.; Hatzakis, E.; Nichols, R. G.; Hao, R.; Correll, J.; Smith, P. B.; Chiaro, C. R.; Perdew, G. H.; Patterson, A. D. Metabolomics reveals that aryl hydrocarbon receptor activation by environmental chemicals induces systemic metabolic dysfunction in mice. *Environ. Sci. Technol.* **2015**, 49, 8067-77.

51 Goya-Jorge, E.; Jorge Rodriguez, M. E.; Veitia, M. S.; Giner, R. M. Plant occurring flavonoids as modulators of the aryl hydrocarbon receptor. *Molecules* **2021**, 26, 2315.

52 Hubbard, T. D.; Murray, I. A.; Perdew, G. H. Indole and tryptophan metabolism: endogenous and dietary routes to Ah receptor activation. *Drug Metab. Dispos.* **2015**, 43, 1522-35.

53 Quintana, F. J.; Basso, A. S.; Iglesias, A. H.; Korn, T.; Farez, M. F.; Bettelli, E.; Caccamo, M.; Oukka, M.; Weiner, H. L. Control of T_{reg} and Th17 cell differentiation by the aryl hydrocarbon receptor. *Nature* **2008**, 453, 65-71.

54 Perdew, G. H.; Esser, C.; Snyder, M.; Sherr, D. H.; van den Bogaard, E. H.; McGovern, K.; Fernandez-Salguero, P. M.; Coumoul, X.; Patterson, A. D. The Ah receptor from toxicity to therapeutics: report from the 5th AHR Meeting at Penn State University, USA, June 2022. *Int. J. Mol. Sci.* **2023**, 24, 5550.

55 Haque, N.; Ojo, E. S.; Krager, S. L.; Tischkau, S. A. Deficiency of adipose aryl hydrocarbon receptor protects against diet-induced metabolic dysfunction through sexually dimorphic mechanisms. *Cells* **2023**, 12, 1748.

56 Smith, S. H.; Jayawickreme, C.; Rickard, D. J.; Nicodeme, E.; Bui, T.; Simmons, C.; Coquery, C. M.; Neil, J.; Pryor, W. M.; Mayhew, D. et al. Tapinarof is a natural AhR agonist that resolves skin inflammation in mice and humans. *J. Invest. Dermatol.* **2017**, 137, 2110-2119.

57 Giovannoni, F.; Li, Z.; Remes-Lenicov, F.; Davola, M. E.; Elizalde, M.; Paletta, A.; Ashkar, A. A.; Mossman, K. L.; Dugour, A. V.; Figueroa, J. M.; Barquero, A. A.;

Ceballos, A.; Garcia, C. C.; Quintana, F. J. AHR signaling is induced by infection with coronaviruses. *Nature Comm.* **2021**, 12, 5148.

58 Shi, J.; Du, T.; Wang, J.; Tang, C.; Lei, M.; Yu, W.; Yang, Y.; Ma, Y.; Huang, P.; Chen, H.; Wang, X.; Sun, J.; Wang, H.; Zhang, Y.; Luo, F.; Huang, Q.; Li, B.; Lu, S.; Hu, Y.; Peng, X. Aryl hydrocarbon receptor is a proviral host factor and a candidate pan-SARS-CoV-2 therapeutic target. *Sci. Adv.* **2023**, 9, eadf0211.

59 Duan, Z.; Li, Y.; Li, L. Promoting epithelial-to-mesenchymal transition by D-kynurenine via activating aryl hydrocarbon receptor. *Mol. Cell. Biochem.* **2018**, 448, 165-173.

60 Moretti, S.; Nucci, N.; Menicali, E.; Morelli, S.; Bini, V.; Colella, R.; Mandarano, M.; Sidoni, A.; Puxeddu, E., The aryl hydrocarbon receptor is expressed in thyroid carcinoma and appears to mediate epithelial-mesenchymal transition. *Cancers (Basel)* **2020**, 12, 145.

61 Gao, H.; Ye, G.; Lin, Y.; Chi, Y.; Dong, S. Benzo[a]pyrene at human blood equivalent level induces human lung epithelial cell invasion and migration via aryl hydrocarbon receptor signaling. *J. Appl. Toxicol.* **2020**, 40, 1087-1098.

62 Selvam, P.; Cheng, C. M.; Dahms, H. U.; Ponnusamy, V. K.; Sun, Y. Y. AhR mediated activation of pro-inflammatory response of RAW 264.7 cells modulate the epithelial-mesenchymal transition. *Toxics* **2022**, 10, 642.

63 Tsai, C. H.; Li, C. H.; Cheng, Y. W.; Lee, C. C.; Liao, P. L.; Lin, C. H.; Huang, S. H.; Kang, J. J. The inhibition of lung cancer cell migration by AhR-regulated autophagy. *Sci. Rep.* **2017**, 7, 41927.

64 Nothdurft, S.; Thumser-Henner, C.; Breitenbucher, F.; Okimoto, R. A.; Dorsch, M.; Opitz, C. A.; Sadik, A.; Esser, C.; Holzel, M.; Asthana, S.; Forster, J.; Beisser, D.; Kalmbach, S.; Gruner, B. M.; Bivona, T. G.; Schramm, A.; Schuler, M., Functional screening identifies aryl hydrocarbon receptor as suppressor of lung cancer metastasis. *Oncogenesis* **2020**, 9, 102.

65 Enan, E.; Matsumura, F. Identification of c-Src as the integral component of the cytosolic Ah receptor complex, transducing the signal of 2,3,7,8-tetrachlorodibenzo-*p*-dioxin (TCDD) through the protein phosphorylation pathway. *Biochem. Pharmacol.* **1996**, 52, 1599-612.

66 Meyer, B. K.; Perdew, G. H. Characterization of the AhR-hsp90-XAP2 core complex and the role of the immunophilin-related protein XAP2 in AhR stabilization. *Biochemistry* **1999**, 38, 8907-17.

67 Kazlauskas, A.; Poellinger, L.; Pongratz, I. Evidence that the co-chaperone p23 regulates ligand responsiveness of the dioxin receptor. *J. Biol. Chem.* **1999**, 274, 13519-24.

68 Ohtake, F.; Baba, A.; Takada, I.; Okada, M.; Iwasaki, K.; Miki, H.; Takahashi, S.; Kouzmenko, A.; Nohara, K.; Chiba, T.; Fujii-Kuriyama, Y.; Kato, S. Dioxin receptor is a ligand-dependent E3 ubiquitin ligase. *Nature* **2007**, 446, 562-6.

69 Yang, Y.; Chan, W. K. Selective autophagy maintains the aryl hydrocarbon receptor levels in HeLa cells: a mechanism that is dependent on the p23 co-chaperone. *Int. J. Mol. Sci.* **2020**, 21, 3449.

70 Cuervo, A. M.; Knecht, E.; Terlecky, S. R.; Dice, J. F. Activation of a selective pathway of lysosomal proteolysis in rat liver by prolonged starvation. *Am. J. Physiol.* **1995**, 269, C1200-8.

71 Rogov, V.; Dotsch, V.; Johansen, T.; Kirkin, V. Interactions between autophagy receptors and ubiquitin-like proteins form the molecular basis for selective autophagy. *Mol. Cell* **2014**, 53, 167-78.

72 Suzuki, K.; Kirisako, T.; Kamada, Y.; Mizushima, N.; Noda, T.; Ohsumi, Y. The pre-autophagosomal structure organized by concerted functions of APG genes is essential for autophagosome formation. *EMBO J.* **2001**, 20, 5971-81.

73 Mizushima, N., The ATG conjugation systems in autophagy. *Curr. Opin. Cell Biol.* **2020**, 63, 1-10.

74 Li, P.; Ji, M.; Lu, F.; Zhang, J.; Li, H.; Cui, T.; Li Wang, X.; Tang, D.; Ji, C. Degradation of AF1Q by chaperone-mediated autophagy. *Exp. Cell. Res.* **2014**, 327, 48-56.

75 Chen, J.; Yang, Y.; Russu, W. A.; Chan, W. K. The aryl hydrocarbon receptor undergoes chaperone-mediated autophagy in triple-negative breast cancer cells. *Int. J. Mol. Sci.* **2021**, 22, 1654.

76 Davarinos, N. A.; Pollenz, R. S. Aryl hydrocarbon receptor imported into the nucleus following ligand binding is rapidly degraded via the cytosplasmic proteasome following nuclear export. *J. Biol. Chem.* **1999**, 274, 28708-15.

77 Roberts, B. J.; Whitelaw, M. L. Degradation of the basic helix-loop-helix/Per-ARNT-Sim homology domain dioxin receptor via the ubiquitin/proteasome pathway. *J. Biol. Chem.* **1999**, 274, 36351-6.

78 Giannone, J. V.; Li, W.; Probst, M.; Okey, A. B. Prolonged depletion of AH receptor without alteration of receptor mRNA levels after treatment of cells in culture with 2,3,7,8-tetrachlorodibenzo-*p*-dioxin. *Biochem. Pharmacol.* **1998**, 55, 489-97.

79 Bao, W.; Gu, Y.; Ta, L.; Wang, K.; Xu, Z. Induction of autophagy by the MG132 proteasome inhibitor is associated with endoplasmic reticulum stress in MCF7 cells. *Mol. Med. Rep.* **2016**, 13, 796-804.

80 Harhouri, K.; Navarro, C.; Depetris, D.; Mattei, M. G.; Nissan, X.; Cau, P.; De Sandre-Giovannoli, A.; Levy, N. MG132-induced progerin clearance is mediated by autophagy activation and splicing regulation. *EMBO Mol. Med.* **2017**, 9, 1294-1313.

81 Shen, Y. F.; Tang, Y.; Zhang, X. J.; Huang, K. X.; Le, W. D. Adaptive changes in autophagy after UPS impairment in Parkinson's disease. *Acta Pharmacol. Sin.* **2013**, 34, 667-73.

82 Massey, A. C.; Kaushik, S.; Sovak, G.; Kiffin, R.; Cuervo, A. M. Consequences of the selective blockage of chaperone-mediated autophagy. *Proc. Natl. Acad. Sci. USA* **2006**, 103, 5805-10.

83 Song, Z.; Pollenz, R. S. Ligand-dependent and independent modulation of aryl hydrocarbon receptor localization, degradation, and gene regulation. *Mol. Pharmacol.* **2002**, 62, 806-16.

84 Kimura, T.; Uesugi, M.; Takase, K.; Miyamoto, N.; Sawada, K. Hsp90 inhibitor geldanamycin attenuates the cytotoxicity of sunitinib in cardiomyocytes via

inhibition of the autophagy pathway. *Toxicol. Appl. Pharmacol.* **2017**, 329, 282-292.

85 Qing, G.; Yan, P.; Xiao, G. Hsp90 inhibition results in autophagy-mediated proteasome-independent degradation of IkappaB kinase (IKK). *Cell. Res.* **2006**, 16, 895-901.

86 Finn, P. F.; Mesires, N. T.; Vine, M.; Dice, J. F. Effects of small molecules on chaperone-mediated autophagy. *Autophagy* **2005**, 1, 141-5.

87 Chen, Y.; Xu, Q.; Ji, D.; Wei, Y.; Chen, H.; Li, T.; Wan, B.; Yuan, L.; Huang, R.; Chen, G. Inhibition of pentose phosphate pathway suppresses acute myelogenous leukemia. *Tumour Biol.* **2016**, 37, 6027-34.

88 Aiello, N. M.; Maddipati, R.; Norgard, R. J.; Balli, D.; Li, J.; Yuan, S.; Yamazoe, T.; Black, T.; Sahmoud, A.; Furth, E. E.; Bar-Sagi, D.; Stanger, B. Z. EMT subtype influences epithelial plasticity and mode of cell migration. *Dev. Cell* **2018**, 45, 681-695.

89 Liu, X.; Huang, H.; Remmers, N.; Hollingsworth, M. A. Loss of E-cadherin and epithelial to mesenchymal transition is not required for cell motility in tissues or for metastasis. *Tissue Barriers* **2014**, 2, e969112.

90 Liu, H.; Yong, Y.; Li, X.; Ye, P.; Tao, K.; Peng, G.; Mo, M.; Guo, W.; Chen, X.; Luo, Y.; Lin, Y.; Qiu, J.; Zhang, Z.; Ding, L.; Zhou, M.; Yang, X.; Lu, L.; Yang, Q.; Xu, P. Chaperone-mediated autophagy regulates cell growth by targeting SMAD3 in glioma. *Neurosci. Bull.* **2022**, 38, 637-651.

91 Jin, Y.; Pan, Y.; Zheng, S.; Liu, Y.; Xu, J.; Peng, Y.; Zhang, Z.; Wang, Y.; Xiong, Y.; Xu, L.; Mu, K.; Chen, S.; Zheng, F.; Yuan, Y.; Fu, J. Inactivation of EGLN3

hydroxylase facilitates Erk3 degradation via autophagy and impedes lung cancer growth. *Oncogene* **2022**, 41, 1752-1766.

92 Su, C. M.; Hsu, T. W.; Chen, H. A.; Wang, W. Y.; Huang, C. Y.; Hung, C. C.; Yeh, M. H.; Su, Y. H.; Huang, M. T.; Liao, P. H. Chaperone-mediated autophagy degrade Dicer to promote breast cancer metastasis. *J. Cell. Physiol.* **2023**, 238, 829-841.

93 Li, Q.; Yue, T.; Du, X.; Tang, Z.; Cui, J.; Wang, W.; Xia, W.; Ren, B.; Kan, S.; Li, C.; Wu, C.; Niu, X.; Li, B.; Lin, K.; Luo, J.; Chen, G.; Wang, Z. HSC70 mediated autophagic degradation of oxidized PRL2 is responsible for osteoclastogenesis and inflammatory bone destruction. *Cell Death Differ.* **2023**, 30, 647-659.

94 Caballero, B.; Wang, Y.; Diaz, A.; Tasset, I.; Juste, Y. R.; Stiller, B.; Mandelkow, E. M.; Mandelkow, E.; Cuervo, A. M. Interplay of pathogenic forms of human tau with different autophagic pathways. *Aging Cell* **2018**, 17, e12692.

95 Caballero, B.; Bourdenx, M.; Luengo, E.; Diaz, A.; Sohn, P. D.; Chen, X.; Wang, C.; Juste, Y. R.; Wegmann, S.; Patel, B.; Young, Z. T.; Kuo, S. Y.; Rodriguez-Navarro, J. A.; Shao, H.; Lopez, M. G.; Karch, C. M.; Goate, A. M.; Gestwicki, J. E.; Hyman, B. T.; Gan, L.; Cuervo, A. M. Acetylated tau inhibits chaperone-mediated autophagy and promotes tau pathology propagation in mice. *Nature Comm.* **2021**, 12, 2238.

96 Sahoo, S.; Padhy, A. A.; Kumari, V.; Mishra, P., Role of ubiquitin-proteasome and autophagy-lysosome pathways in alpha-synuclein aggregate clearance. *Mol. Neurobiol.* **2022**, 59, 5379-5407.

97 Dvorak, Z., Pelargonidin and its glycosides as dietary chemopreventives attenuating inflammatory bowel disease symptoms through the aryl hydrocarbon receptor. *Eur. J. Nutr.* **2020**, 59, 3863-3864.

98 Retnakumar, S. V.; Geesala, R.; Bretin, A.; Tourneur-Marsille, J.; Ogier-Denis, E.; Maretzky, T.; Nguyen, H. T. T.; Muller, S. Targeting the endo-lysosomal autophagy pathway to treat inflammatory bowel diseases. *J. Autoimmun.* **2022**, 128, 102814.

99 Meacham, G. C.; Patterson, C.; Zhang, W.; Younger, J. M.; Cyr, D. M. The Hsc70 co-chaperone CHIP targets immature CFTR for proteasomal degradation. *Nature Cell Biol.* **2001**, 3, 100-5.

100 Kim, J.; de Haro, M.; Al-Ramahi, I.; Garaicoechea, L. L.; Jeong, H. H.; Sonn, J. Y.; Tadros, B.; Liu, Z.; Botas, J.; Zoghbi, H. Y. Evolutionarily conserved regulators of tau identify targets for new therapies. *Neuron* **2023**, 111, 824-838.

101 Bento, C. F.; Fernandes, R.; Ramalho, J.; Marques, C.; Shang, F.; Taylor, A.; Pereira, P. The chaperone-dependent ubiquitin ligase CHIP targets HIF-1alpha for degradation in the presence of methylglyoxal. *PLoS One* **2010**, 5, e15062.

102 Ferreira, J. V.; Fofo, H.; Bejarano, E.; Bento, C. F.; Ramalho, J. S.; Girao, H.; Pereira, P. STUB1/CHIP is required for HIF1α degradation by chaperone-mediated autophagy. *Autophagy* **2013**, 9, 1349-66.

103 Morales, J. L.; Perdew, G. H. Carboxyl terminus of hsc70-interacting protein (CHIP) can remodel mature aryl hydrocarbon receptor complexes and mediate ubiquitination of both the AhR and the 90 kDa heat-shock protein (hsp90) in vitro. *Biochemistry* **2007**, 46, 610-21.

104 Wu, Z.; Geng, Y.; Lu, X.; Shi, Y.; Wu, G.; Zhang, M.; Shan, B.; Pan, H.; Yuan, J. Chaperone-mediated autophagy is involved in the execution of ferroptosis. *Proc. Natl. Acad. Sci. USA* **2019**, 116, 2996-3005.

105 Peng, Y.; Ouyang, L.; Zhou, Y.; Lai, W.; Chen, Y.; Wang, Z.; Yan, B.; Zhang, Z.; Zhou, Y.; Peng, X.; Chen, J.; Peng, X.; Xiao, D.; Liu, S.; Tao, Y.; Liu, W. AhR promotes the development of non-small cell lung cancer by inducing SLC7A11-dependent antioxidant function. *J. Cancer* **2023**, 14, 821-834.

106 Ciolino, H. P.; Yeh, G. C., Inhibition of aryl hydrocarbon-induced cytochrome P-450 1A1 enzyme activity and CYP1A1 expression by resveratrol. *Mol. Pharmacol.* **1999**, 56, 760-7.

107 Wang, H.; Zhang, H.; Tang, L.; Chen, H.; Wu, C.; Zhao, M.; Yang, Y.; Chen, X.; Liu, G. Resveratrol inhibits TGF-beta1-induced epithelial-to-mesenchymal transition and suppresses lung cancer invasion and metastasis. *Toxicol.* **2013**, 303, 139-46.

108 Ouyang, L.; Yan, B.; Liu, Y.; Mao, C.; Wang, M.; Liu, N.; Wang, Z.; Liu, S.; Shi, Y.; Chen, L.; Wang, X.; Cheng, Y.; Cao, Y.; Xiao, D.; Zhang, L.; Liu, S.; Tao, Y. The deubiquitylase UCHL3 maintains cancer stem-like properties by stabilizing the aryl hydrocarbon receptor. *Signal Transduct. Target Ther.* **2020**, 5, 78.

109 Xiong, J.; Zhang, X.; Zhang, Y.; Wu, B.; Fang, L.; Wang, N.; Yi, H.; Chang, N.; Chen, L.; Zhang, J. Aryl hydrocarbon receptor mediates Jak2/STAT3 signaling for non-small cell lung cancer stem cell maintenance. *Exp. Cell Res.* **2020**, 396, 112288.

110 Gerashchenko, T. S.; Novikov, N. M.; Krakhmal, N. V.; Zolotaryova, S. Y.; Zavyalova, M. V.; Cherdyntseva, N. V.; Denisov, E. V.; Perelmuter, V. M. Markers of Cancer Cell Invasion: Are They Good Enough? *J. Clin. Med.* **2019**, 8, 1092.

111 Jin, U. H.; Karki, K.; Cheng, Y.; Michelhaugh, S. K.; Mittal, S.; Safe, S. The aryl hydrocarbon receptor is a tumor suppressor-like gene in glioblastoma. *J. Biol. Chem.* **2019**, 294, 11342-11353.

112 Livak, K. J.; Schmittgen, T. D. Analysis of relative gene expression data using real-time quantitative PCR and the $2^{-\Delta\Delta C_T}$ Method. *Methods* **2001**, 25, 402-8.

113 Han, W.; Sun, P.; Yao, R.; Zhang, W.; Zhou, X.; Jia, Y.; He, K. Comprehensive Pan-Cancer Analysis of PTGES3 and Its Prognostic Role in Hepatocellular Carcinoma. *Frontiers in Oncology* **2023**, *13*.

114 Ali, M. M. U.; Roe, S. M.; Vaughan, C. K.; Meyer, P.; Panaretou, B.; Piper, P. W.; Prodromou, C.; Pearl, L. H. Crystal Structure of an Hsp90–Nucleotide–P23/Sba1 Closed Chaperone Complex. *Nature* **2006**, *440* (7087), 1013–1017.

115 Felts, S. J.; Toft, D. O. P23, a Simple Protein with Complex Activities. *Cell Stress & Chaperones* **2003**, *8* (2), 108.

116 Vikash Reebye; Laia Querol Cano; Lavery, D. N.; Brooke, G. N.; Powell, S.; D. Chotai; Walker, M. M.; Whitaker, H. C.; Wait, R.; Hurst, H. C.; Bevan, C. L. Role of the HSP90-Associated Cochaperone P23 in Enhancing Activity of the Androgen Receptor and Significance for Prostate Cancer. *Molecular Endocrinology* **2012**, *26* (10), 1694–1706.

117 Pappas, B.; Yang, Y.; Wang, Y.; Kim, K.; Chung, H. J.; Cheung, M.; Ngo, K.; Shinn, A.; Chan, W. K. P23 Protects the Human Aryl Hydrocarbon Receptor from Degradation via a Heat Shock Protein 90-Independent Mechanism. *Biochemical Pharmacology* **2018**, *152* (2018), 34–44.

118 Jiang, W.; Wei, Q.; Xie, H.; Wu, D.; He, H.; Xuedong Lv. Effect of PTGES3 on the Prognosis and Immune Regulation in Lung Adenocarcinoma. *Analytical Cellular Pathology* **2023**, *2023* (4522045), 1–23.

119 Cebola, I.; Custodio, J.; Muñoz, M.; Díez-Villanueva, A.; Paré, L.; Prieto, P.; Aussó, S.; Coll-Mulet, L.; Boscá, L.; Moreno, V.; Peinado, M. A. Epigenetics Override Pro-Inflammatory PTGS Transcriptomic Signature towards Selective Hyperactivation of PGE2 in Colorectal Cancer. *Clinical Epigenetics* **2015**, *7* (1).

120 Liang, Y.; Liu, M.; Wang, P.; Ding, X.; Cao, Y. Analysis of 20 Genes at Chromosome Band 12q13: *RACGAP1*and*MCRS1*Overexpression in Nonsmall-Cell Lung Cancer. *Genes, Chromosomes and Cancer* **2012**, *52* (3), 305–315.

121 Nguyen, P. M.; Wang, D.; Wang, Y.; Li, Y.; Uchizono, J. A.; Chan, W. K. P23 Co-Chaperone Protects the Aryl Hydrocarbon Receptor from Degradation in Mouse and Human Cell Lines. *Biochemical Pharmacology* **2012**, *84* (6), 838–850.

122 Wang, D.; Xu, Q.; Yuan, Q.; Jia, M.; Niu, H.; Liu, X.; Zhang, J.; Young, C. Y.; Yuan, H. Proteasome Inhibition Boosts Autophagic Degradation of Ubiquitinated-AGR2 and Enhances the Antitumor Efficiency of Bevacizumab. *Oncogene* **2019**, *38* (18), 3458–3474.

123 Jiang, P.; Mizushima, N. LC3- and P62-Based Biochemical Methods for the Analysis of Autophagy Progression in Mammalian Cells. *Methods* **2015**, *75* (2015), 13–18.

124 Yoshii, S. R.; Mizushima, N. Monitoring and Measuring Autophagy. *International Journal of Molecular Sciences* **2017**, *18* (9).

125 Wu, Y.-T.; Tan, H.-L.; Shui, G.; Bauvy, C.; Huang, Q.; Wenk, M. R.; Ong, C.-N.; Codogno, P.; Shen, H.-M. Dual Role of 3-Methyladenine in Modulation of Autophagy via Different Temporal Patterns of Inhibition on Class I and III Phosphoinositide 3-Kinase. *Journal of Biological Chemistry* **2010**, *285* (14), 10850–10861.

126 Los, G. V.; Encell, L. P.; McDougall, M. G.; Hartzell, D. D.; Karassina, N.; Zimprich, C.; Wood, M. G.; Learish, R.; Ohana, R. F.; Urh, M.; Simpson, D.; Mendez, J.; Zimmerman, K.; Otto, P.; Vidugiris, G.; Zhu, J.; Darzins, A.; Klaubert, D. H.; Bulleit, R. F.; Wood, K. V. HaloTag: A Novel Protein Labeling Technology for Cell Imaging and Protein Analysis. *ACS Chemical Biology* **2008**, *3* (6), 373–382.

127 Quintavalle, C.; Stefania Di Costanzo; Zanca, C.; Tasset, I.; Alessandro Fraldi; Mariarosaria Incoronato; Mirabelli, P.; Monti, M.; Ballabio, A.; Pucci, P.; Ana María Cuervo; Gerolama Condorelli. Phosphorylation-Regulated Degradation of the Tumor-Suppressor Form of PED by Chaperone-Mediated Autophagy in Lung Cancer Cells. *Journal of Cellular Physiology* **2014**, *229* (10), 1359–1368.

128 Zhou, J.; Yang, J.; Fan, X.; Hu, S.; Zhou, F.; Dong, J.; Zhang, S.; Shang, Y.; Jiang, X.; Guo, H.; Chen, N.; Xiao, X.; Sheng, J.; Wu, K.; Nie, Y.; Fan, D.

Chaperone-Mediated Autophagy Regulates Proliferation by Targeting RND3 in Gastric Cancer. *Autophagy* **2016**, *12* (3), 515–528.

129 Hubbi, M. E.; Hu, H.; Kshitiz; Ahmed, I.; Levchenko, A.; Semenza, G. L. Chaperone-Mediated Autophagy Targets Hypoxia-Inducible Factor-1α (HIF-1α) for Lysosomal Degradation. *Journal of Biological Chemistry* **2013**, *288* (15), 10703–10714.

130 Lv, L.; Li, D.; Zhao, D.; Lin, R.; Chu, Y.; Zhang, H.; Zha, Z.; Liu, Y.; Li, Z.; Xu, Y.; Wang, G.; Huang, Y.; Xiong, Y.; Guan, K.-L.; Lei, Q.-Y. Acetylation Targets the M2 Isoform of Pyruvate Kinase for Degradation through Chaperone-Mediated Autophagy and Promotes Tumor Growth. *Molecular Cell* **2011**, *42* (6), 719–730.

131 Tsai, C.-H.; Li, C.-H.; Cheng, Y.-W.; Lee, C.-C.; Liao, P.-L.; Lin, C.-H.; Huang, S.-H.; Kang, J.-J. The Inhibition of Lung Cancer Cell Migration by AhR-Regulated Autophagy. *Scientific Reports* **2017**, *7* (1).

132 Ching Hao Li; Chen Wei Liu; Chi Hao Tsai; Peng, Y.; Hsuan, Y.; Po Lin Liao; Chen Chen Lee; Yu Wen Cheng; Jaw Jou Kang. Cytoplasmic Aryl Hydrocarbon Receptor Regulates Glycogen Synthase Kinase 3 Beta, Accelerates Vimentin Degradation, and Suppresses Epithelial–Mesenchymal Transition in Non-Small Cell Lung Cancer Cells. *Archives of Toxicology* **2016**, *91* (5), 2165–2178.

133 Kiffin, R.; Christian, C.; Knecht, E.; Cuervo, A. M. Activation of Chaperone-Mediated Autophagy during Oxidative Stress. *Molecular Biology of the Cell* **2004**, *15* (11), 4829–4840.

134 Tsuji, G.; Takahara, M.; Hiroshi Uchi; Takeuchi, S.; Chikage Mitoma; Yoichi Moroi; Masutaka Furue. An Environmental Contaminant, Benzo(A)Pyrene,

Induces Oxidative Stress-Mediated Interleukin-8 Production in Human Keratinocytes via the Aryl Hydrocarbon Receptor Signaling Pathway. *Journal of Dermatological Science* **2011**, *62* (1).

135 Christina Blume Clark; Rane, M. J.; Delphine El Mehdi; Miller, C. J.; Sachleben, L. R.; Gozal, E. Role of Oxidative Stress in Geldanamycin-Induced Cytotoxicity and Disruption of Hsp90 Signaling Complex. *Free Radical Biology and Medicine* **2009**, *47* (10), 1440–1449.

Appendix A: Methodology

RT-qPCR

RNA isolation: DNase/RNase-free filter tips and tubes were used in all steps. Total RNA was extracted from A549 cells using TRI Reagent (Zymo Research) and RNA miniprep kit (Direct-zol) according to the manufacturer's recommendations. In brief, 400 μl of TRI Reagent was added into each well of 12-well plate and mixed well by pipetting, followed by being collected in 1.5 ml tubes. 400 μl of ethanol was added into each tube and mixed well. For RNA purification, the mixture was transferred into a Zymo-Spin Column in a Collection Tube followed by centrifuging at 16,000g for 30s. The flow-through was discarded. 400 μl of RNA Wash Buffer was added into the Column and centrifuged to remove the flow-through. A mixture of 5 μl DNase I and 75 μl DNA Digestion Buffer was added into each column. It was kept at room temperature for 15 min. The column was washed twice with 400 μl of Direct-zol RNA PreWash Buffer, and once with 700 μl of RNA Wash Buffer. The column was transferred into a new RNase-free tube. 100 μl of DNase/RNase-Free Water was added into the column and centrifuged at 16,000g to elute the total RNA. The eluted RNA is recommended to be used immediately for cDNA synthesis.

cDNA synthesis: For each reaction, to denature the RNA sample and anneal the primers, 1μg of RNA and 2μl of random primer (1:5 diluted in DNase/RNase free Water) were mixed with DNase/RNase free Water to make a total volume of 10 μl in a 0.2 ml tube. The samples were incubated at 65℃ for 2min in a PCR thermocycler and chilled on ice. A 10 μl mixture of 3μl of RNase-free water, 2μl of 10X MMLV buffer, 2μl of 100mM DTT, 0.5μl of ScriptGuard RNase inhibitor, 2μl of dNTP mix, and 0.5μl of MMLV

high performance reverse transcriptase was added in each tube and mixed well. The PCR thermocycler was used with the following protocol: 25℃ for 10min, 37℃ for 60min, 85℃ for 5min, and 4℃ for 1min. The cDNA was centrifuged briefly and used for real-time PCR.

qPCR analysis: For each reaction, a 20 µl mixture of 10 µl iTaq SYBR green supermix, 2 µl Forward primer (400nM), 2 µl Reverse primer (400nM), 5 µl RNase-free water, and 1 µl cDNA template was prepared in a PCR tube. qPCR was performed on a CFX Connect real-time PCR operating system (Bio-rad, USA) according to the following protocol: 95℃ for 2 min, 40 cycles of 95 ℃ for 15s and 60 ℃ for 1min. Relative gene expression was analyzed by the $2^{-\Delta\Delta Cq}$ method [112] and *18s* rRNA was used as an internal control for normalization.

Western Blot analysis

Preparation of whole cell extract: cells were scraped in cold PBS and centrifuged at 400g for 5 min to collect cell pellets. The collected cells were washed once with cold PBS and then lysed in lysis buffer (25mM HEPES pH7.4, 0.4 M KCl, 1mM EDTA, 1mM DTT, 10% glycerol, 1% NP40, 1mM PMSF, and 2µg/ml leupeptin). After 3 cycles of freeze and thaw, cell lysates were kept on ice for 30 min and then centrifuged at 16,000g for 15 min at 4 ℃. The supernatants were used as whole cell extracts. Bicinchoninic acid (BCA) assay: A 96-well plate was used for the BCA assay. The BSA standard was prepared according to Table 1. The sample was 1:10 diluted in HEDG buffer. The volume for each well was 10 µl and duplication for each well. 190 µl BCA reagent mixture of 98% reagent A and 2% reagent B was added into each well with a multichannel pipette, followed by mix well. The Plate was incubated at 37℃ for 30min.

The Epoch plate reader was used to measure the absorbance at 562 nm. The protein concentration was calculated based on the standard curve and absorbance.

SDS-PAGE: The gel was prepared according to Table 2. In brief, 14 mg agarose was dissolved in 1.5 ml di H_2O and 0.5 ml lower tris buffer, followed by microwave twice briefly. It was dripped into the glass plates set to seal the bottom. Waiting 10 min for solidify. The running gel was poured into the glass set until the level was about 1cm below the top edge. Di H_2O was gently added on top of the running gel for acrylamide polymerization. The gel was kept at room temperature for more than 30 min to form a flat and clear interface between the water and gel. The water layer was poured off and cleaned with filter paper. The stacking gel was poured, and a 15-well comb was inserted into it. The gel was kept at room temperature for another 4 hours for complete polymerization. Based on the protein concentration, 20 µg of the whole cell extract was prepared and adjusted to the same volume with HEDG buffer. The lysate was mixed with 1× treatment buffer (with βME), followed by vortex and heat at 95 ℃ for 3 min. 350 ml of 1×TGS running buffer was used for electrophoresis, 110 V for the stacking gel, and 160 V for the running gel.

Li-COR Western analysis: To set up the transfer sandwich, 4 pieces of filter paper and nitrocellulose membrane were wet before transfer. The order from negative electrode to positive electrode was black frame, foam, 2 pieces of filter paper, SDS-PAGE gel, nitrocellulose membrane, 2 pieces of filter paper, foam, and clear frame. It was transferred for 120 min using 300mA in a cold room. After transfer, the membrane was rinsed in diH_2O, followed by being incubated in 5ml total protein stain solution for 5 min. It was rinsed with wash solution twice and diH_2O once. LI-COR Odyssey CLx

imaging system with 700nm channel was used to image the total protein stain. After the image, the membrane was incubated in revert solution for 5 min to destain and then washed with diH2O. The membrane was blocked in blocking buffer (PBS, 0.1% Tween-20, 5% BSA) for 1h and incubated with primary antibody overnight in a cold room. Then it was washed with 1×PBST (PBS and 0.1% Tween-20) for 5 min × 5. The membrane was incubated with a secondary antibody for 2h at room temperature, followed by washing with 1×PBST (PBS and 0.1% Tween-20) for 5 min × 5 and 1×PBS for 5 min. The membrane was dried before proceeding to imaging. Results were obtained and quantified by using LI-COR Odyssey CLx imaging system.

Co-immunoprecipitation

Cells from T75 flask were harvested to be lysed in lysis buffer (25mM HEPES pH7.4, 0.15 M KCl, 1mM EDTA, 1mM DTT, 10% glycerol, 10mM N-Ethylmaleimide, 1mM PMSF, and 2μg/ml leupeptin). About 2mg of the whole cell extract was incubated with 2 μl of rabbit anti-AHR antibody (SA210) for 30min at room temperature. To pre-equilibrate the Dynabeads™ Protein G (Invitrogen) magnetic beads, 3-5 μl of magnetic beads slurry was aliquoted into each GeneMate microfuge tube. Then it was set on Magnet for 1 min and the supernatant ethanol was discarded carefully. 0.5ml of diH2O was added and mixed gently. Magnet for 1 min and discard the supernatant. This step was repeated twice. Then the beads were washed with IP buffer (25mM HEPES pH7.4, 1mM EDTA, 1mM DTT, 10% glycerol, and 150mM NaCl). Magnet for 1 min and discard the supernatant. The sample was added to the pre-equilibrated magnetic beads and q.s. to 1ml with IP buffer (with 1mg/mL BSA). It was rotated at 60rpm in the cold room for 16-18h. The magnetic beads-Ab-Ag complex were washed twice with cold IP buffer

(with 0.05% Tween-20) on the magnet for 5min. Resuspend the magnetic beads-Ab-Ag complex in 30μl of 1× treatment buffer (with βME) and boil at 95 ℃ for 3min to free the bound protein. 1% of the whole cell extract was used as an input control. All the samples were analyzed by western blot with antibodies against AHR, LAMP2, and Hsc70.

Proximity ligation assay

The microscope glass coverslips (~1 cm^2) were placed in the wells of a 12-well plate, and cells were seeded onto them and grown to approximately 70-80% of confluence. Cells were treated with or without CQ for 6h and then were rinsed with ice-cold PBS twice. Cells were fixed and permeabilized with 100% methanol (chilled at -20℃ before) for 5min. After 3 times washing with ice-cold PBS, cells were ready for proximity ligation assay according to the Duolink® PLA Fluorescence Protocol. Briefly, one drop of Duolink Blocking Solution was added to each microscope glass coverslip to completely cover the samples. Then the samples were incubated at 37℃ for 1h, followed by incubation with mouse anti-AHR monoclonal antibody (A-3x) and rabbit anti-LC3B monoclonal antibody (1:100 diluted in the Duolink antibody diluent) for 1h at 37℃. Samples were washed 2×5min with 1×wash buffer A, followed by incubation with PLUS and MINUS PLA probes (1:5 diluted in the Duolink antibody diluent) for 1h at 37℃. Samples were washed 2×5min with 1×wash buffer A, followed by incubation with ligase (1:40 diluted in 1×ligation buffer) for 30min at 37℃. Samples were washed 2×5min with 1×wash buffer A, followed by incubation with polymerase (1:80 diluted in 1×amplification buffer) for 100 min at 37℃. From this step, the samples were protected from light since the amplification buffer is light-sensitive. Finally, samples were washed with 1×wash

buffer B for 2×10 min and 0.01×wash buffer B for 1 min. The nucleus was stained by 1μg/mL DAPI in water for 1min. Nail polish was used to seal the edges of the coverslip to the microscope slide. Samples were imaged by using an inverted microscope (BZ-X700, KEYENCE, USA) with a camera.

CRISPR/Cas9 mediated *AHR* knockout in A549 cells

Three different single guide RNA (sgRNA) targeting the exon 2 of the human *AHR* gene were used to knock out the *AHR* gene in A549 cells. The sequences were as follows, sgRNA1: 5'- GCTGAAGGAATCAAGTCAAA-3'; sgRNA2: 5'- ACAAGATGTTAT-TAATAAGT-3'; sgRNA3:5'- GAGAGCCAAGAGCTTCTTTG-3'. Cas9 nuclease NLS and sgRNAs were introduced as a ribonucleoprotein (RNP) complex into A549 cells through transfection using the Lipofectamine RNAiMAX according to the manufacturer's recommendations. In brief, 3μM Cas9 nuclease NLS was combined with 3μM sgRNAs (1μM each of 3 sgRNAs) to form RNPs in 12.5μl volume with the Opti-MEM. Gently mixed the reaction and incubated at room temperature for 10 min. 1.2μl of transfection reagent RNAiMAX was diluted in 12.5μl of the Opti-MEM and was added directly into the RNPs tube. The RNPs/liposome complexes were mixed gently and incubated at room temperature for 20 min. Meanwhile, 3.2×10^5 cells/ml A549 cell suspension was prepared and 125μl of them were added into each well of a 96-well plate, followed by mixing with 25μl of RNPs/liposome complexes. The transfected cells were incubated at 37 ℃, 5% CO_2 for 72h. Then the isolation of single cells from the knockout cell pool was accomplished through limiting dilution according to the protocol from Synthego. In brief, calculate the concentration of cells in the cell suspension. Dilute cells to 0.5-1 cell/100 μl of medium or 100 cells/10 ml of medium for each 96-well plate. The diluted cell

suspension was transferred to a sterile reservoir. 100ul/well of the diluted cell suspension was aliquoted into each well of a 96-well plate using a multichannel pipette. The cells were kept at 37℃, 5% CO_2 for expansion. The colonies were transferred to a 24-well plate when it reached 70% confluence. After several weeks of expansion, cells from each well were collected for Western blot and PCR analysis. To genotype clones, genomic DNA was isolated using QuickExtract DNA extraction solution (Lucigen). PCR was performed to amplify the edited region using PCR Master Mix (Promega) with the following primers: OL921 Forward 5'-TCGGAAGAATTTAACC-CATTCCCT-3' and OL922 Reverse 5'-TGCAGCCACTGAAATGATGC-3'. The DNA fragment ~500bp was observed by agarose gel electrophoresis and was purified for Sanger sequencing (Functional Biosciences, WI, USA). The sequencing data was uploaded to the online Inference of CRISPR Edits (ICE) analysis tool (http://ice.synthego.com) for knockout analysis.

Generation of p23, ATG5, LAMP2 stable knockdown A549 cells using lentivirus

Lentivirus containing p23, ATG5, or LAMP2 shRNA was prepared as follows: AD293 cells (7×10^5) in 5ml of growth media (10% fetal bovine serum and 2mM GlutaMAX-I in DMEM) were seeded in a 25 cm^2 flask. Cells were incubated at 37 ℃, 5% CO_2 overnight. Then AD293 cells were transfected using 10μl EndoFectin™ transfection reagent with 5μg plasmids (2.5μg of pLKO.1 specific shRNA plasmid, 1.875μg of the pCMV-dR8.2 dvpr packaging plasmid, and 0.625μg of the pCMV-VSV-G envelope plasmid). Fresh complete medium was replaced 15h after transfection. After 24h, the medium containing lentiviral particles was transferred to a 15ml tube and stored at 4 ℃. Another 5ml of fresh complete medium was added to the cells and the

medium containing lentiviral particles was harvested after 24h of incubation. The combined medium was centrifuged at 400g for 5min to pellet any AD293 cells and the supernatant was used for A549 infection. Stable p23, ATG5, or LAMP2 knockdown cell lines were generated as follows: A549 cells were seeded in a 25 cm^2 flask to achieve 50-70% confluence on the next day. A fresh complete medium containing 8μg/mL polybrene was replaced. 500μl of medium containing lentiviral particles was added into the flask. After 24h, the medium was replaced with fresh complete medium containing 1.5μg/ml of puromycin for stable cell line selection. Change to fresh medium containing puromycin every 2-3 days. p23 knockdown stable A549 cells were generated using pLKO.1 Lentiviral (TRC) p23 siRNA #1475 plasmid, ATG5 knockdown stable A549 cells were generated using pLKO.1 Lentiviral (TRC) ATG5 shRNA #5 (TRCN0000151963) plasmid; LAMP2 knockdown stable A549 cells were generated using pLKO.1 Lentiviral (TRC) LAMP2 shRNA #4 (TRCN0262) plasmid.

Transient Transfection

A549 cells were seeded in a 6-well plate to achieve 90-95% confluence at the time of transfection. Plasmid DNA, EndoFectin™ transfection reagent, and Opti-MEM were equilibrated to room temperature before use. Cells were transfected with 4μg of plasmid and 8μl of transfection reagent. Both plasmids and transfection reagent were diluted in 125μl of the Opti-MEM, respectively. Then the diluted transfection reagent and the diluted DNA were combined and kept at room temperature for 20 min to allow DNA-transfection reagent complexes to form. The combined complexes were added to each well and mixed gently. The cells were treated with drugs after 48h of incubation at 37 ℃, 5% CO2, and harvested for analysis. For the overexpression of HaloTag-AHR stable

cell line selection, the medium was replaced with a fresh complete medium containing 2mg/ml of G418 after 48h of incubation. Cells were passaged in T75 flasks with G418 selection for about one month, followed by Western blot analysis.

Wound healing assay

A549 cells were seeded in 6-well plates and formed monolayers at the time of wounding. A sterile 1ml pipette tip was used to scratch across the monolayers to form a linear wound. Then the disassociated cells and debris were removed by washing with PBS. Fresh medium was added into each well, followed by imaging using an inverted microscope (BZ-X700, KEYENCE, USA) in 4×objective with a camera. Cells were treated with DMSO or 6AN for 48h. Representative images were taken at the same position under the inverted microscope with a camera. The scale bar on the representative images is 500μm.

Transwell migration assay

Falcon® 24-well cell culture inserts with transparent PET membrane (8.0μm pore size) and 24-well plates were used to determine the cell migration capability. For migration assay, 5×10^4 cells suspended in 100μl of DMEM medium containing 1% FBS were added into the upper chamber, and the lower chamber of the transwell plates were filled with 700μl of DMEM medium containing 10% FBS. After 24h incubation, the inserts were washed with PBS twice, followed by being fixed with ice-cold methanol for 10 min. The cells were stained with 0.1% crystal violet for 5min. Then the cells on the upper side of the membrane were removed with cotton swabs carefully. The inserts were dipped into the distilled water as many times as needed to remove the excess crystal violet. Only the cells that migrated through the membrane to the bottom of

inserts were imaged by using an inverted microscope (BZ-X700, KEYENCE, USA) with a camera. Three separate microscopic fields, which covered about 80% of the well, were randomly captured and analyzed by Image-J software.

Transwell Invasion assay

The transwell invasion assay can be easily modified from the cell migration assay. Falcon® 24-well cell culture inserts with transparent PET membrane (8.0μm pore size) and Corning Matrigel matrix were used to determine the cell invasion capability. Before cell seeding, the Matrigel matrix was thawed on ice overnight. It was diluted at the ratio of 1:5 in a DMEM medium that contained 1% FBS. For invasion assay, 1×10^5 cells suspended in 100μl of DMEM medium containing 1%FBS were added into the upper chamber, and the lower chamber of the transwell plates was filled with 700μl of DMEM medium containing 10% FBS. After 24h incubation, the inserts were washed with PBS twice, followed by being fixed with ice-cold methanol for 10 min. The cells were stained with 0.1% crystal violet for 5min. Then the cells on the upper side of the membrane were removed with cotton swabs carefully. The inserts were dipped into the distilled water as many times as needed to remove the excess crystal violet. Only the cells that migrated through the membrane to the bottom of inserts were imaged by using an inverted microscope (BZ-X700, KEYENCE, USA) with a camera. Three separate microscopic fields, which covered about 80% of the well, were randomly captured and analyzed by Image-J software.

Appendix B: Preparation of Solutions and Reagents

Table 1

Preparation of BSA standard curve in BCA assay on 96-well plate

Well	BSA concentration (mg/ml)	HEDG buffer (µl)	BSA dilution (µl)	
A	0	10	0	1:100 of original BSA dilution
B	0.05	5	5	
C	0.1	0	10	
D	0.2	8	2	1:10 of original BSA dilution
E	0.3	7	3	
F	0.5	5	5	
G	0.7	3	7	
H	1	0	10	

Note. The original BSA solution is 10 mg/ml. The sample from the whole cell extract is diluted 1:10 in HEDG buffer for BCA assay.

Table 2

SDS-PAGE gel preparation

Reagents	12% running gel	15% running gel	Stacking gel
DI water (ml)	6.9	4.8	3.4
30% Acrylamide /0.8%Bisacrylamide (ml)	8	10.1	0.575
Upper Tris Buffer (ml)			1.25
Lower Tris Buffer (ml)	5	5	
10% ammonium persulfate (µl)	100	100	50
TEMED (µl)	10	10	5

Note. The volume is for preparing 2 gels of 1.5 mm thickness.

Western transfer buffer

Tris base	3.03 g
Glycine	14.4 g
Methanol	200 ml

Adjust volume to 1 L with di H_2O.

HEDG Buffer

25 mM HEPES	5.96 g
1 mM EDTA	2 ml of 0.5M EDTA
1 mM DTT	154.25 mg
10% glycerol	100 ml

Adjust volume to 1 L with di H_2O, pH to 7.4.

30% Acrylamide/ 0.8% Bisacrylamide

Acrylamide	120 g
Bisacrylamide	3.2 g

Adjust volume to 400 ml with di H_2O.

Lower Tris buffer

1.5M Tris base	181.7 g

Adjust volume to 1 L with di H_2O, pH to 8.8.

Upper Tris buffer

0.5M Tris base	30.3 g

Adjust volume to 500 ml with di H_2O, pH to 6.8.

Treatment Buffer (with no βME)

Glycerol	5 ml
Upper Tris buffer	6.25 ml
10% SDS	20 ml
0.25% Bromophenol Blue	4 ml

Adjust volume to 50 ml. The working buffer is a mixture of 950 µl of Treatment buffer and 50 µl of βME.

0.1% crystal violet

Crystal violet	0.05 g
20% Methanol	50 ml

Appendix C: Liquide Nitrogen Position of Engineered Cell Lines

Table 3

Liquide Nitrogen Position of Engineered Cell Lines

Cell lines	B106A Liquid nitrogen tank
A549-LAMP2 knockdown (KD)	Red-6
A549-ATG5 knockdown (KD)	Red-6
A549-scramble	White-5, Red-6
A549-p23 knockdown (KD)	White-5, Red-6
A549-HaloTag-AHR	Red-6
A549-AHR knockout (KO) cell lines 5G11	Blue-5, Red-6
A549-AHR knockout (KO) cell lines 4H2	Blue-5, Red-6
A549-AHR knockout (KO) cell lines 2F6	Blue-5, Red-6
A549-AHR knockout (KO) cell lines 3C9	Blue-5, Red-6
A549-AHR knockout (KO) cell lines 5F2	Blue-5, Red-6
A549-AHRKO-5G11-HaloTag-AHR	Red-6
A549-AHRKO-5G11-LAMP2KD	Red-6
KLN 205	White-6, Red-6
A549-LC3B knockdown (KD)	White-3, White-5, Red-6